The Magnetism of Free Cobalt Clusters Measured in Molecular Beams

A Thesis
Presented to
The Academic Faculty

by

Xiaoshan Xu

In Partial Fulfillment
of the Requirements for the Degree
Doctor of Philosophy

School of Physics
Georgia Institute of Technology
May 2007

The Magnetism of Free Cobalt Clusters Measured in Molecular Beams

Approved by:

Professor Walt de Heer, School of Physics,
Georgia Institute of Technology, Advisor

Professor Ward Plummer,
University of Tennessee, ORNL

Professor Meiyin Chou, School of Physics,
Georgia Institute of Technology

Professor Robert L. Whetten, School of Chemistry and Biochemistry,
Georgia Institute of Technology

Professor Phillip First, School of Physics,
Georgia Institute of Technology

Date Approved: December 7th, 2006

This work is dedicated to my wife – lovely Yan.

PREFACE

The fascinating world of condensed matter physics has intrigued me since I was an undergraduate student who hah just touched quantum mechanics. It was professor Jin who planted the big question in my mind: is complexity physics? Reductionists believe that everything can be eventually explained using a few unified simple rules. But increasing complexity when the number of objects increases definitely introduces a host of interesting phenomena, which are studied in condensed matter physics. In the past a few decades, cluster physics emerged as physicists attacked the issue of complexity, not only for understanding the fundamental physics but also for the great application potentials of small systems. I was very lucky to join the small system lab in fall 2000 to study metal clusters. When Ramiro Moro showed me the beautiful mass spectrum that can resolve a single proton, I was amazed. As I learned more and more about cluster physics, I discovered that it involves classical and quantum mechanics, thermal and electrodynamics, statistical and nonlinear physics, atomic molecular and condensed matter physics. I got more and more excited by the wonder world I was entering. Starting with data analysis, I learned from my advisor, Walt, the importance of a physicist's ability to extract physical information from raw data and also the importance of designing a convincing experiment. More important is to respect all data. Any unusual experimental result may be a hint to new physics, especially in cluster physics. After an interesting discovery, it takes systematic study to verify it. If a new phenomenon cannot be understood, we should neither ignore it nor rush to publication. As a matter of fact, it took us about 4 years and hundreds of experiments to understand the adiabatic process of clusters' negotiation with an inhomogeneous field. Another example is that we spent a year to understand the thermalization condition of the cluster beam source. Now this hard work is paying off. Looking back to the six years in the Small System Lab of Georgia Tech, I learned fundamental and new physics, but more essentially, how to conduct physics research.

ACKNOWLEDGEMENTS

I am deeply indebted to my advisor Dr. Walt A. de Heer whose help, stimulating suggestions and encouragement helped me in all the time of research.

I would like to express my deep and sincere gratitude to my committee members Dr. Meiyin Chou, Dr. Phillip First, Dr. Ward Plummer and Dr. Robert L. Whetten for the precious time they spent on my thesis and their suggestions.

I am deeply grateful to the members of our research group who participated in this work: Ramiro Moro, Shuangye Yin, Anthony Liang and John Bowlan.

I want to thank former group members who contributed in building the molecular beam machine: Philippe Poncharal, Stefan Frank and Patrice Keghelian. I love the years in the Small System Lab and want to thank all the other members: Claire Berger, Zhimin Song and Xuebin Li.

During the time in Georgia Tech, I have learned a lot of physics from Dr. Fox, Dr. Zangwill, Dr. Kennedy, Dr. Flannery, Dr. Sa De Melo and Dr. Landman.

I received help from Judy Melton, Kathy Hardwick, Lori Sheridan, Velera Pate, Nancy Naggett, Debbie James, Patricia Dixon, Kelvin Carter and Scott Centers. I also want to thank the training from machine shop by Norman Scott, Leon Halverson and Sam Mize.

TABLE OF CONTENTS

LIST OF TABLES

LIST OF FIGURES

LIST OF SYMBOLS

amu	mass unit, 1 amu = 1.66053886 $\times 10^{-27}$ kg
AIP	adiabatic ionization potential
B	magnetic field
$B_{external}$	external magnetic field
Debye	unit of dipole moment, 1 Debye = 3.336 $\times 10^{-30}$ coulomb meter
DLM	disordered local moment theory
DOS	density of states
e	electronic charge 1 e = 1.6 $\times 10^{-19}$ coulomb
eV	electronic volt, unit of energy, 1 eV = 1.60 $\times 10^{-19}$ J
excimer	excited dimer, used in excimer laser
E	electric field
E_{aniso}	magnetic anisotropy of a cluster
E_F	Fermi energy
FLB	fluctuating local band theory
g_L	orbital Lande factor
g_{Lande}	Lande factor
g_S	spin Lande factor
H	Hamiltonian
Hz	unit of frequency, 1 $H_z = 1sec^{-1}$
I^{off}	beam profile with field off
I^{on}	beam profile with field on
IP	ionization potential
J	quantum number of total angular moment of a small particle
J_z	projection of J along certain space direction
K	Kelvin, unit of temperature
K	geometric constant of the appratus in the Stern-Gerlach experiment

k_B	Boltzmann constant, $1k_B = 1.38 \times 10^{-23} J/K$
l_{field}	length of deflection plates
L	orbital quantum number of an electron
m	mass of a cluster
meV	unit of energy, 1 meV = 0.001 eV
M	Magnetization
$M_{saturate}$	saturation magnetization
nm	nanometer, 1 nm = 10^{-9} meter
N	number of atoms
N_e	number of valence electrons
OPO	Optical Parametric Oscillators
R	radius
RPA	random phase approximation
S	electronic spin
SCR	selfconsistent renomalization method
SR	spin relaxation
Torr	unit of pressure, 1 torr = 133 pascal
T	tesla, unit of magnetic field
T	temperature
T_{block}	blocking temperature
T_c	transition temperature of ferromagnetism
T_{Debye}	Debye temperature
TOF	time of flight
v	speed of the cluster
V	volume or voltage
VIP	vertical ionization potential
W^{off}	second moment of beam profile with field off
W^{on}	second moment of beam profile with field on
WF	work function

YAG	yttrium aluminum garnet
α	polarizability
α_{atom}	atomic polarizability
χ	magnetic susceptibility
δ	energy spacing
$\delta_{spilllout}$	electronic spillout
ϵ	dielectric constant
ϵ_0	permittivity of vacuum (8.85×10^{-12} F/m)
λ_{screen}	screening length of electron gas in metal
μ	magnetic moment
μ_B	Bohr magneton, unit of magnetic moment, $1\mu_B = 9.27 \times 10^{-24}$ J/T
$\mu_{molecular}$	molecular magnetic moment
ϕ	electron wavefunction
Ψ	electron wavefunction
ρ	Density of states
σ	electron spin wavefunction
Å	angstrom, unit of length, 1 Å = 10^{-10} m

SUMMARY

Magnetic properties of cobalt clusters ($20 \leq N \leq 200$) were studied in molecular beams. The magnetization of cobalt clusters is studied at a broad range of temperatures, magnetic fields and clusters sizes. It is shown that the magnetization of ferromagnetic clusters in a cluster beam can be understood as an adiabatic process using the avoided crossing theory. Besides the ground state that bears magnetic moment of about 2 μ_B per atom, an excited state that has 1 μ_B per atom was discovered for every cobalt cluster observed. The energy separations between the two states was investigated by photo-ionization experiments. The ionization threshold shows that the energy gap between the two states is on the order of 0.1 eV for small clusters ($N < 100$) and vanishes for larger clusters. Experiments also show that the polarizability of the excited state is lower than that of the ground state, which indicates a significant electronic structure difference between the two states. Two states are also found for iron clusters ($20 \leq N \leq 200$) for which the magnetic moments per atom are about 3 μ_B for the ground state and 1 μ_B for the excited states. This explains the fractional magnetic moments as well as the local magnetic order observed above the Curie temperatures for iron group ferromagnets. Further experiments show two states for manganese clusters for which the ground state has magnetic moment of 1 μ_B per atom in about the same size range. This suggests that the two states are a universal phenomenon of $3d$ transition metal clusters, which originate from the interaction between $3d$ and $4s$ electrons.

CHAPTER I

INTRODUCTION TO MAGNETISM

Why are iron, cobalt and nickel magnetic? It has been a subject of wonder for thousands of years. In history, many generations of theories of magnetism were developed. From superstition to classical theory to quantum mechanical theory, we are closer and closer to the truth. However, the theory is still not complete on this issue, due to the complexity of the problem. That is why the Heisenberg model and the Stoner model are used in text books to give an idea of ferromagnetism, although they both explain only part of the story.

In this chapter, the history of ferromagnetism is reviewed. Rather than enumerating great names and dreadful jargon, I will present the problems and theories of bulk systems side by side with those of the two atom system. The advantage is that the problem can be formulated and the Hamiltonian can be diagonalized under some assumptions which is not always possible for the bulk. This is not intended to downplay the importance of the complexity of bulk systems, but I do believe it is helpful for getting a fundamental picture.

1.1 Classical theory

The ancient Greeks knew about the attractive force of a loadstone to iron, which they explained by using mysterious spirits [115]. A later milestone discovery was that a suspended small magnet always orients in the same direction. This not only brought a breakthrough in navigation, but also led people to the idea of a magnetic field that is produced by the earth. Maxwell's seminal equations demonstrated that classical electrodynamics is complete on the macroscopic scale [78]: the important physical quantities like magnetic field, magnetic dipole moment and magnetization were all well-defined. The thermal properties of ferromagnets were described by Curie's law [39]: ferromagnets become paramagnetic above a critical temperature T_{Curie}, and the susceptibility χ is inversely proportional to temperature, thus $\chi \propto \frac{1}{T}$. To explain the paramagnetic behavior, Langevin proposed the idea that every

molecule or atom carries a magnetic moment $\mu_{molecular}$ [99]. By using Boltzman statistics, the average molecular moment under external field $B_{external}$ is

$$\begin{aligned}\langle\mu_{molecular}\rangle &= \mu_{molecular}\frac{\int\cos\theta e^{\frac{\mu_{molecular}B_{external}\cos\theta}{k_BT}}\sin\theta d\theta}{\int e^{\frac{\mu_{molecular}B_{external}\cos\theta}{k_BT}}\sin\theta d\theta} \\ &= \mu_{molecular}L(\frac{\mu_{molecular}B_{external}}{k_BT}),\end{aligned}$$

where $L(x) = coth(x) - \frac{1}{x}$ is the Langevin function. Because when $x \ll 1$, $L(x) = \frac{x}{3}$, at high temperature $\chi = \frac{N_m<\mu_{molecular}>}{VB_{external}} = \frac{N_m\mu^2_{molecular}}{V3k_BT}$, where N_m is the number of molecules and V is the volume.

Although Langevin's theory explained paramagnetism, ferromagnetism was still a mystery in the view of classical electrodynamics: if you put two macroscopic magnets with magnetic moments $\overrightarrow{\mu}_1$ and $\overrightarrow{\mu}_2$ side by side, they tend to antialign. This means the magnetic field that is given by dipole $\overrightarrow{\mu}_1$ and felt by $\overrightarrow{\mu}_2$ is

$$\overrightarrow{B}_1 = -a\overrightarrow{\mu}_1, \tag{1}$$

where a is a positive constant. Should the minus sign in (1) be positive, the two magnets would be aligned, which means a big ferromagnet could be considered as many small ferromagnets side by side. Intuitively Weiss [186] added one *ad hoc* assumption of a molecular field, stating that every molecule feels the molecular field that is given by all the other atoms in the same material. The molecular field

$$\overrightarrow{B}_{molecular} = \gamma_{molecular}\sum_i\overrightarrow{\mu}_i/V, \tag{2}$$

where $\overrightarrow{\mu}_i$ is the magnetic moment of ith molecule as a vector and more importantly $\gamma_{molecular}$ is a positive constant. Treating (2) with Langevin's theory selfconsistently, Weiss succeeded in explaining ferromagnetism phenomenologically using only one parameter $\gamma_{molecular}$. Transition from ferromagnet to paramagnet was predicted at $T_c = \frac{N_m}{V}\frac{\gamma_{molecular}\mu^2}{3k_B}$, where μ is the magnitude of the magnetic moment of every molecule. At low temperature, spontaneous magnetization is predicted. At high temperature, the susceptibility has the relation:

$$\chi = \frac{N_m}{V}\frac{\mu^2}{3k_B(T-T_c)}, \tag{3}$$

which is called the Curie Weiss law.

So far the Weiss mean field theory semi-quantitatively explained ferromagnetism. The theory is outstanding because it introduces only one parameter $\gamma_{molecular}$ and it works for all kinds of ferromagnets. The question that was left was: what is the origin of the molecular field? Actually, two unusual features of the molecular field were puzzling people: first the molecular field has a different sign from the dipole field, and second the molecular field is several orders of magnitude stronger than the dipole field. It turns out that quantum mechanics is the key to understanding the molecular field [181].

1.2 Quantum theory

1.2.1 Magnetic moment of atom

A major initial success of quantum mechanics for magnetism was to explain the origin of the atomic magnetic moment. It can be shown that for an electron in magnetic field B, an extra term will appear in the electron's Hamiltonian $H_{mag} = -g_{Lande}\mu_B J_z B$, where g_{Lande} is called the Lande factor, μ_B is the Bohr magneton (9.27×10^{-24} Am^2), and J_z is the projection of the angular momentum on the direction of the magnetic field ($-J \leq J_z \leq J$). The magnetic moment of an electron in a atom comes from the orbital motion ($\overrightarrow{L}$) and electronic spin ($\overrightarrow{S}$). The projection of magnetic moment on the field direction can be found from $\mu_z \equiv -\frac{\partial H_{mag}}{\partial B} = g_{Lande}\mu_B J_z$. The magnitude of the moment can be defined as the maximum projection $\mu \equiv \mu_z^{\max} = g_{Lande}\mu_B J$.

For the total angular momentum $\overrightarrow{J} = \overrightarrow{L} + \overrightarrow{S}$, the Lande factor

$$g_{Lande} = g_L \frac{J(J+1) - S(S+1) + L(L+1)}{2J(J+1)} + g_S \frac{J(J+1) + S(S+1) - L(L+1)}{2J(J+1)},$$

where $g_L = 1$ and $g_S = 2$ are Lande factors for the orbital angular momentum and the spin angular momentum, respectively.

The next question was how atoms combine their angular momenta. The prediction of the magnitude of the angular momentum that atoms have in their ground state is embodied by Hund's rules, which can be summarized as follows: for energy degenerate orbitals, electrons tend to be in different orbitals, spins of electrons tend to be aligned, and electrons tend to

have the largest total orbital angular momentum. These empirical rules can be explained by quantum mechanics.

Because of the Pauli exclusion principle, two or more electrons can never be in the same state. Although two electrons with different spin can occur in the same orbital, the Coulomb repulsion counteracts this tendency. Therefore, unless there are no empty orbitals with the same energy, atomic electrons avoid occurring in the same orbital. Suppose the two electrons are labeled a and b, the two orbitals can be expressed as wave function φ_1 and φ_2. Due to the the Pauli exclusion principle, the wave functions of the two electrons have to be antisymmetric. Considering both the orbital and the spin degrees of freedom, two choices for the wave function of the two electrons definitely satisfy the symmetry restriction: an antisymmetric spin part with a symmetric orbital part or a symmetric spin part with an antisymmetric orbital part. The orbital part of the two choices can be written as:

$$\begin{aligned}\Psi_S &= \frac{1}{\sqrt{2}}(\varphi_1(\overrightarrow{r}_a)\varphi_2(\overrightarrow{r}_b) + \varphi_1(\overrightarrow{r}_b)\varphi_2(\overrightarrow{r}_a)) \\ \Psi_A &= \frac{1}{\sqrt{2}}(\varphi_1(\overrightarrow{r}_a)\varphi_2(\overrightarrow{r}_b) - \varphi_1(\overrightarrow{r}_b)\varphi_2(\overrightarrow{r}_a)),\end{aligned}$$

where $\overrightarrow{r}_a$ and $\overrightarrow{r}_b$ are the coordinates of electron a and b, respectively. The total Hamiltonian of the two electrons is $H_{total} = H_a + H_b + \frac{e^2}{4\pi\epsilon_0|\overrightarrow{r}_a - \overrightarrow{r}_b|}$, where ϵ_0 is the vacuum dielectric constant, m_e is the mass of electron, and $H_a = \frac{\hbar^2}{2m_e}\bigtriangledown_a^2 - \frac{e^2}{4\pi\epsilon_0|\overrightarrow{r}_a|}$. The average energy of the two wave functions can be calculated

$$\langle\Psi_S|\, H_{total}\,|\Psi_S\rangle = 2E_{orbital} + C_{12} + J_{12} \text{ and} \tag{4}$$

$$\langle\Psi_A|\, H_{total}\,|\Psi_A\rangle = 2E_{orbital} + C_{12} - J_{12}, \tag{5}$$

where $E_{orbital}$ is the eigenenergy for orbital wave function φ_1 and φ_2 and

$$\begin{aligned}C_{12} &= \int\int \frac{e^2}{4\pi\epsilon_0\,|\overrightarrow{r}_a - \overrightarrow{r}_b|}\varphi_1^*(\overrightarrow{r}_a)\varphi_2^*(\overrightarrow{r}_b)\varphi_2(\overrightarrow{r}_b)\varphi_1(\overrightarrow{r}_a)d\overrightarrow{r}_a d\overrightarrow{r}_b \text{ and} \\ J_{12} &= \int\int \frac{e^2}{4\pi\epsilon_0\,|\overrightarrow{r}_a - \overrightarrow{r}_b|}\varphi_1^*(\overrightarrow{r}_a)\varphi_2^*(\overrightarrow{r}_b)\varphi_1(\overrightarrow{r}_b)\varphi_2(\overrightarrow{r}_a)d\overrightarrow{r}_a d\overrightarrow{r}_b\end{aligned}$$

are Coulomb and exchange integrals. On a specific atom, $J_{12} > 0$, so that Ψ_A is the more stable state, which means two spins are symmetric and hence they are aligned. This explains

why electrons' spins tend to be aligned. Note that the term J_{12} comes from the fact that electrons are indistinguishable Fermions, which is a purely quantum effect.

To explain the molecular field proposed by Weiss, one has to look at multi atom problems, of which the two-atom problem is the simplest.

1.2.2 Two-atom problem

Although the two-atom problem is not usually discussed in the chronology of magnetism, I will show here that it is very revealing for bulk magnetism.

Consider a system with two ion cores, A and B, and two electrons, a and b, the Hamiltonian of the system is

$$\begin{aligned} H &= \frac{\hbar^2}{2m_e}\bigtriangledown_a^2 - \frac{e^2}{4\pi\epsilon_0\,|\overrightarrow{r}_a - \overrightarrow{r}_A|} - \frac{e^2}{4\pi\epsilon_0\,|\overrightarrow{r}_a - \overrightarrow{r}_B|} \\ &\quad + \frac{\hbar^2}{2m_e}\bigtriangledown_b^2 - \frac{e^2}{4\pi\epsilon_0\,|\overrightarrow{r}_b - \overrightarrow{r}_A|} - \frac{e^2}{4\pi\epsilon_0\,|\overrightarrow{r}_b - \overrightarrow{r}_B|} \\ &\quad + \frac{e^2}{4\pi\epsilon_0\,|\overrightarrow{r}_a - \overrightarrow{r}_b|}. \end{aligned} \tag{6}$$

This Hamiltonian includes both electron-ion core and electron-electron interaction. The only approximation is that the two ion cores are fixed, which is the Born Oppenheimer approximation. Furthermore, it is a many body Hamiltonian.

Unfortunately, to solve the equation (6), we have to make further approximations based on the assumption that electron-ion core interaction is stronger than electron-electron interaction. In these approximations, we solve the electron-ion core Hamiltonian first and treat electron-electron interaction as a perturbation.

1.2.2.1 Localized electrons (Heitler-London approximation)

If two atoms are far apart, each electron stays on its atom most of the time. We can regroup the Hamiltonian as $H = H_a + H_b + H_{ab}$, where

$$\begin{aligned} H_a &= \frac{\hbar^2}{2m_e}\bigtriangledown_a^2 - \frac{e^2}{4\pi\epsilon_0\,|\overrightarrow{r}_a - \overrightarrow{r}_A|}, \\ H_b &= \frac{\hbar^2}{2m_e}\bigtriangledown_b^2 - \frac{e^2}{4\pi\epsilon_0\,|\overrightarrow{r}_b - \overrightarrow{r}_B|}, \text{ and} \\ H_{ab} &= -\frac{e^2}{4\pi\epsilon_0\,|\overrightarrow{r}_a - \overrightarrow{r}_B|} - \frac{e^2}{4\pi\epsilon_0\,|\overrightarrow{r}_b - \overrightarrow{r}_A|} + \frac{e^2}{4\pi\epsilon_0\,|\overrightarrow{r}_a - \overrightarrow{r}_b|}. \end{aligned}$$

If two atoms are the same, H_a and H_b have the same form but different coordinates. The solutions are atomic orbitals, ϕ_i $(i = 1, 2, ...)$ with energies E_i $(i = 1, 2, ...)$. Suppose ϕ_1 is the lowest energy state with energy E_1, for the lowest energy state, the space part of the wave functions of the two-electron system can be expressed as:

$$\begin{aligned}
\Psi_S &= \frac{1}{\sqrt{2}}(\phi_1(\overrightarrow{r}_a - \overrightarrow{r}_A)\phi_1(\overrightarrow{r}_b - \overrightarrow{r}_B) + \phi_1(\overrightarrow{r}_a - \overrightarrow{r}_B)\phi_1(\overrightarrow{r}_b - \overrightarrow{r}_A)) \\
\Psi_A &= \frac{1}{\sqrt{2}}(\phi_1(\overrightarrow{r}_a - \overrightarrow{r}_A)\phi_1(\overrightarrow{r}_b - \overrightarrow{r}_B) - \phi_1(\overrightarrow{r}_a - \overrightarrow{r}_B)\phi_1(\overrightarrow{r}_b - \overrightarrow{r}_A)),
\end{aligned}$$

where $\overrightarrow{r}_A$ and $\overrightarrow{r}_B$ are the coordinates of the two ion cores. Then the total energies are

$$\langle \Psi_S | H | \Psi_S \rangle = 2E_1 + C_{AB} + J_{AB} \quad (7)$$

$$\langle \Psi_A | H | \Psi_A \rangle = 2E_1 + C_{AB} - J_{AB}, \quad (8)$$

where

$$\begin{aligned}
C_{AB} &= \int\int H_{ab} |\phi_1(\overrightarrow{r}_a - \overrightarrow{r}_A)|^2 |\phi_1(\overrightarrow{r}_b - \overrightarrow{r}_B)|^2 d\overrightarrow{r}_a d\overrightarrow{r}_b \\
J_{AB} &= \int\int H_{ab}\phi_1(\overrightarrow{r}_a - \overrightarrow{r}_A)\phi_1^*(\overrightarrow{r}_b - \overrightarrow{r}_B)\phi_1(\overrightarrow{r}_a - \overrightarrow{r}_B)\phi_1(\overrightarrow{r}_b - \overrightarrow{r}_A)d\overrightarrow{r}_a d\overrightarrow{r}_b.
\end{aligned}$$

Note that, in this case J_{AB} can be either positive or negative. If $J_{AB} < 0$, Ψ_S has lower energy and two spins are aligned; if $J_{AB} > 0$, Ψ_A has lower energy and two spins are antialigned.

1.2.2.2 Itinerant electrons (molecular-orbital approximation)

If the distance between the two ion cores is small, the two electrons are evenly shared by the two ion cores. We regroup the total Hamiltonian as $H = H_a + H_b + H_{ab}$, where

$$\begin{aligned}
H_a &= \frac{\hbar^2}{2m_e}\bigtriangledown_a^2 - \frac{e^2}{4\pi\epsilon_0 |\overrightarrow{r}_a - \overrightarrow{r}_A|} - \frac{e^2}{4\pi\epsilon_0 |\overrightarrow{r}_a - \overrightarrow{r}_B|} \\
H_b &= \frac{\hbar^2}{2m_e}\bigtriangledown_b^2 - \frac{e^2}{4\pi\epsilon_0 |\overrightarrow{r}_b - \overrightarrow{r}_A|} - \frac{e^2}{4\pi\epsilon_0 |\overrightarrow{r}_b - \overrightarrow{r}_B|} \\
H_{ab} &= \frac{e^2}{4\pi\epsilon_0 |\overrightarrow{r}_a - \overrightarrow{r}_b|}.
\end{aligned}$$

We can solve the electron-ion core interaction H_a and H_b and consider H_{ab} as perturbation. H_a and H_b have the same form but different coordinates.

To solve H_a and H_b, one can start from the lowest atomic orbital ϕ_1, recombine atomic orbitals of iron cores A and B, and get two lowest energy solutions of H_a and H_b:

$$\xi_1(\overrightarrow{r}) = \frac{1}{\sqrt{2}}(\phi_1(\overrightarrow{r}-\overrightarrow{r}_A)+\phi_1(\overrightarrow{r}-\overrightarrow{r}_B)) \text{ and} \quad (9)$$

$$\xi_2(\overrightarrow{r}) = \frac{1}{\sqrt{2}}(\phi_1(\overrightarrow{r}-\overrightarrow{r}_A)-\phi_1(\overrightarrow{r}-\overrightarrow{r}_B)), \quad (10)$$

with energies $E_{\xi_1} = E_1 - t_{AB}$ and $E_{\xi_2} = E_1 + t_{AB}$, where

$$t_{AB} = \int \frac{e^2}{4\pi\epsilon_0 \left|\overrightarrow{r}_a - \overrightarrow{r}_B\right|} \phi_1^*(\overrightarrow{r}-\overrightarrow{r}_A)\phi_1(\overrightarrow{r}-\overrightarrow{r}_B)d\overrightarrow{r} > 0.$$

$\xi_1(\overrightarrow{r})$ and $\xi_2(\overrightarrow{r})$ are called molecular orbitals, and $\xi_1(\overrightarrow{r})$ is the lower energy state.

If the two electrons are both in the orbital ξ_1, the space part of the total wave function is symmetric, then the spin part has to be antisymmetric, thus, spins are antialigned. In this case, the total energy is

$$E_{total}^{\xi_1\xi_1} = 2E_1 - 2t_{AB} + C_{\xi_1\xi_1}, \quad (11)$$

where

$$C_{\xi_1\xi_1} = \int \frac{e^2}{4\pi\epsilon_0 \left|\overrightarrow{r}_a - \overrightarrow{r}_b\right|} \left|\xi_1(\overrightarrow{r}_a)\right|^2 \left|\xi_1(\overrightarrow{r}_b)\right|^2 d\overrightarrow{r}_a d\overrightarrow{r}_b \quad (12)$$

is the Coulomb energy between the two electrons in the same molecular orbital.

If we plug (9) and (10) into (12), we get 16 terms. Among this, the most important ones are those that are centered on the same atom. Thus,

$$\begin{aligned} C_{\xi_1\xi_1} &\approx \frac{1}{4}\int \frac{e^2}{4\pi\epsilon_0 \left|\overrightarrow{r}_a - \overrightarrow{r}_b\right|} \left|\phi_1(\overrightarrow{r}_a - \overrightarrow{r}_A)\right|^2 \left|\phi_1(\overrightarrow{r}_b - \overrightarrow{r}_A)\right|^2 d\overrightarrow{r}_a d\overrightarrow{r}_b \\ &\quad + \frac{1}{4}\int \frac{e^2}{4\pi\epsilon_0 \left|\overrightarrow{r}_a - \overrightarrow{r}_b\right|} \left|\phi_1(\overrightarrow{r}_a - \overrightarrow{r}_B)\right|^2 \left|\phi_1(\overrightarrow{r}_b - \overrightarrow{r}_B)\right|^2 d\overrightarrow{r}_a d\overrightarrow{r}_b \\ &= \frac{1}{2}C_{intra}, \end{aligned}$$

where

$$C_{intra} = \int \frac{e^2}{4\pi\epsilon_0 \left|\overrightarrow{r}_a - \overrightarrow{r}_b\right|} \left|\phi_1(\overrightarrow{r}_a - \overrightarrow{r}_A)\right|^2 \left|\phi_1(\overrightarrow{r}_b - \overrightarrow{r}_A)\right|^2 d\overrightarrow{r}_a d\overrightarrow{r}_b$$

is called intra-atomic Coulomb repulsion. Hence

$$E_{total}^{\xi_1\xi_1} \approx 2E_1 - 2t_{AB} + \frac{1}{2}C_{intra}. \quad (13)$$

If one electron is in orbital ξ_1 and the other in ξ_2, the space part also can be antisymmetric. This is very similar to the two-electron atom case we discussed in 1.2.1. The only difference is that ξ_1 and ξ_2 are not degenerate here, but that is not essential. Hence (5) and (4) apply and we get two possible energy states:

$$\begin{aligned} E_{total}^{A_{\xi_1\xi_2}} &= 2E_1 + C_{\xi_1\xi_2} - J_{\xi_1\xi_2} \text{ and} \\ E_{total}^{S_{\xi_1\xi_2}} &= 2E_1 + C_{\xi_1\xi_2} + J_{\xi_1\xi_2}, \end{aligned}$$

where

$$\begin{aligned} C_{\xi_1\xi_2} &= \int \frac{e^2}{4\pi\epsilon_0 \left|\overrightarrow{r}_a - \overrightarrow{r}_b\right|} \left|\xi_1(\overrightarrow{r}_a)\right|^2 \left|\xi_2(\overrightarrow{r}_b)\right|^2 d\overrightarrow{r}_a d\overrightarrow{r}_b \\ &\approx \frac{1}{4}\int \frac{e^2}{4\pi\epsilon_0 \left|\overrightarrow{r}_a - \overrightarrow{r}_b\right|} \left|\phi_1(\overrightarrow{r}_a - \overrightarrow{r}_A)\right|^2 \left|\phi_1(\overrightarrow{r}_b - \overrightarrow{r}_A)\right|^2 d\overrightarrow{r}_a d\overrightarrow{r}_b \\ &\quad + \frac{1}{4}\int \frac{e^2}{4\pi\epsilon_0 \left|\overrightarrow{r}_a - \overrightarrow{r}_b\right|} \left|\phi_1(\overrightarrow{r}_a - \overrightarrow{r}_B)\right|^2 \left|\phi_1(\overrightarrow{r}_b - \overrightarrow{r}_B)\right|^2 d\overrightarrow{r}_a d\overrightarrow{r}_b \\ &= \frac{1}{2} C_{intra}, \end{aligned}$$

is the Coulomb repulsion when two electrons are in different orbitals and

$$\begin{aligned} J_{\xi_1\xi_2} &= \int \frac{e^2}{4\pi\epsilon_0 \left|\overrightarrow{r}_a - \overrightarrow{r}_b\right|} \xi_1^*(\overrightarrow{r}_a)\xi_2^*(\overrightarrow{r}_b)\xi_1(\overrightarrow{r}_b)\xi_2(\overrightarrow{r}_a) d\overrightarrow{r}_a d\overrightarrow{r}_b \\ &\approx \frac{1}{2} C_{intra} \end{aligned}$$

is the corresponding exchange integral. Hence

$$\begin{aligned} E_{total}^{A_{\xi_1\xi_2}} &\approx 2E_1 \text{ and} \\ E_{total}^{S_{\xi_1\xi_2}} &\approx 2E_1 + C_{intra}. \end{aligned} \tag{14}$$

If we compare $E_{total}^{A_{\xi_1\xi_2}}$ and $E_{total}^{\xi_1\xi_1}$ using (13) and (14), we find that if $C_{intra} > 4t_{AB}$, one should expect $E_{total}^{A_{\xi_1\xi_2}}$ as the lowest energy. In other words, two spins will be aligned.

1.2.3 Bulk

1.2.3.1 Hamiltonian and wave functions of many electrons

It is important to clarify one difference between the magnetism of atoms and bulk for the iron group metal. Because of the electric field from neighboring atoms, angular momentum

is no longer a good quantum number for the atomic orbitals. Therefore, the orbital angular momentum does not contribute to the magnetic moment of an atom in the bulk. This is called orbital quenching [87] [177] [13]. In that case almost all of the angular momentum (and hence the magnetic moment) in a solid is from the spin.

In two-electron problems, we argued that the space and spin degrees of freedom can be treated separately and then combined together to get an antisymmetric wave function. However, it does not have to be that way. Suppose there are electrons in states $\{\varphi_I, I = A, B, C...\}$ including spin and space degrees of freedom, a possible wave function that satisfies the Pauli exclusion principle is the Slater determinant [46]:

$$\Psi = \begin{vmatrix} \varphi_A(r_1) & \varphi_A(r_2) & \varphi_A(r_3) & ... \\ \varphi_B(r_1) & \varphi_B(r_2) & \varphi_B(r_3) & ... \\ \varphi_C(r_1) & \varphi_C(r_2) & \varphi_C(r_3) & ... \\ ... & ... & ... & ... \end{vmatrix}.$$

Consider the many electron Hamiltonian $H_{many} = \sum H_{single} + \sum\sum H_{int}$, where H_{single} is the single electron Hamiltonian and H_{int} is the Hamiltonian for interaction between two electrons. Because it is impossible to solve H_{many}, we have to solve H_{single} first and use the eigenfunctions of H_{single} to form all possible Slater determinants. Using these determinants as basis, we can include the interactions H_{int} and solve the problem.

If H_{single} is spin independent and $\{\phi_i\}$ are the eigenfunctions of H_{single}, the basis for many body problem will be

$$\Psi = \begin{vmatrix} \phi_a(r_1)\sigma_1 & \phi_a(r_2)\sigma_2 & \phi_a(r_3)\sigma_3 & ... \\ \phi_b(r_1)\sigma_1 & \phi_b(r_2)\sigma_2 & \phi_b(r_3)\sigma_3 & ... \\ \phi_c(r_1)\sigma_1 & \phi_c(r_2)\sigma_2 & \phi_c(r_3)\sigma_3 & ... \\ ... & ... & ... & ... \end{vmatrix}, \tag{15}$$

for all possible combinations of $\{\phi_i, i = a, b, c...\}$, where σ_i is the wave function of the spin part for *ith* electron. A further step of approximation is to look at only the diagonal term of the Hamiltonian $\langle\Psi| H_{many} |\Psi\rangle$, like what we have done for the two atom problem. It turns out that the on-diagonal energy is

$$\langle\Psi| H_{many} |\Psi\rangle = E_{\sin gle} + E_{Coulomb} - E_{exchange}, \tag{16}$$

where E_{single}=$\sum_i \langle\phi_i| H_{single} |\phi_i\rangle$ is the summation of all the single electron energy,

$$\begin{aligned} E_{Coulomb} &= \sum_{i,j} \int\int H_{int} \left|\phi_i(\overrightarrow{r}_1)\right|^2 \left|\phi_j(\overrightarrow{r}_2)\right|^2 d\overrightarrow{r}_1 d\overrightarrow{r}_2 \\ &= \sum_{i,j} C_{ij} \end{aligned}$$

is the Coulomb interaction energy and

$$\begin{aligned} E_{exchange} &= \sum_{i,j} \delta_{\sigma_1,\sigma_2} \int\int H_{int} \phi_i(\overrightarrow{r}_1) \phi_j^*(\overrightarrow{r}_2) \phi_j(\overrightarrow{r}_1) \phi_i^*(\overrightarrow{r}) d\overrightarrow{r}_1 d\overrightarrow{r}_2 \\ &= \sum_{i,j} \delta_{\sigma_1,\sigma_2} J_{ij} \end{aligned}$$

is the exchange interaction energy. Note that the exchange energy is non-zero only when the two electrons are in the same spin states due to the Dirac delta function $\delta_{\sigma_1,\sigma_2}$. The exchange integral is $J_{ij} > 0$, which means the exchange energy favors a parallel spin orientation.

After this formal introduction, we return to the original question: what is the origin of the molecular field of the Weiss theory? Clearly, quantum mechanics should give the answer, especially considering its success in explaining the magnetic moments of atoms.

1.2.3.2 Heisenberg's localized electron model

Starting from the Heitler-London approximation of the two-atom problem, Heisenberg proposed his famous theory of magnetism [69]. In his theory, electrons are localized. In other words, every electron is bonded to a special atom. Electron-electron interactions are treated only as perturbations. He summarized the correlation between the total energy of the two atoms and the alignment of their spins with the following Hamiltonian:

$$H_{Heisenberg} = -J_{AB}(\overrightarrow{S}_A \cdot \overrightarrow{S}_B + \frac{1}{2}). \tag{17}$$

It is easy to verify that if two spins are aligned then $\overrightarrow{S}_A \cdot \overrightarrow{S}_B = \frac{1}{2}$, and if they are antialigned then $\overrightarrow{S}_A \cdot \overrightarrow{S}_B = \frac{3}{2}$.

Dirac [47] showed the derivation of (17) using many body theory for the spin $\frac{1}{2}$ case. Later Anderson showed that (17) works for the multi-electron atoms case as well [6], which means that S_A and S_B can be more than $\frac{1}{2}$. It is easy to expand this model from the two

atom case to the bulk:

$$H_{Heisenberg} = -J_{ij} \sum_{i,j} \overrightarrow{S}_i \cdot \overrightarrow{S}_j, \tag{18}$$

where $\overrightarrow{S}_i$ is the spin for ith atom and the constant $\frac{1}{2}$ is neglected. Heisenberg argued in his model, that the most important terms are the nearest neighbor terms. The sign of J_{ij} determines whether the material is ferromagnetic or antiferromagnetic. If we make a further step in (18) by replacing one of the spin operators with its average value, we get

$$H_{Heisenberg} \approx -J_{ij} \sum_{i,j} \overrightarrow{S}_i \cdot \left\langle \overrightarrow{S}_j \right\rangle = -J_{ij} N_a \left\langle \overrightarrow{S} \right\rangle \cdot \sum_i \overrightarrow{S}_i, \tag{19}$$

where N_a is the number of atoms. This is actually the Weiss molecular field model. The strong molecular field comes from the exchange interaction between electrons.

It appeared that the origin of the molecular field was explained and that the theory was complete. However, it turns out that Heisenberg model can only explain magnetism in insulators. For iron, cobalt and nickel, experiments showed that magnetic moment per atom in Bohr magnetons unit is fractional [189]. As we pointed out in 1.2.3.1, the magnetic moment is entirely due to electronic spin. In the localized electron model, the magnetic moment per atom should be an integer number. On the other hand, subsequent calculations of the exchange integral showed that both its sign and its magnitude are inconsistent with a ferromagnetic alignment of spins for iron group ferromagnets [201].

Because Heisenberg looked at localized electrons, the spin alignment is not included in the electrons' kinetic energy. Instead, it is determined by the sign of the exchange integral. However if we look at itinerant electrons, the exchange integral is always positive, which always favors parallel spin. In that case, the spin alignment will indeed change the distribution of the electrons in the Fermi sea and in turn increase the total single electron energy. Therefore, ferromagnetism actually results from the competition between the exchange energy and the single electron energy.

1.2.3.3 Bloch's free electron model

Just one year later, Bloch [24] attacked the problem from the point of view of itinerant electrons. Instead of discussing localized electrons in an ionic background, he investigated

the free electron gas. For the free electron gas model, we can calculate $E_{Coulomb}$ and $E_{exchange}$. In this case $\phi_i = \frac{1}{\sqrt{V}} e^{-i\overrightarrow{k}_i \cdot \overrightarrow{r}}$, then we find the Coulomb integral:

$$\begin{aligned} C_{ij} &= \frac{1}{V^2}\int H_{int} \left|\phi_i\right|^2 \left|\phi_j\right|^2 d\overrightarrow{r}_1 d\overrightarrow{r}_2 \\ &= \frac{1}{V^2}\int H_{int} d\overrightarrow{r}_1 d\overrightarrow{r}_2 \\ &= \frac{1}{V^2}\int \frac{e^2}{4\pi\epsilon_0 \left|\overrightarrow{r}_1 - \overrightarrow{r}_2\right|} d\overrightarrow{r}_1 d\overrightarrow{r}_2, \end{aligned}$$

is a constant, and the exchange integral is:

$$\begin{aligned} J_{ij} &= \frac{1}{V^2}\int H_{int} e^{-i\overrightarrow{k}_i \cdot \overrightarrow{r}_1} e^{-i\overrightarrow{k}_j \cdot \overrightarrow{r}_2} e^{i\overrightarrow{k}_i \cdot \overrightarrow{r}_2} e^{i\overrightarrow{k}_j \cdot \overrightarrow{r}_1} d\overrightarrow{r}_1 d\overrightarrow{r}_2 \\ &= \frac{1}{V^2}\int H_{int} e^{-i(\overrightarrow{k}_i - \overrightarrow{k}_j)\cdot(\overrightarrow{r}_1 - \overrightarrow{r}_2)} d\overrightarrow{r}_1 d\overrightarrow{r}_2 \\ &= \frac{1}{V^2}\int \frac{e^2}{4\pi\epsilon_0 \left|\overrightarrow{r}_1 - \overrightarrow{r}_2\right|} e^{-i(\overrightarrow{k}_i - \overrightarrow{k}_j)\cdot(\overrightarrow{r}_1 - \overrightarrow{r}_2)} d\overrightarrow{r}_1 d\overrightarrow{r}_2. \end{aligned} \tag{20}$$

Because the exchange energy between two electrons vanishes when their spins are not the same, we can discuss the total exchange energy of the spin-up and the spin-down cases separately. Suppose that the largest wave vectors for the two spin orientations are $k_\uparrow^0 = (\frac{3N_\uparrow}{4\pi V})^{\frac{1}{3}}$ and $k_\downarrow^0 = (\frac{3N_\downarrow}{4\pi V})^{\frac{1}{3}}$, where $N_\uparrow$ and $N_\downarrow$ are the number of electrons with spin up and spin down, respectively, one can calculate the exchange energy

$$\begin{aligned} E_{exchange}^{\uparrow} &= \sum_{i,j} J_{ij}^{\uparrow} = \frac{e^2}{\epsilon_0} V (k_\uparrow^0)^4 = \frac{e^2}{4\pi\epsilon_0} \frac{3^{\frac{4}{3}}}{(4\pi V)^{\frac{1}{3}}} N_\uparrow^{\frac{4}{3}} \text{ and} \\ E_{exchange}^{\downarrow} &= \sum_{i,j} J_{ij}^{\downarrow} = \frac{e^2}{\epsilon_0} V (k_\downarrow^0)^4 = \frac{e^2}{4\pi\epsilon_0} \frac{3^{\frac{4}{3}}}{(4\pi V)^{\frac{1}{3}}} N_\downarrow^{\frac{4}{3}}. \end{aligned} \tag{21}$$

The total single-electron energy depends on the electron population, which gives

$$E_{single} = \frac{3^{\frac{5}{3}}\hbar^2}{10 m_e (4\pi V)^{\frac{2}{3}}} (N_\uparrow^{\frac{5}{3}} + N_\downarrow^{\frac{5}{3}}).$$

Thus the total energy is

$$\begin{aligned} & E_{single} + E_{Coulomb} + E_{exchange}^{\uparrow} + E_{exchange}^{\downarrow} \\ = \; & constant + \frac{3^{\frac{5}{3}}\hbar^2}{10 m (4\pi V)^{\frac{2}{3}}} (N_\uparrow^{\frac{5}{3}} + N_\downarrow^{\frac{5}{3}}) - \frac{e^2}{4\pi\epsilon_0} \frac{3^{\frac{4}{3}}}{(4\pi V)^{\frac{1}{3}}} (N_\uparrow^{\frac{4}{3}} + N_\downarrow^{\frac{4}{3}}). \end{aligned} \tag{22}$$

Bloch argued that as long as the density of the electron gas is small enough, the third term in (22) will be dominant and align the spin of the electron system. The critical density of

the electron gas $\frac{N_e}{V}$ can be estimated to be on the order of $\frac{1}{100V_{Bohr}}$, where V_{Bohr} is the volume of the sphere with one Bohr radius. This is much smaller than typical density of free electrons of in a metal.

1.2.3.4 Wigner lattice and electron-electron correlation

Wigner showed that the dilute electron gas will actually localize to form a lattice before the spins aligns [187]. It is crucial to understand this issue because this is the first time electron-electron correlations were brought up with respect to magnetism. We will see below that this issue is extremely important. The term "electron-electron correlation" may be confusing because we are already talking about the Coulomb interactions between electrons. A two electron example can clear this confusion.

First we should reconsider and see the approximation we have made to reach to the formula (16) for the total energy: (i) we started from the single-electron eigenfunctions as basis and (ii) we used the on-diagonal terms of the Hamiltonian to represent the total energies, rather than finding the real eigenenergies of the many-body system. We cannot do anything about (i), but for a system of only two electrons, we certainly can do better than (ii).

Assuming two electrons in single-electron states, ϕ_{k_1} and ϕ_{k_2}, we can write down the many-body basis using second quantization representation: $|\uparrow\downarrow\rangle_{k_1}|\rangle_{k_2}$, $|\uparrow\rangle_{k_1}|\uparrow\rangle_{k_2}$, $|\uparrow\rangle_{k_1}|\downarrow\rangle_{k_2}$, $|\downarrow\rangle_{k_1}|\uparrow\rangle_{k_2}$, $|\downarrow\rangle_{k_1}|\downarrow\rangle_{k_2}$ and $|\rangle_{k_1}|\uparrow\downarrow\rangle_{k_2}$, where $|\uparrow\rangle_{k_1}$ denotes a spin up electron in ϕ_{k_1} and so forth. Subsequently, we can write down the Hamiltonian H_{k_1,k_2} :

$$\frac{1}{2}\begin{bmatrix} 2C_{1111} & 0 & \begin{matrix}C_{1121}\\ +C_{1112}\end{matrix} & \begin{matrix}-C_{1112}\\ -C_{1121}\end{matrix} & 0 & 2C_{1122} \\ 0 & \begin{matrix}C_{1221}+C_{2112}\\ -C_{1212}-C_{2121}\end{matrix} & 0 & 0 & 0 & 0 \\ \begin{matrix}C_{2111}\\ +C_{1211}\end{matrix} & 0 & \begin{matrix}C_{1221}\\ +C_{2112}\end{matrix} & \begin{matrix}-C_{1212}\\ -C_{2121}\end{matrix} & 0 & \begin{matrix}C_{2122}\\ +C_{1222}\end{matrix} \\ \begin{matrix}-C_{1211}\\ -C_{2111}\end{matrix} & 0 & \begin{matrix}-C_{2121}\\ -C_{1212}\end{matrix} & \begin{matrix}C_{2112}\\ +C_{1221}\end{matrix} & 0 & \begin{matrix}-C_{1222}\\ -C_{2122}\end{matrix} \\ 0 & 0 & 0 & 0 & \begin{matrix}C_{2112}+C_{1221}\\ -C_{2121}-C_{1212}\end{matrix} & 0 \\ 2C_{2211} & 0 & \begin{matrix}C_{2221}\\ +C_{2212}\end{matrix} & \begin{matrix}-C_{2212}\\ -C_{2221}\end{matrix} & 0 & 2C_{2222} \end{bmatrix}, \tag{23}$$

where

$$C_{ijkl} = \int\int \frac{e^2}{4\pi\epsilon_0 \left|\overrightarrow{r}_1 - \overrightarrow{r}_2\right|} \phi^*_{k_i}(\overrightarrow{r}_1)\phi^*_{k_j}(\overrightarrow{r}_2)\phi_{k_k}(\overrightarrow{r}_2)\phi_{k_l}(\overrightarrow{r}_1) d\overrightarrow{r}_1 d\overrightarrow{r}_2.$$

If we only consider the on-diagonal term, only the pure Coulomb repulsion terms C_{1111}, C_{2222}, C_{1221}, C_{1212} and the exchange interaction terms C_{1212} and C_{2121} are involved, and we are back to Bloch's model. We can verify that for all the basis states (using plane wave), the charge density $\widehat{\rho}(\overrightarrow{r}) = \sum_{i,j} \phi^*_{k_i}(\overrightarrow{r})\phi_{k_j}(\overrightarrow{r}) a^+_{k_i} a_{k_j}$ is constant over the space, where a_{k_j} is the annihilation operator for state ϕ_{k_j}. However, if we diagonalize the Hamiltonian, we will mix these basis states, giving rise to non-uniform charge distribution because of off-diagonal terms. This is actually the electron-electron correlation, resulting from the Coulomb interaction.

Another way to see this issue is to note that when we only look at the on-diagonal energies, only the Coulomb repulsions of electrons with parallel spin but not those with antiparallel spins, are taken into account.

Interestingly enough, if we diagonalize the Hamiltonian of the Heitler-London model, we find that (7) and (8) are actually the eigenenergies. The reason is that the Heitler-London

approximation assumes localized electrons, which implicitly takes care of the electron-electron correlations. That is why in the the Heisenberg model, electron-electron correlations is not a problem.

1.2.3.5 Stoner's tight-binding electron model

Bloch's argument is not valid because he studied the oversimplified case of the free electron gas. Real itinerant electrons do not necessarily have the same density of states as the free electron gas. According to Bloch's theory, to get a system with aligned spins, all we need is that at the Fermi surface, changing spin population should not affect single electron energy too much. A high density of states at the Fermi surface will satisfy this condition [188].

Stoner and Wohlfarth [169] [188] looked at the spin alignment of electrons that are more tightly bonded to atoms. This corresponds to the molecular-orbital approximation of the two atom problem in 1.2.2.2. In the case of many electrons,

$$E_{single} = \int_0^{E_\uparrow^{\max}} DOS(E)EdE + \int_0^{E_\downarrow^{\max}} DOS(E)EdE,$$

where $E_\uparrow^{\max}$ and $E_\downarrow^{\max}$ are the highest energies occupied by spin-up and spin-down electrons, respectively, and

$$E_{exchange} = \frac{1}{4}N_\uparrow^2 C_{intra} + \frac{1}{4}N_\downarrow^2 C_{intra}.$$

The Coulomb energy does not depend on the spin population.

Assuming a small spin imbalance at Fermi surface $\Delta N_e = N_\uparrow - N_\downarrow$, the single electron energy increases by $\frac{\Delta N_e^2}{4DOS(E_F)}$, and the exchange energy decreases by $\frac{1}{8}\Delta N_e^2 C_{intra}$, the total energy change is

$$\frac{\Delta N_e^2}{4DOS(E_F)} - \frac{1}{8}\Delta N_e^2 C_{intra} = (\frac{2}{DOS(E_F)} - C_{intra})\frac{\Delta N_e^2}{8}. \quad (24)$$

Therefore as long as $\frac{DOS(E_F)C_{intra}}{2} > 1$, the spin imbalanced case is more energy efficient. This is called the Stoner Criteria. As mentioned in 1.2.3.3, a high density of states at the Fermi surface will cause spin alignment and in turn ferromagnetism.

To compare with the Heisenberg model, we write the total energy of the tight-binding itinerant electrons at the Fermi surface as

$$H_{Stoner} = E_{single} + E_{exchange} = -J_{k_1k_2}\sum_{k_1,k_2} \overrightarrow{S}_{k_1} \cdot \overrightarrow{S}_{k_2}, \quad (25)$$

where $J_{k_1k_2} = -(\frac{2}{DOS(E_F)} - C_{intra})$, and k_1 and k_2 are the indices for the itinerant electrons.

Stoner's model answered the question that can not be explained by the Heisenberg model: why is the magnetic moment per atom fractional if the magnetic moment comes from electronic spins? In this respect, the model is very successful, which explains why it is still invoked in text books to explain itinerant ferromagnetism. Unfortunately, this is only part of the story. It turns out that Stoner's model fails to explain the thermal properties of the ferromagnets [128]. For example, the transition temperature calculated by Stoner's model is several times higher than the experimental value [31] and it fails to yield the Curie Weiss law at high temperature. All of these directly suggest some validity of the localized magnetic moment picture.

Another controversy that was added to the above problems is the inconsistency between the low temperature saturation magnetization and the high temperature magnetic moment. By definition, the magnetic moment per atom is determined from the low temperature saturation magnetization. This is called $\mu_{saturation}$, which can be measured. For iron, cobalt and nickel, the values are $2.1\mu_B$, $1.7\mu_B$ and $0.6\mu_B$, respectively. In addition for all ferromagnetic material, the high temperature paramagnetic behavior follows the Curie Weiss law (3). Therefore one can also calculate the magnetic moment per atom from (3), which is called $\mu_{CurieWeiss}$. For iron, cobalt and nickel, the values are $2.2\mu_B$, $2.3\mu_B$ and $0.9\mu_B$ [189], respectively. The fact that the ratios $\mu_{saturation}/\mu_{CurieWeiss}$ significantly deviate from unity complicates the problem. Apparently, purely localized electron and itinerant electron models are not good enough. The truth must lie in between.

1.2.3.6 Zener's indirect exchange model

To resolve this issue, Zener proposed his model [200] [201], which included both itinerant and localized electrons. In his model, $3d$ electrons are localized and carry magnetic moments, the $4s$ electrons are itinerant and responsible for aligning these local moments. The interaction between the $3d$ electrons are like (18) $\sum_{i,j} J_{ij} \overrightarrow{S}_i \cdot \overrightarrow{S}_j$, and the interaction between $4s$ electrons are like (25) $\sum_{k_1,k_2} J_{k_1k_2} \overrightarrow{S}_{k_1} \cdot \overrightarrow{S}_{k_2}$. Zener argued that J_{ij} and $J_{k_1k_2}$ are all positive, so that these interactions favor antialignment of the electronic spins. However, Zener introduced

one more term $-\sum_{i,k} J_{ik} \overrightarrow{S}_i \cdot \overrightarrow{S}_{k_1}$, where J_{ik} is a positive number. Therefore the total energy is

$$H_{Zener} = \sum_{i,j} J_{ij} \overrightarrow{S}_i \cdot \overrightarrow{S}_j + \sum_{k_1,k_2} J_{k_1 k_2} \overrightarrow{S}_{k_1} \cdot \overrightarrow{S}_{k_2} - \sum_{i,k_1} J_{ik} \overrightarrow{S}_i \cdot \overrightarrow{S}_{k_1}. \tag{26}$$

Replacing $\overrightarrow{S}_{k_1}$ with their average (just like introducing the molecular field in (19)), (26) becomes

$$H_{Zener} = \sum_{i,j} J_{ij} \overrightarrow{S}_i \cdot \overrightarrow{S}_j + \sum_{k_1,k_2} J_{k_1 k_2} \left\langle \overrightarrow{S}_{k_1} \right\rangle \cdot \left\langle \overrightarrow{S}_{k_2} \right\rangle - \sum_{i,k_1} J_{ik_1} \overrightarrow{S}_i \cdot \left\langle \overrightarrow{S}_{k_1} \right\rangle. \tag{27}$$

Minimizing H_{Zener} by requiring that $\frac{\partial H_{Zener}}{\partial \left\langle \overrightarrow{S}_{k_1} \right\rangle} = 0$, one gets

$$\left\langle \overrightarrow{S}_{k_1} \right\rangle = \frac{\sum_i J_{ik_1} \overrightarrow{S}_i}{2\sum_{k_2} J_{k_1 k_2}}. \tag{28}$$

Plugging in (27) back to (28), one finds the effective Hamiltonian

$$H^{eff}_{Zener} = \sum_{i,j} (J_{ij} - \sum_{k_1,k_2} J_{k_1 k_2} \frac{J_{ik_1} J_{jk_2}}{4\sum_{k'_2} J_{k_1 k'_2} \sum_{k'_1} J_{k'_1 k_2}}) \overrightarrow{S}_i \cdot \overrightarrow{S}_j.$$

As long as $(J_{ij} - \sum_{k_1,k_2} J_{k_1 k_2} \frac{J_{ik_1} J_{jk_2}}{4\sum_{k'_2} J_{k_1 k'_2} \sum_{k'_1} J_{k'_1 k_2}}) < 0$, the aligned spin configuration will have lower energy. Zener's model was proposed to explain the ferromagnetism of iron group metals. However, the measured magnetic moments per atom do not satisfy the assumption of completely localized $3d$ electrons, and more importantly, the polarization of $4s$ electrons required by the model takes a significant amount of energy [180]. Actually, a refined version of Zener's model better explains the ferromagnetism of rare earth metals, where the $4f$ electrons are well-localized and their mutual interactions are mediated by the $5s$ electrons. The only difference is that the $5s$ electrons are polarized, not uniformly as in Zener's model but rather in an oscillating way. The effective interaction between 4f electrons are called the RKKY (Ruderman, Kittel, Kasuya and Yosida) [158] [85] [198] interaction.

1.2.3.7 Huewitz-van Vleck's minimum polarity model

Huewitz and van Vleck [77] [178] [180] also noticed the defects of the purely localized electron and the purely itinerant electron model, so they introduced a hybrid model that

they called the generalized Heisenberg model or the minimum polarity model. Instead of utilizing $4s$ electrons to align the spins, they argued that a fraction of the $3d$ electrons are also itinerant and can mediate interactions between the spins on different atoms. In fact, this is a hybridization of the Heisenberg model and the Stoner's model. In Stoner model, all of the $3d$ electrons are itinerant, which does not exclude the high-polarity states (e.g., $3d^0$, $3d^1$) in which atoms lose many electrons. In the generalized Heisenberg model, only the minimum polarity states are allowed. Most $3d$ electrons are localized and carry magnetic moments according to the Hund's rule. Only a few itinerant 3d electrons migrate between atoms. They are responsible for the interactions between the localized magnetic moments which need not be the same for all atoms. This model reconciled the fractional magnetic moments per atom with the properties that indicate the existence of localized magnetic moments.

We will show how it works for nickel and cobalt. For cobalt, atoms fluctuate between $3d^8$ and $3d^9$ polarity states by sharing itinerant electrons. Because of the Hund's rule, the shared electrons tend to align the spins of different atoms. Nickel is a little more complicated since three polarity states ($3d^8$, $3d^9$ and $3d^{10}$) are involved. Again the presence of $3d^8$ and $3d^9$ states are responsible for aligning the spins. The excess energy in this higher polarity state is believed to be compensated by the screening of the $4s$ electrons. It is not difficult to see that by applying this model to a nearly full or a nearly empty d shell, we get ferromagnetic behavior. For about half-filled d shells, we should get antiferromagnetic behavior.

The minimum polarity model is a qualitative model, because it is not possible to carry out quantitative calculations to compare with experimental results. However it is very important because it implies the existence of the local moments in iron group ferromagnets. Along this line, people tried to elaborate or refine this model to make it quantitative.

1.2.3.8 Hubbard model

The Hubbard model [74] plays a critical role in the history of ferromagnetism. Later theories, whether edging towards localized or itinerant magnetic moment picture, were all based on this model. The idea was simply to include the electron-electron correlations, as mentioned

in 1.2.3.4. It is trivial to write down the Hamiltonian of Hubbard model using the second quantization representation:

$$H_{Hubbard} = t_{H0}\sum_{i\sigma} n_{i\sigma} - t_{H1}\sum_{ij\sigma}(C^{+}_{i\sigma}C_{j\sigma} + C^{+}_{j\sigma}C_{i\sigma}) + U_{Hubbard}\sum_{i\sigma} n_{i\sigma}n_{i\bar{\sigma}}, \tag{29}$$

where $C_{i\sigma}$ is the annihilation operator of an atomic orbital i with spin σ, $n_{i\sigma}$ is the electron electrons operator at atomic orbital i with spin σ and t_{H0}, t_{H1} and $U_{Hubbard}$ are respectively single electron energy of the atomic orbital, the hopping energy between atomic orbitals and the electronic repulsion for electrons on the same atomic orbital. We can understand the Hubbard model for the two-electron problem we elaborated in 1.2.3.4. If the two states are the molecular orbitals in 1.2.2.2, we can use the same approximation there, thus only the intra-atomic interactions are considered for the electron-electron Coulomb repulsion. Then (23) becomes

$$H_{\xi 1\xi 2} = \frac{1}{2}\begin{bmatrix} C_{intra} & 0 & 0 & 0 & 0 & C_{intra} \\ 0 & 0 & 0 & 0 & 0 & 0 \\ 0 & 0 & C_{intra} & C_{intra} & 0 & 0 \\ 0 & 0 & C_{intra} & C_{intra} & 0 & 0 \\ 0 & 0 & 0 & 0 & 0 & 0 \\ C_{intra} & 0 & 0 & 0 & 0 & C_{intra} \end{bmatrix}, \tag{30}$$

which is actually the Hubbard model with the same single electron energy and $U_{Hubbard} = C_{intra}$. Note that (30) is in the molecular orbital space or reciprocal space, while (29) is in real space, which is more often used because of its simple form. Comparing Eq. (30) with (23), we see that some of off-diagonal terms that are ignored in the Stoner model are kept, which improves the validity of the model. The Hubbard model immediately resolved a paradox pointed out by Slater [165] for the Stoner model. The paradox was that in the Stoner model, if electrons are very far apart, the band width of "itinerant" electrons must be very narrow, yielding high density of states that favors the alignment of the spins since that minimizes the on-diagonal energy (24). This is contrary to common sense: two distant electrons should not care about their relative spin alignment at all. If we diagonalize (30), we find that both the antialigned state and the aligned state are ground states. This resolves the paradox.

The Hubbard model takes into account additional necessary interaction terms. However, diagonalizing the Hubbard Hamiltonian is not trivial at all. A further approximation has to be made in order to make the problem tractable. It is trivial to show that the mean field treatment will reduce the Hubbard model to the Stoner's model. Since mean field theory ignores the necessary terms, better ways have to be found. Again alternate approaches were adapted.

At this point, I am forced to only sketch the basic ideas because it is extremely complicated to formulate the approximations which in fact are not in the Hamiltonian but rather in the technique of diagonalizing the Hamiltonian.

1.2.3.9 Disordered local moment theory (DLM)

Following the original suggestion of van Vleck, Hubbard and others [40] [75] [76] [163] [167] believed in the existence of local magnetic moments. The localized moment model was fortified by the fact that dilute magnetic atoms in some nonmagnetic materials in fact do develop local moments, as later explained by Anderson [5] [7] [190] using an $s - d$ mixing mechanism based on the Hubbard model.

In his theory, Hubbard introduced the local exchange field which may fluctuate vertically and transversely along the magnetic moments. Vertical fluctuations correspond to changes in the magnitude of the spin due to the itinerancy of electrons, and transverse fluctuations correspond to spin reorientation, much like in Heisenberg's picture.

Two energy scales were suggested by this model. The first is a fluctuation of the magnitude of the spin that is on the order of an eV because it results from the itinerant nature of the electrons. The second one is due to the alignment of these local spins. This is on the order of one-tenth of eV. The latter will behave like Heisenberg localized spin interaction and will cause the phase transition to the ferrimagnetically ordered state.

In this theory, both the local and itinerant properties of electrons are taken into account, and several controversies were resolved qualitatively. The fractional magnetic moment per atom was explained as by the magnitude fluctuations of the total spins. The low transition temperature and Curie-Weiss law were explained by the transverse fluctuations.

1.2.3.10 Fluctuating local band theory (FLB)

Another approach [127] [128] [95] [96] [97] [152] [153] started from the mean field treatment of the Hubbard model, and modified it little by little in order to reconcile many experimental facts qualitatively.

The random phase approximation (RPA) was the initial step beyond the mean field theory, which allowed one to solve the excitation spectrum of Hubbard model. This improvement gave rise to spin-wave modes. However, RPA could not explain the Curie-Weiss law. Moriya [127] [128] then introduced a self-consistent-renormalization (SCR) method, which was able to explain Curie-Weiss law at high temperatures. Meanwhile, the local band theory was developed [95] [96] [97] [152] [153], which incorporates an idea similar to Moriya's. The formation of a local band inhibits the local spin fluctuations. Thus, spin order can persist over a range beyond the nearest neighbors, which makes it different from DLM model where the disorder can be on the nearest-neighbor scale. At temperatures higher than transition temperature, this local order will be retained due to the high energy scale of band width, but the long range spin order will be destroyed, and with it, the ferromagnetic states.

1.2.3.11 Density functional theory (DFT)

From Heisenberg model [69] to Fluctuating band theory [128], people try to simplify the complicated many-electron problem by various approximations in order to get an analytical solution. Meanwhile, numerical calculation methods were developed to achieve solution by taking less approximations. Density functional theory is among the most successful methods. As the computational power of the modern machines grows, the DFT is playing more and more important roles in physical and chemical research.

Diagonalizing the high-dimensional matrices is the insurmountable difficulty in solving many-electron problem for both analytical and numerical methods. It is necessary to reduce the dimensionality of the problem before one can get a solution. Normally, to do this definitely loses important information of the many-electron system, it turns out that if only the ground state is concerned, there exists a way to reduce the dimensionality without

approximations.

In 1927, Thomas and Fermi proposed independently a way (Thomas-Fermi model) [172] [57] to calculate the energy of an atom by representing its kinetic energy as a functional of the electron density, combining this with the classical expressions for the nuclear-electron and electron-electron interactions (which can both also be represented in terms of the electron density). The total energy is given as a functional of electron density $n(\overrightarrow{r})$:

$$E_{TF}[n] = \frac{3}{10}(3\pi^2)^{2/3}\int n^{5/3}(\overrightarrow{r})d\overrightarrow{r} - Ze\int \frac{n(\overrightarrow{r})}{\left|\overrightarrow{R}-\overrightarrow{r}\right|}d\overrightarrow{r} + \frac{1}{2}\int \frac{n(\overrightarrow{r_1})n(\overrightarrow{r_2})}{|\overrightarrow{r_1}-\overrightarrow{r_2}|}d\overrightarrow{r_1}d\overrightarrow{r_2}.$$

Thomas-Fermi model is the predecessor of the DFT, because the concept of density functional is already there. In 1964, the DFT was put on a firm theoretical foundation by Hohenberg-Kohn (HK) theorems [72]. The first HK theorem demonstrates the existence of a one-to-one mapping between the ground state electron density and the ground state wavefunction of a many-particle system. The second HK theorem proves that the ground state density minimizes the total electronic energy of the system. The theorems reduce the problem of solving ground state of a many-electron system from solving high-dimensional wavefunction to solving a much low-dimensional electron density without approximations. However, although the existence of the one-to-one mapping is proved, the exact mapping is not provided by the Hohenberg-Kohn theorems.

Since the exact one-to-one mapping is not known, one has to make approximations to guess the mappings in order to implement the DFT. Kohn-Sham (KS) method [92] provides a framework that is commonly used for the implementation. Within the framework of KS DFT, the intractable many-body problem of interacting electrons in a static external potential is reduced to a tractable problem of non-interacting electrons moving in an effective potential $v_{eff}(\overrightarrow{r})$:

$$-\frac{\hbar^2}{2m}\nabla^2\psi(\overrightarrow{r}) + v_{eff}(\overrightarrow{r})\psi(\overrightarrow{r}) = \varepsilon_i\psi(\overrightarrow{r}).$$

The effective potential includes the external potential $V_{ext}(\overrightarrow{r})$ and the effects of the Coulomb interactions between the electrons, e.g. and the exchange and correlation interactions :

$$v_{eff}(\overrightarrow{r}) = V_{ext}(\overrightarrow{r}) + \int \frac{n(\overrightarrow{r_1})}{|\overrightarrow{r}-\overrightarrow{r_1}|}d\overrightarrow{r_1} + \frac{\delta E_{xc}[n]}{\delta n},$$

where $\int \frac{n(\overrightarrow{r_1})}{|\overrightarrow{r}-\overrightarrow{r_1}|} d\overrightarrow{r_1}$ and $E_{xc}[n]$ represents classical Coulomb interaction and the exchange and correlation interactions respectively. The total energy is:

$$E = \sum \varepsilon_i - \int \frac{n(\overrightarrow{r_1})n(\overrightarrow{r_2})}{|\overrightarrow{r_1}-\overrightarrow{r_2}|} d\overrightarrow{r_1} d\overrightarrow{r_2} + E_{xc}[n] - \int \frac{\delta E_{xc}[n]}{\delta n(\overrightarrow{r})} n(\overrightarrow{r}) d\overrightarrow{r}$$

Unfortunately, the exchange and correlation interaction functional $E_{xc}[n]$ is unknown. To guess the functional is where most approximations come in. The simplest approximation is the local-density approximation (LDA) [92], which is based upon exchange energy for a uniform electron gas, which can be obtained from the Thomas-Fermi model, and from fits to the correlation energy for a uniform electron gas. Similarly, local-spin-density approximation (LSDA) [12] [137] [133] takes into account of the electron density with different spins. Furthermore, generalized gradient approximations (GGA) [101] [100] [143] [145] consider gradient of the density at the same coordinate as well the electron density.

Using the DFT, electronic structures of ferromagnetic materials have been studied. Based on the electronic structures, various properties such as cohesion energy, magnetic moment and Curie temperature have also been investigated numerically [53] [52] [51] [103] [110] [50] [125]. Because of the strong exchange and correlation interactions in ferromagnetic system, generally the DFT does not do as good job as it does in less correlated system. Using certain form of functional $E_{xc}[n]$, the calculations are in good agreement with the experiments. However, depending on the system studied, different functional $E_{xc}[n]$ has to be used. There is not yet a universal way that is able to calculate different materials and get good results with no fitting parameters.

1.2.3.12 Open questions

Note that the difference between the DLM and the FLB is very subtle. The most obvious difference is that local order is critical for FLB. Neutron scattering experiments showed some evidence for local order above the Curie temperature [122] [123] [124] [121] [28]. However, it has not been confirmed by any other experimental method. Another fact is that both theories remain at qualitative stage, due to mathematical complexity of the theory, which prohibits quantitative predictions.

A ferromagnetic system with a size that is comparable or even smaller than the scale of local order is very interesting. In this system, the existence of local order can be directly tested. More interesting are systems that are so small that their Hamiltonians can be diagonalized without too much approximation (e.g., a cluster with only two iron atoms) [157] [171] [174] [11] [184] [14]. If their magnetic properties are measured, all theoretical models can be tested by comparing them to the experiments.

Although the DFT is promising in studying ferromagnetism, the results of calculation have to be compared to experiments. Small cluster systems definitely can give another way to verify and refine DFT.

Hence, the questions are: what is going to happen in the small magnetic system, and how are all kinds of theoretical models going to predict the magnetic behavior of these small systems? The study of small magnetic clusters is the key to answering these questions.

CHAPTER II

INTRODUCTION TO CLUSTER PHYSICS

2.1 From atom to bulk

The physical properties of metals change dramatically with size. The bulk limit was the first to be studied. More precisely, the physics of the other limit (atom) was understood. Clearly, knowledge of atomic physics is essential to understand the bulk. It is even more interesting to study the intermediate range, which provides a new perspective in bulk properties. In fact the evolution from atom to bulk itself is an intriguing subject.

If the properties change gradually and continuously with size, the investigation of size dependence would not be of much interest. Nature has presented us with a different situation. The properties change not monotonically, but often in an interesting quasi-periodic way and sometimes erratically [113]. Clusters belong to the intermediate size range, therefore they have much more variety than the two limits. As a matter of fact, adding or subtracting one atom from a cluster changes their properties dramatically [2].

It is interesting to look at the cluster mass spectrum to get an idea of the cluster size evolution. The generic Hamiltonian can be broken up into two parts: the surface part and the interior part.

$$H = H_{interior} + H_{surface}. \tag{31}$$

By this counting, very small metal clusters are all surface and resemble molecules (that is why they are heavily studied by chemists). The metallic bond may not be fully developed for these clusters. Actually the metal to insulator transition was observed in this range [183]. Since every atom is on the surface, the shape varies significantly depending on the number of atoms in the cluster. The electronic energy spectra consists of a countable number of discrete levels. They can be written as a sequence of delta functions. For clusters beyond this size range, their properties are more complicated. I will start from the better-understood simple-metal clusters and try to expand to other metal clusters.

For slightly larger sizes, electronic shells form in simple metal clusters [41] [27] [112] [113] [114]. In these cases, a significant amount of electrons spill out beyond classical boundaries of the clusters. In first approximation a number of properties can be attributed to that. Since electrons spend most of their time on the surface of the cluster, the details of the ionic core are less significant. In fact, it appears that the shape of the ionic core is determined by the electronic shell structure. Generally, clusters deform into ellipsoids to be energetically efficient for electrons. This effect is called the Jahn-Teller effect [80] [79]. Consequently when electrons form a full shell, the clusters are spherical. A very simple model provides some basic insight into the structure of simple metal clusters. In this mode, the spherical shell structure can be understood using spherical a 3-dimensional harmonic oscillator [42]:

$$H_{eshell} = \hbar\omega(n_x + n_y + n_z + \frac{3}{2}), \tag{32}$$

where ω is frequency of the oscillator, n_x, n_y and n_z are the energy quanta. The energy levels will be discrete

$$E_n = \hbar\omega(n + \frac{3}{2}), \tag{33}$$

with degeneracy

$$D_n = \frac{n^2}{2} + \frac{3n}{2} + 1, \tag{34}$$

where

$$n \equiv n_x + n_y + n_z. \tag{35}$$

Notice that the degeneracy increases quadratically with energy. Introducing the deformation of the potential well, these energy shells are no longer degenerate. They disperse producing a band of levels. If the broadening is close to the energy separation between shells, the density of state increases with second power of the energy, approximately:

$$D(E) \propto E^2, \tag{36}$$

so that the energy spacing at the Fermi energy

$$\delta(E_F) = \frac{2E_F}{3N_e} \tag{37}$$

where E_F is the Fermi energy and N_e is the total number of conduction electrons. This is the extreme case: normally the broadening is much smaller and the energy spacing at the Fermi energy is much less [134] [135].

For even larger sizes, geometric shell structure will take over [113]. In this case, the surface plays a slightly different role. Clusters want to minimize the surface area in order to increase the coordination (i.e., minimize the surface energy), therefore, they tend to be spherical. The geometric structure of the clusters is not the same as that of the bulk however. Noncrystalline structures (e.g., icosahedra) often are preferred for smaller clusters in this range [114]. Ultimately for even larger sizes, the periodic structure of the bulk develops. Then the clusters look like fragments of the bulk material. Kubo [67] pointed out that they can be treated as highly disordered systems for which the energy levels are approximately uniformly spaced by

$$\delta \approx \frac{2E_F}{N_e}. \tag{38}$$

When the size increases even further, the bulk limit will be reached where the surface effect is ignorable unless the surface itself is studied. In that limit the quasi-free electron model [117] is appropriate for the conduction electrons. In this case, the density of states will increase with a power of $\frac{1}{2}$.

The behavior discussed above depends on the type of metal. For simple metals (e.g., alkali), the atoms' core levels are filled. The valence electrons are all from isotropic s electrons, and the clusters tend to form electronic shells. In fact, electronic shells are observed for sodium clusters with up to several thousand atoms [113]. For transition metals, the valence electrons are not only s electrons, but also d or f electrons that are directional. In those cases, it is seen that clusters tend to have geometrical shells [138]. The interplay between electronic shell and geometrical shell structure adds complications and causes of new phenomena for transition metal clusters that are not seen in simple metal clusters. These phenomena include superconductivity, ferroelectricity and ferromagnetism [98] [129] [60].

The physical properties do not change monotonically from atom to bulk. For example, properties have been observed to show enhancements or reductions compared with the bulk,

such as enhanced magnetic moments and polarizabilities [21] [41]. Novel features that only belong to clusters are also observed, such as shell structure and permanent electronic dipole moments for metal clusters [129].

The transition metal clusters studied in this thesis contain from a few atoms to a few hundred atoms. They fall into a size range where both electronic and geometric shells are expected.

2.2 Ferromagnetism of free clusters

As mentioned in Chapter 1, the study of small ferromagnetic system is important for understanding the fundamental problem of ferromagnetism. Since there are basic differences between the magnetism of atoms and that of the bulk, it is especially interesting to look at systems that consist of a few atoms to determine the evolution with size. The molecular beam method provides isolated clusters and is likely the most appropriate way to study intrinsic magnetic properties of clusters.

2.2.1 Does spin relaxation occur in isolated clusters?

In 1985, the pioneering experiment on clusters of ferromagnetic metals was performed on iron clusters [38]. In these experiments a beam of iron clusters was deflected in the fields of Stern-Gerlach magnet. Unfortunately, complete deflection beam profiles of these clusters were not measured, so that the most important difference was missed between the deflection of an iron atom and deflection of an iron cluster in a Stern-Gerlach magnet. The first measurements of the complete deflection profiles of iron clusters were done five years later [45], which showed the striking single sided deflection. For an isolated atom, we expect that the deflection corresponds to the projection of the magnetic moment along the direction of the magnetic field, hence $-g_{Lande}\mu_B J$, $-g_{Lande}\mu_B(J-1)...$, $g_{Lande}\mu_B(J-1)$, $g_{Lande}\mu_B J$, as shown in 1.2.1. In other words atoms are as likely to be attracted to a magnet as to be repelled, depending on their quantum states. However, the single sided deflections indicate that the iron clusters are uniquely attracted by the magnet, much like macroscopic iron. It was also observed that the magnetization measured from the deflections is smaller than that of the bulk. And it increases with an increasing magnetic field [45].

All of these effects were unexpected and needed to be understood in order to extract the magnetic moments of clusters. Actually, a similar behavior was already seen for small magnetic particles on a substrate, an effect called superparamagnetism [15]. It was found that the magnetization of small magnetic particles does not have hysteresis above a certain temperature (blocking temperature T_{block}).

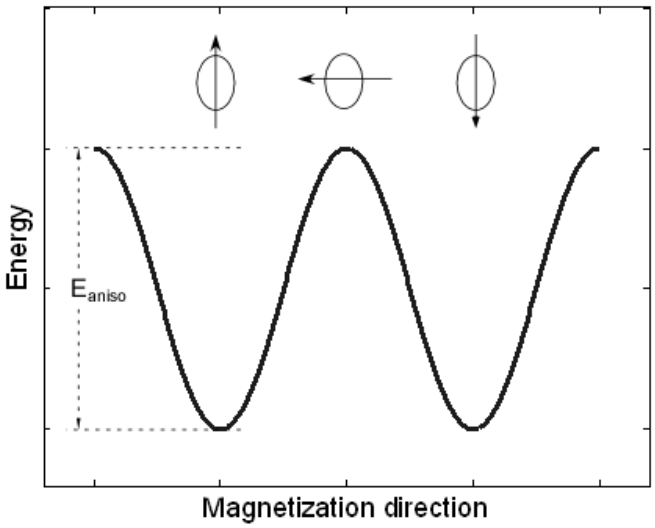

Figure 1: Schematic illustration of anisotropy energy of a magnetic particle. When the magnetization is aligned to the "easy" axis, the energy reaches a minimum.

Superparamagnetism was explained by Neel [132] and by Brown [29] in terms of a competition between the magnetic anisotropy energy (E_{aniso}) and the thermal energy. It was argued that if the magnetic anisotropy energy is much larger than the thermal energy (k_BT), then the orientation of the magnetic moment should be pinned along the easy axis. When the thermal energy is high enough, the magnetic moment will fluctuate quickly between the two minima in Figure 1, causing the loss of hysteresis behavior. The fluctuation rate is governed by the Arrhenius relation, proportional to e^{-E_{aniso}/k_BT}. Because the anisotropy energy is proportional to size of the particle, for small particles the blocking temperature is low. The relation between the magnetization M (the average projection of the magnetic moment on a certain space axis) and total magnetic moment μ for superparamagnetic

particles is given by the Langevin function:

$$M = \mu(\coth(x) - \frac{1}{x}), \tag{39}$$

where $x \equiv \frac{\mu B}{k_B T}$. At low field limit,

$$M = \frac{\mu^2 B}{3k_B T}. \tag{40}$$

At high field limit,

$$M(x \gg 1) = M_{Saturate} = \mu, \tag{41}$$

where $M_{Saturate}$ is the saturation magnetization.

Since free clusters appeared to mimic this behavior, the idea of superparamagnetism was adopted from supported clusters and applied to free clusters using exactly the same spin relaxation (SR) model [86]. Since experiments [30] [45] showed that magnetization is indeed proportional to the magnetic field and inversely proportional to the temperature, as (40) predicted, (40) was accepted as an empirical relation.

However, there are two problems with the SR model of (40) that should be considered.

The first one comes from the experimental side. Although the proportionality between M, B and $1/T$ are confirmed, the coefficient $\frac{\mu^2}{3k_B}$ is actually only a hypothesis that was not confirmed. Also according to the SR model, (40) is only the low field limit. What should be verified is (39). Therefore, as far as experiments are concerned, we should investigate all the conditions from $x \ll 1$ to $x \gg 1$. If (39) is right, in order to verify (40) with no doubt, we should get the magnetic moment from the saturation magnetization $M_{Saturate}$. Some work toward this direction [148] [149] has been done on dysprosium (Dy), however more thorough studies are required.

The second problem arises from the statistical thermodynamics for free clusters. In the argument for supported particles, the temperature T is a well defined physical quantity that is the same as that of the heat bath provided by the substrate. However, for free clusters, there is clearly no heat bath because the clusters are isolated. In fact, the only candidates for the heat bath are the vibrations of the cluster itself. However, if we keep to that idea, we have to surmount two other difficulties. One is discussed in Appendix B: for small clusters, the lowest vibrational mode has energy on the order of $k_B T_{Debye}$, where T_{Debye} is the Debye

temperature. Consequently, for example, if a cluster of 10 cobalt atoms is generated in a source of 77 K, the average number of phonons in the cluster is less than one. This state cannot serve as a heat bath. The other difficulty is more subtle: even if there are many phonon modes excited, angular momentum has to be conserved when spins are flipped, but vibrations do not carry angular momentum. It is interesting to investigate the process theoretically taking into account of all the issues just mentioned. Much attention has been devoted to this issue [116] [20] [19] [182] [68] [82] [83] [10] [118] [108] [90], but there is still no consensus.

Clearly, there are good reasons for the magnetization of clusters of ferromagnetic metals to be investigated more carefully, both experimentally and theoretically.

2.2.2 Magnetic moment

2.2.2.1 Experiment

The magnetic properties of various metal cluster systems [21] [25] [35] [36] [89] [91] [70] [130] [194] [196] have been analyzed in terms of the relation (40). The results are less surprising compared to the magnetization behavior. Below, we have summarize the previous work on the ferromagnetism of metal clusters.

For clusters of ferromagnetic metals, it is found that the magnetic moment per atom is enhanced for small clusters and decreases with increasing size until they converge to the bulk value [21] [9]. The decrease of magnetic moment per atom with size is not monotonic. Like other properties of clusters, it oscillates. The oscillations were attributed to the geometric shell structure of the clusters [2] [21] [22]. Some clusters of antiferromagnetic metals (Mn, e.g.) were found to be ferromagnetic [89], as were some clusters of nonmagnetic metals (Rh, e.g.) [37] [36].

2.2.2.2 Theory

The enhancement of magnetic moments in small clusters is generally explained as a surface effect. To explain more detail, calculation needs to know geometric structure of the clusters, which is a problem that has not yet a good solution. There are some indirect means to get some clue about the structure of clusters, including chemical reaction, photoelectron

spectroscopy, and electron scattering [105] [106] [107] [197] [66] [138]. Generally, detail of the geometric structure of a clusters is unknown. Nevertheless, assuming a structure, one can carry out calculation of a cluster's electronic structure and therefore magnetic moment.

Because of the limitation of computational power of the hardware, early electronic structure calculations are mostly based on tight-binding Hubbard Hamiltonian using Hartree-Fock approximation. Pastor et al. [140] found the enhanced magnetic moments for small iron and nickel clusters. Similar results were found later on by Andriotis et al. [8] for cluster size containing more than 100 atoms. Lopez et al. [156] studied the geometry of cobalt clusters and found an icosahedral growth pattern for the global minimum with some hcp and fcc structure for particular sizes. The magnetic moments also agree with the experiments better.

The DFT calculation are mostly restricted to small clusters due to the much computational effort needed. First wave of studies focus on the geometry and magnetic moments of very small clusters that can be investigated by the DFT [102] [155] [56] [32] [146] . Since the DFT can give a more precise and reliable total energy of a cluster with certain geometry, it is used to explain the tendency of icosahedral geometry of small cobalt clusters [102]. Some magic numbers are found for small clusters. Many isomers with different energy and magnetic moments are found for small clusters too [155] [56]. Unfortunately, experimental value of magnetic moment of very small clusters ($N < 5$) that are more feasible for calculation are not available yet. Calculations on iron clusters show the enhanced orbital magnetic moments as well as the total magnetic moments [151] [164]. Recently, Tiago et al. [173] claimed that the DFT calculation has been done on iron clusters for size up to $N = 400$ and the overall reduction of the magnetic moment from atom to bulk is reproduced.

2.3 Other properties related to electronic structure of clusters

2.3.1 Static dipole polarizability

On the macroscopic scale, the dielectric constant ϵ is often used to describe the response of a material to an external electric field [78]. For vacuum $\epsilon = 1$, and for metal $\epsilon \to \infty$, which

means that vacuum cannot be polarized by an external field and for metals it is very easy. Another way to describe this is to use the screening length λ_{screen}. Normally, for a metal, the screening length is on the order of 0.1 $\mathring{A}$ [202], which means that the external electric field is almost perfectly screened down to the sub angstrom scale.

For a microscopic system, especially when we are considering a cluster with a radius of 1 nm, the polarizability α is a better way to describe the response to an external field. Normally for a solid, α can result from a polar or a nonpolar state. In a polar molecule, α reflects the degree of alignment with the field. The nonpolar α is caused by the redistribution of the electronic charge. Since metal clusters are studied here, normally we are only concerned with non-polar α. In fact, as mentioned above, a permanent dipole moment has been found for some metal clusters [129], but in that case a whole different analysis has to be carried out for the polar contribution. Nonetheless, for the clusters we are studying in this thesis, we have not seen any sign of polar contributions. That means, the clusters do not have permanent electronic dipole moments. The connection between the atomic polarizability α_{atom} and dielectric constant is given by the Clausius-Mossotti relation [78] as

$$\alpha_{atom} = 3\Omega_{atom}\frac{\epsilon - 1}{\epsilon + 2}, \tag{42}$$

or

$$\epsilon = 1 + \frac{\frac{\alpha_{atom}}{\Omega_{atom}}}{1 - \frac{\alpha_{atom}}{3\Omega_{atom}}},$$

where Ω_{atom} is the atomic volume.

The response to a static electric field changes with the size of the system, and with other properties. Since even for a metal the screening length is not zero, the screening ability will be reduced when the size is small. This is reflected in the reduced dielectric constant. Another effect is shown by the following classical equation:

$$\alpha = 4\pi(R + \delta_{spillout})^3,$$

where R is the classical radius of the spherical system, and $\delta_{spillout}$ is called electronic spillout. Because $\delta_{spillout}$ is on the order of an angstrom, this effect is very important for

small clusters.

Polarizability is one of the most straightforward properties that can be measured by the electric deflection technique [41]. Since it provides information about the electronic structure (e.g. the volume) of the electron cloud, it gives us a very powerful tool for studying small clusters. In particular, the spillout is quite sensitive to the density of selected electrons, so that the polarizability is, in a sense, a probe of state and density.

2.3.2 Photo-ionization efficiency

To probe the electronic structure of clusters, photo-ionization experiments are often performed. In these experiments, clusters are illuminated by single-wavelength photons. The ionization efficiency is measured as a function of the wavelength of the photons. The threshold of the photo-ionization, called the ionization potential (IP), is then determined from the ionization efficiency.

For various reasons (e.g., finite temperature, line width of the ionizing photon) [160] [147] [73] the threshold of the photo-ionization is not sharp, which makes the analysis complicated. There is another complication caused by the structure change due to ionization. When a cluster loses one electron, the structure of an ionized cluster may not be the same as that of the neutral cluster. The energy difference between the ground state of neutral cluster and that of the ion is called adiabatic ionization potential (AIP). However, because the ionization happens much faster than the structure change, the most probable electron transitions are those in which the structure does not change. This is called Franck-Condon principle [17] and the corresponding ionization potential measured is called the vertical ionization potential (VIP), which is slightly different from AIP.

Although there is no unambiguous way to extract the threshold from ionization efficiency data [65] [185] [84] [104] [16], as long as all clusters are analyzed consistently, the comparisons between clusters should be valid.

The ionization potential predicted by the Jellium model (defined by a Hamiltonian that treats the electrons as usual but the ionic cores as a uniform positively charged background)

[27] is

$$IP = IP_0 + \frac{\alpha_{IP}}{4\pi\epsilon_0}\frac{e^2}{R + \delta_{spillout}},$$

where IP_0 is the ionization potential when R is infinity, α_{IP} is the fitting constant. For classical sphere $\alpha_{IP} = \frac{1}{2}$ [109] [144]; for cluster it is normally very close to $\frac{1}{2}$ [27] [144].

CHAPTER III

EXPERIMENTAL SETUP

3.1 Molecular beam machine

Clusters have been studied with various techniques. The earliest methods measure properties of clusters on substrates [94] [15] [62] [131] [191]. However, the interaction of the substrate with the clusters is distracting because it is a source of controversy concerning the interpretation of the measurements and is poorly understood. Alternatively, free clusters in the gas phase have the advantage of being isolated from the environment and other clusters, so the intrinsic properties of clusters can be investigated.

Even though technical difficulties limited the styles of clusters that could be studied, these early studies produced important results.

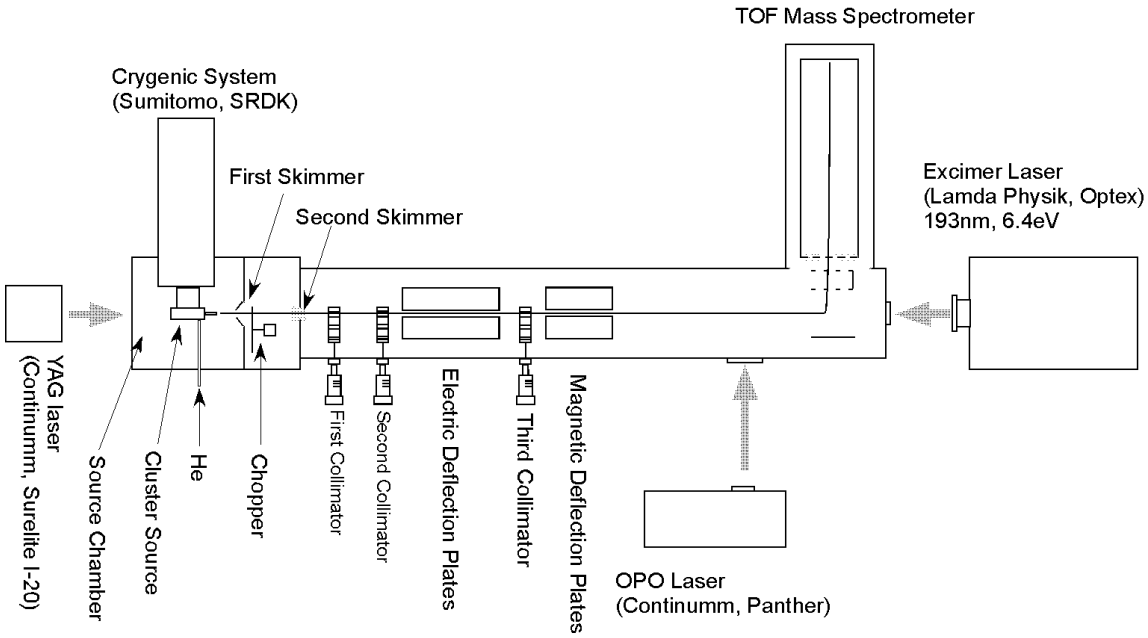

Figure 2: Schematic illustration of the experimental setup showing the main parts of the molecular beam apparatus. The scale of the machine is about 2.5 m, excluding the lasers.

Molecular beam methods used in this thesis allow clusters to be studied in the gas phase.

Gaseous clusters are created and measured by the molecular beam method. The main components of the apparatus are shown in Figure 2. The operation of the experiment is briefly described next and in more detail in the subsequent sections. Focused laser light from a YAG laser hits the metal sample rod. This generates a metal vapor in the source chamber. A short pulse of precooled helium (He) gas is injected into the source. The metal vapor cools down and condenses into clusters. Helium gas carries the clusters through a nozzle to form a cluster beam. The cluster beam is skimmed by the first skimmer (1.0 mm diameter) that separates the first and the second chamber. The cluster beam is collimated by a second skimmer (1 mm wide, 2 mm high) and three collimators (collimation 0.1 mm $\times$5 mm, 0.3 mm $\times$5 mm or 0.8 mm $\times$5 mm). The cluster beam then may be deflected in either magnetic or electric fields depending on which property is under investigation. Finally, the clusters are photo-ionized by an Excimer laser (193 nm) or an OPO laser (215 nm$-$700 nm). The mass and the position of the clusters are simultaneously measured using a time-of-flight (TOF) position-sensitive mass spectrometer [43]. The repetition rate of the experiment is 20 Hz. If deflection experiments are performed, the field is switched on and off every 20 seconds, and the data are stored in separated channels to produce an off spectrum and an on spectrum. Data are collected by the computer for several hundred cycles for a single experiment to average out cluster beam intensity fluctuations.

Table 1: Pressures and the mean free path for the chambers. The cluster collision cross section is taken to be 1 $(\text{nm})^2$.

Chamber	1st	2nd	3rd	4th
Pressure (Torr)	10^{-2}	5×10^{-6}	10^{-7}	10^{-9}
Mean Free Path (m)	10^{-3}	2	10^{2}	10^{4}

The apparatus is differentially pumped. Pressures and the mean free paths are summarized in Table 1. The first and second chambers are connected via the first skimmer. The second and third chambers are connected via the second skimmer. The third chamber includes the deflection plates and the fourth chamber houses the time of flight spectrometer. The first chamber has the highest pressure because hehium gas is injected into this

chamber. Note that downstream from the first skimmer, the clusters are collision free.

3.2 Laser ablation source

The laser ablation cluster source is a critical part of the apparatus. This source is uniquely designed to produce cryogenic beams.

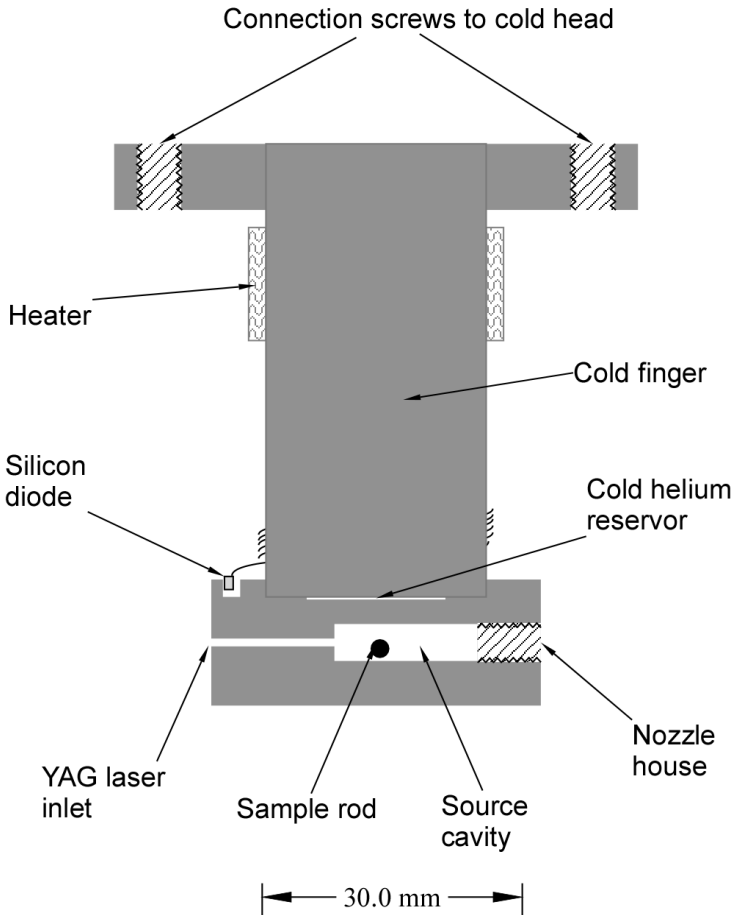

Figure 3: Cross section of the laser ablation source with the cold finger, the heater and the thermal diode. The nozzle and the pulsed valve are not shown.

Figure 3 shows the cross section of the source. The source is firmly connected to the cold head of the cryogenic system (Sumitomo, SDK) by 6 screws. A heater is attached to the cold finger close to the cold head. The temperature is measured using a diode (LakeShore 470 SD) that is located in the source and thermally connected using vacuum grease. The connection wires are wound around the cold finger to avoid heating by the wire. The resistance of the diode is measured by the temperature controller (LakeShore 321) that

converts this into a temperature. The controller supplies feedback to the heater so that the temperature is stabilized at the set temperature.

Focused YAG laser light enters the source via a 0.9 mm diameter hole as shown in Figure 3. This light hits the sample rod (2 mm diameter). A short pulse (with duration about 1000 μs at room temperature and 500 μs at 20 K) of precooled hehium gas enters the source cavity (0.5 cm^3 volume). Since the pressure in the source (on the order of 1 Torr) is much higher than the in the source chamber (10^{-2} Torr), the hehium gas and metal vapor mixture will pass around the sample rod and enter the nozzle region and ultimately escape from the nozzle.

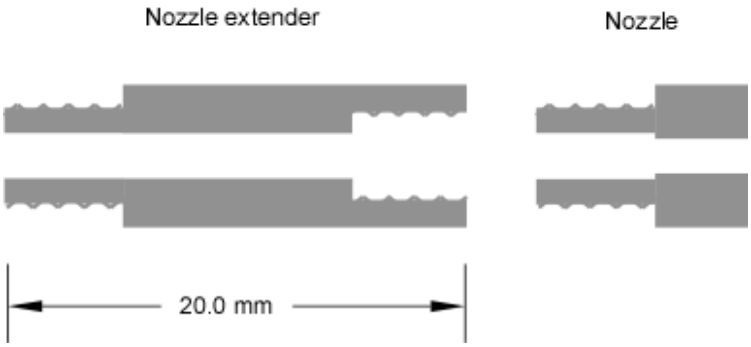

Figure 4: Cross section of the nozzle and the extender.

3.2.1 Nozzle

The nozzle and nozzle extender are shown in Figure 4. As shown in Figure 3, the nozzle tube diameter (about 2 mm) is much smaller than that of source cavity ($\sim$ 4 mm). This gives the mixture enough time to reach equilibrium. At the exit of the nozzle, the diameter is further reduced ($\sim$ 1.5 mm).

Clusters and metal atoms collide to make the clusters grow. Collision between hehium atoms and metal clusters carry away the heat of condensation. Therefore, a large enough number of collisions are critical for generating clusters as well as cooling the clusters generated. The number of collisions is sensitive to the source parameters.

In the experiments, three nozzles were used: one without a nozzle extender, one with a 1 cm extender and one with a 2 cm extender. A long nozzle helps obtain equilibrium. In

order to study excited states of clusters, short nozzles are used.

3.2.2 Reservoir

As mentioned above, the hehium gas is precooled in the reservoir between the source and the cold finger before it enters the source cavity (Figure 3).

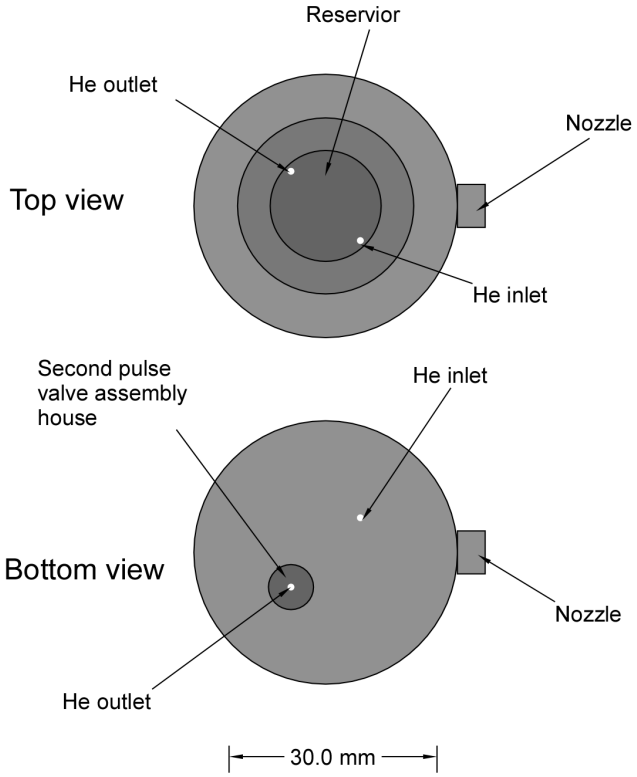

Figure 5: The top view and bottom view of the source without the cold finger.

Figure 5 shows a top view of the source with the cold finger removed. There are two pinholes (1 mm in diameter) in the reservoir. The first pinhole allows gas to enter the reservoir from the first pulsed valve, so that room temperature helium gas enters the reservoir. The second pinhole is sealed by the poppet of the second pulse valve. The helium gas stays in the reservoir for at least 40 ms before the second valve is opened. Hence, the helium gas can be cooled down from room temperature to the source temperature.

3.2.3 Second pulse valve

The second pulse valve is the most sensitive part of the source assembly because it has to operate at various temperatures.

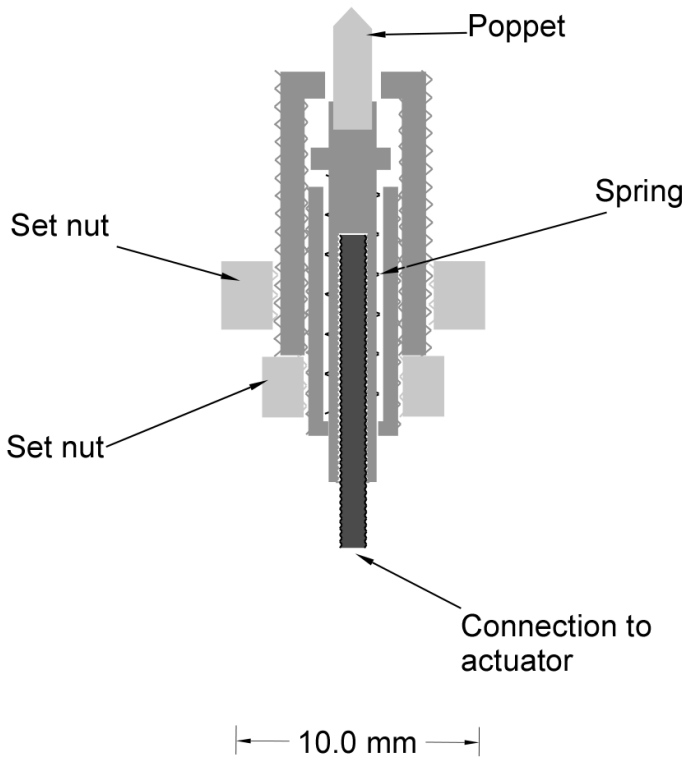

Figure 6: Cross section of the second pulse valve.

Figure 6 shows the cross section of the second pulse valve. The assembly is screwed in the source at the position shown in Figure 5. The poppet seals the pinhole of the hehium outlet by means of a spring. When an electric pulse is sent to the actuator (not shown here), the poppet will be pulled down, thereby opening the valves so that the cold gas will exit the reservoir and enter the source cavity. The spring restores the poppet position after the pulse and seals the reservoir. The poppet is made of Delrin whose thermal expansion is small.

As discussed in the Appendix B, the gas discharge into the source cavity can be tuned by the timing of the second pulse valve and by the length of the nozzle. Long nozzles and long pulse durations are required in order to attain equilibrium.

3.3 Deflection in Stern-Gerlach fields

3.3.1 Magnetic deflection

We use Stern-Gerlach inhomogeneous fields that are generated by pairs of deflection plates, to investigate the response of clusters to electric and magnetic fields.

Neutral clusters are deflected in an inhomogeneous field due to their magnetization. If a particle in an inhomogeneous field B in the z direction with energy U, then the magnetization in the z direction is

$$M \equiv -\frac{\partial U}{\partial B}. \tag{43}$$

The force in the z direction on the cluster is

$$F_z = -\frac{\partial U}{\partial z} = -\frac{\partial U}{\partial B}\frac{dB}{dz}, \tag{44}$$

where $\frac{dB}{dz}$ is the gradient of the field.

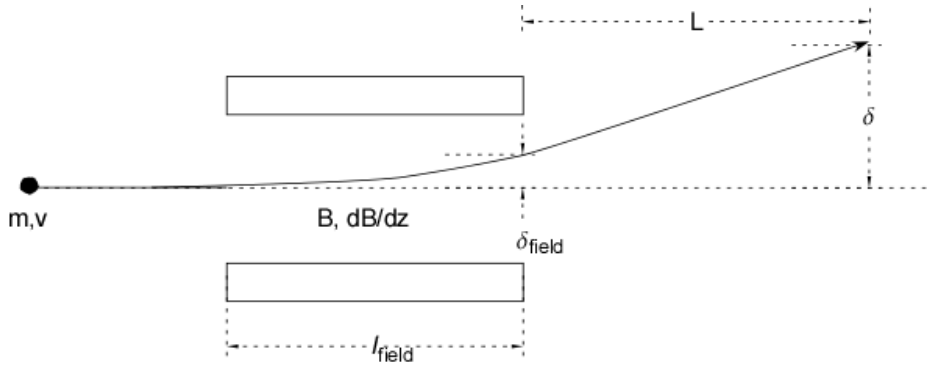

Figure 7: Schematic diagram of the deflection of a cluster in a Stern-Gerlach field. The magnetization is $M \equiv \frac{2}{l_{field}^2+2l_{field}L}\frac{\delta m v^2}{\frac{dB}{dz}}$.

The deflection δ_{field} in a field of length l_{field} is

$$\delta_{field} = \frac{1}{2}\frac{F_z}{m}(\frac{l_{field}}{v})^2, \tag{45}$$

where m is the mass of the cluster, v is the speed of the cluster, as shown in Figure 7. Combining (43), (44) and (45), we find the relation

$$M = \frac{2}{l_{field}^2}\frac{\delta_{field} m v^2}{\frac{dB}{dz}}. \tag{46}$$

The deflection of the detection

$$\delta = \frac{\delta_{field}}{l_{field}}(2L + l_{field}).$$

Therefore

$$M \equiv K\frac{\delta m v^2}{\frac{dB}{dz}}, \tag{47}$$

where $K \equiv \frac{2}{l_{field}^2 + 2 l_{field} L}$.

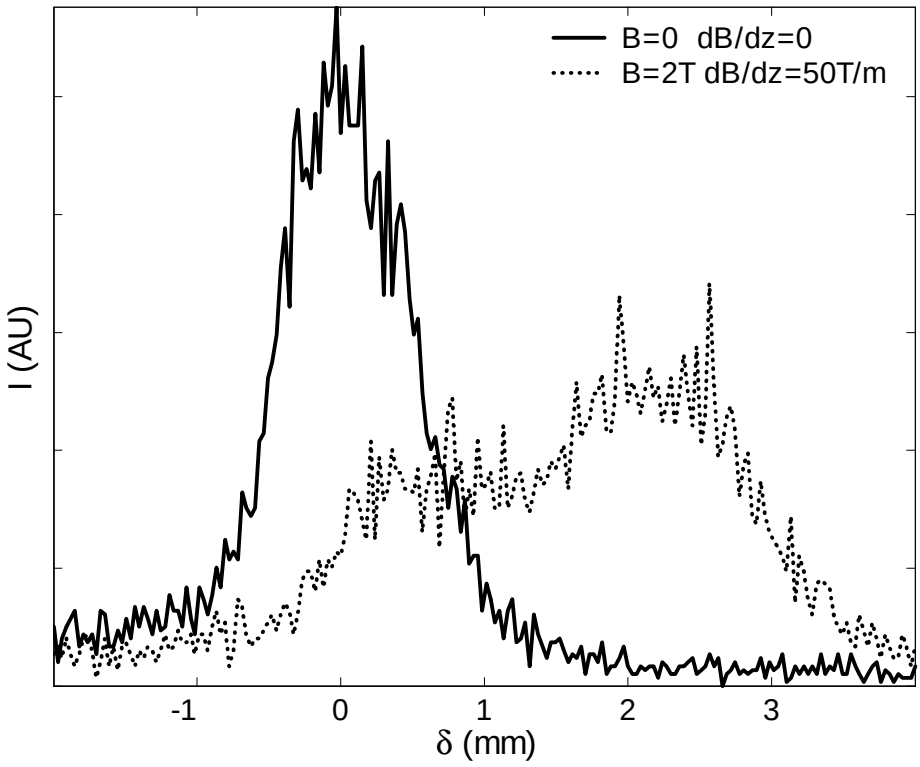

Figure 8: Typical beam profile with the magnetic field on and off. The Cluster is Co_{37}, T=30 K.

3.3.1.1 Beam profiles

The cluster deflection process is rather complex. This can be seen by noting that not all clusters deflect by the same amount. That is to say, the beam does not simply shift, but it can also broaden, when the clusters are subjected to the field of the Stern-Gerlach magnet. Hence, the beam profile changes from $I^{off}(\delta)$ to $I^{on}(\delta)$ (i.e. the intensity I as a function of deflection δ), when the field is turned on. This can be understood in terms of the

magnetization distribution $P(M)$ of the cluster beam. If the clusters have a magnetization distribution $P(M)$, then the beam profile with the magnetic field on $I^{on}(\delta)$ will be

$$I^{on}(\delta) = I^{off}(\delta) \otimes P(\delta),$$

where $P(\delta)$ is the deflection distribution, which is derived from the magnetization distribution $P(M)$. The magnetization distribution is known for some simple cases. For an atom, $P(M) = \sum_{J_z=-J}^{J} \delta(M - g_{Lande} J_z \mu_B)$, where $\delta(x)$ is the Dirac delta function, J is the total angular moment of the atom and μ_B is the Bohr magneton. For a cluster with susceptibility χ, $P(M) = \delta(M - \chi B)$.

However, the real beam profile is more complicated. Figure 8 shows an example of the beam profile for Co_{37} with and without magnetic field. As we can see, the beam profile with magnetic field can neither be explained by the atomic model nor in terms of susceptibility.

3.3.2 Electric deflections

3.3.2.1 Beam profiles

Electric deflections are less complex than magnetic deflections because for most clusters only have induced electric dipole moments [26] [44] [120] [88]. Therefore

$$\mu_{measure} = \alpha E,$$

where α is the polarizability and E is the electric field. Hence

$$\alpha = \frac{\delta m v^2}{KE(dE/dz)}, \tag{48}$$

where dE/dz is the gradient of the electric field along the z direction. In this case, the deflected beam profile will simply show a rigid shift at $\mu_{measure} = \alpha E$.

3.3.3 Stern-Gerlach fields

3.3.3.1 Two-wire field

The magnetic field geometry approximates that produced by two wires. This two-wire field geometry is optimal for molecular beam deflection and was first introduced by Rabi [141] [154]. Hence the pole faces are shaped to produce the two-wire fields as shown in Figure 9.

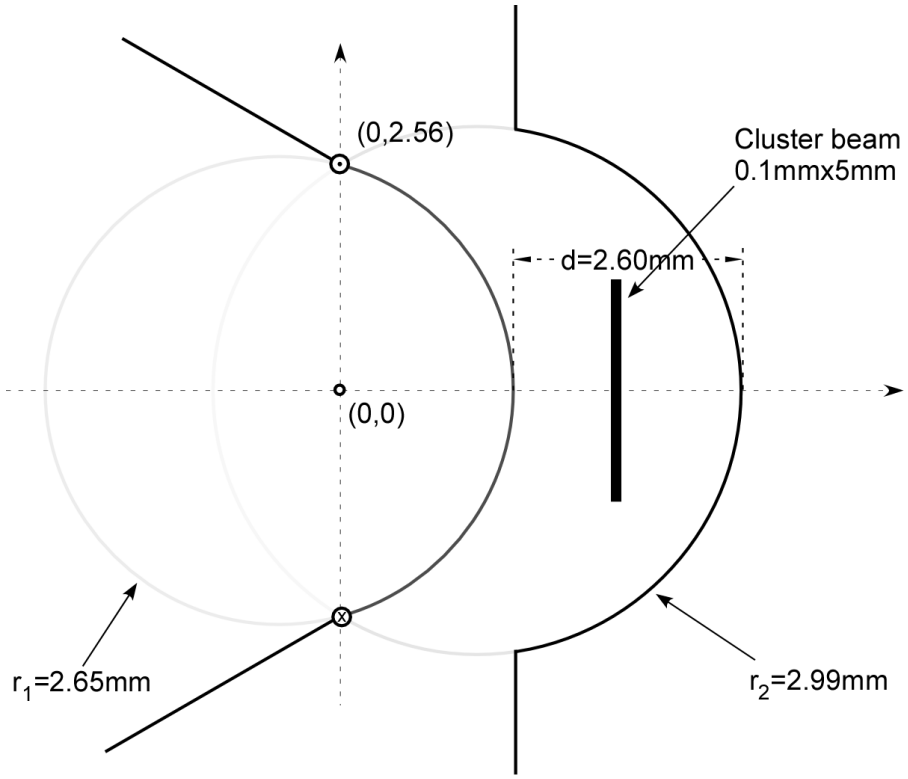

Figure 9: Pole face of the high deflection power magnet shown as an example of the two-wire field. The solid line is the shape of the pole faces, and the ribbon between the pole faces is at the position of the cluster beam.

If there were two wires perpendicular to the surface at position $(0, a)$ and $(0, -a)$, where a =2.56 mm, and one carries current inward and the other carries current outward, then the equipotential surface will be a set of circles [154]. Rather than using two wires, we construct two pole faces that correspond to two of the equipotential surfaces. This results in a field with the same structure. To describe the two-wire field, we need three parameters: the radii of the two arcs r_1, r_2 and the gap d between the two pole faces. We can find out the locations of the virtual wires using relation:

$$2r_2 - d = \sqrt{r_1^2 - a^2} + \sqrt{r_2^2 - a^2},$$

so that the shape of the inhomogeneous field can be calculated.

The ratio between field and field gradient is always fixed for a given magnet. Therefore, we construct several magnets in order to vary the gradient and the field strength separately. Figure 10 shows an example of pole face of low field gradient magnet. The dependence of

magnetic field on the current in the coil and magnetic field is determined by the material of the magnet.

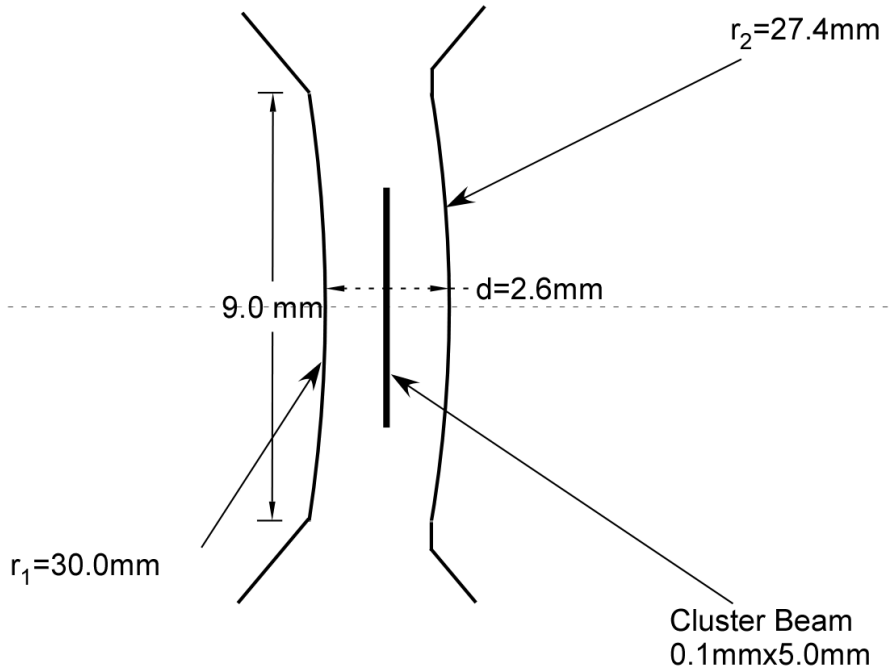

Figure 10: Pole face of the low deflection power magnet shown as an example of the two wire field. The solid line is the shape of the pole faces, and the ribbon between the pole faces gives the position of the cluster beam.

Table 2: Parameters of deferent magnets. The B_{max} and $(\frac{dB}{dz})_{max}$ are the values when the electric current in the coil is $7A$.

magnet	B_{max}(T)	$(\frac{dB}{dz})_{\max}$(T/m)	$length$(cm)	r_1(mm)	r_2(mm)	d(mm)
#1	0.91	345	12.5	2.65	2.99	2.6
#2	1.29	51.3	12.5	30.0	27.4	2.6
#3	1.09	34.5	4.0	30.0	27.4	2.6
#4	1.98	50.0	6.0	30.0	27.4	2.6

The four magnets shown in Table 2 have been used in this thesis. Calculation of the field and field gradient can be found in Ref [154]. The calibration of the magnet is performed as follows: the magnetic field is measured for various currents in the coils using a Tesla meter. The gradient of the field is calculated using (47) from the deflection of a beam of Al atoms. The magnetization distribution for the Al atom beam is $P(M) = \delta(M-\frac{1}{3}\mu_B)+\delta(M+\frac{1}{3}\mu_B)$

(The magnetic moment for Al atom is $\frac{1}{3}\mu_B$ and the angular momentum is $J = \frac{1}{2}$).

3.3.3.2 Coaxial field

In this thesis we also used a coaxial field, or a one-wire field. The equipotential surfaces of a charged wire with infinite length are a set of coaxial cylinders. We make two coaxial equipotential surfaces by two electrodes with certain voltages.

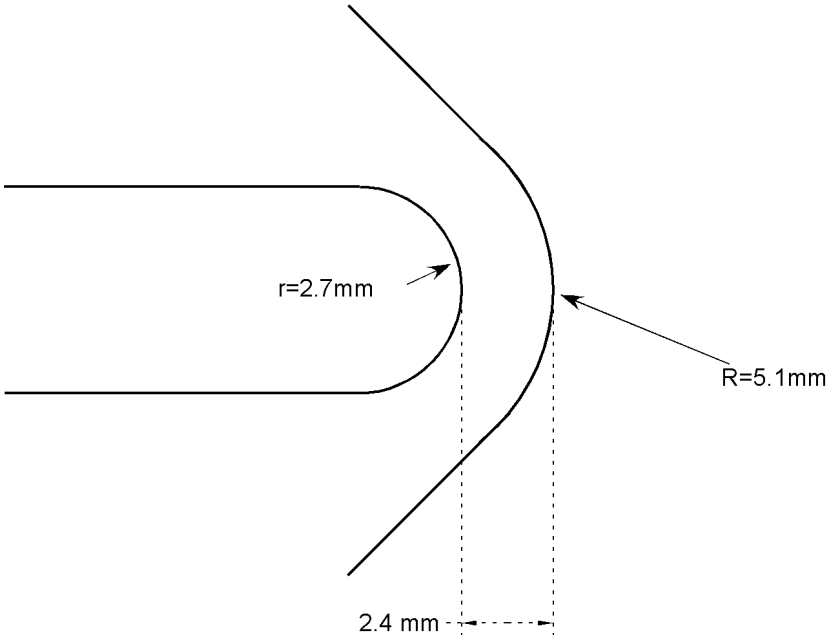

Figure 11: Pole face of the electric deflection plates.

Figure 11 shows the geometry of the coaxial electric deflection plates. It is trivial to calculate the electric field and field gradient for the coaxial field. The two coincident axes of the two cylinders are at the origin. The electric field and the field gradient are then

$$\begin{aligned} V(r_0) &= V_0 + \frac{\Delta V}{(\frac{1}{r} - \frac{1}{R})r_0}, \\ E(r_0) &= -\frac{\Delta V}{(\frac{1}{r} - \frac{1}{R})r_0^2}, and \\ \frac{dE(r_0)}{dr_0} &= 2\frac{\Delta V}{(\frac{1}{r} - \frac{1}{R})r_0^3}, \end{aligned}$$

where V_0 is a constant, and ΔV is the voltage difference between the two plates, r and R are the radii of two cylinders and r_0 is the distance from the origin. If $\Delta V = 20$ kV for example, then at the center of the deflection plates, $E(r_0) = 7.5 \times 10^6$ V/m, where $r_0 = (r + R)/2$.

3.4 Photo-ionization experiment setup

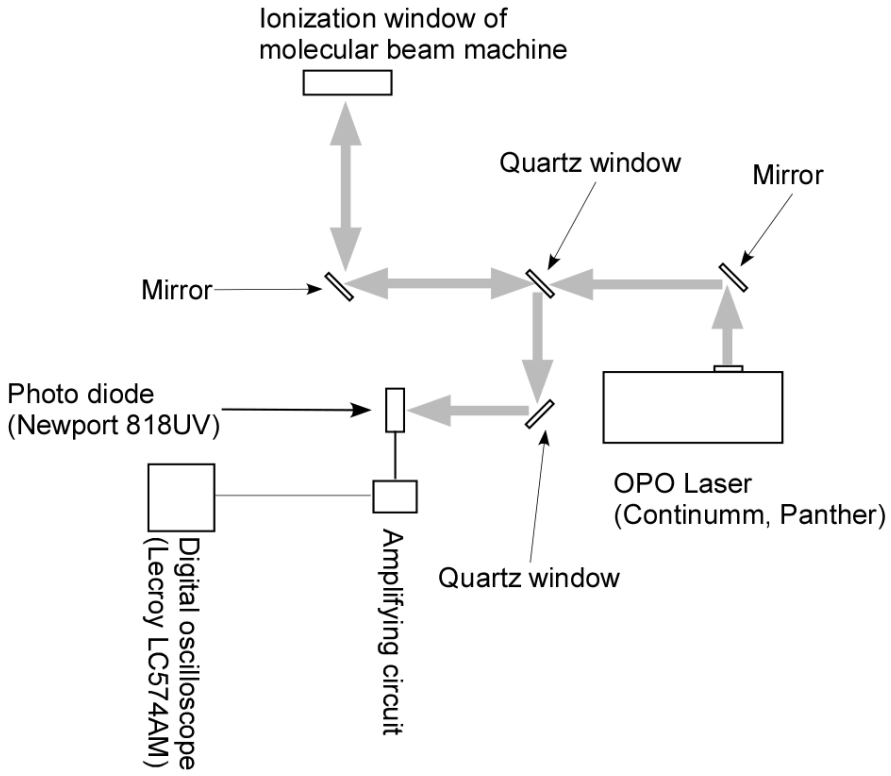

Figure 12: Experimental setup for photo-ionization potential experiments.

Usually photo-ionization is accomplished with fixed wavelength light supplied by an Excimer. For a photo-ionization experiment, the Excimer is replaced by an optical parametric oscillator (OPO) laser system (Continumm Panther) so that the wavelength can be continuously varied.

Figure 12 shows the setup for photo-ionization experiments. Since the intensity of the OPO laser changes with its wavelength, the laser intensity is monitored in real time in order to make a precise cluster ionization efficiency measurement. The OPO laser is sampled by its reflection from the ionization window into the molecular beam machine and further attenuated by reflections from the two quartz windows. The photo diode generates an electric current proportional to the intensity of the OPO laser, which is then recorded by the computer and correlated with the detected ion intensities to produce the photo-ionization efficiencies.

CHAPTER IV

MAGNETIZATION–RESULTS AND DISCUSSION

4.1 Experiment

In order to investigate the magnetization behavior of ferromagnetic clusters in a Stern-Gerlach field, we studied cobalt clusters for a wide range of sizes ($10 \leq N \leq 200$), temperatures ($25 \leq T \leq 100$) and magnetic fields ($0 \leq B \leq 2$ T).

4.1.1 Beam profiles

Figure 13a shows an example of beam profiles for Co_{20} at $T = 40$ K and $B = 2$ T. Two important features should be pointed out: (i) the clusters deflect exclusively in the stronger field direction; (ii) the beam profile is significantly broadened when the field is on indicating a wide magnetization distribution.

The magnetization distribution $P(M)$ is extracted from the beam profiles with magnetic field off and magnetic field on by the deconvolution method described in Appendix C (Figure 13b). The conversion from deflection to magnetization is done using (47). The intensity at negative magnetization in Figure 13b is an artifact of the deconvolution method due to statistical uncertainties. This does not affect the average magnetization. The magnetization distributions of all clusters are plotted together to give a global view in Figure 13c. Note that the average magnetization per atom saturates at 2 μB for large cluster sizes.

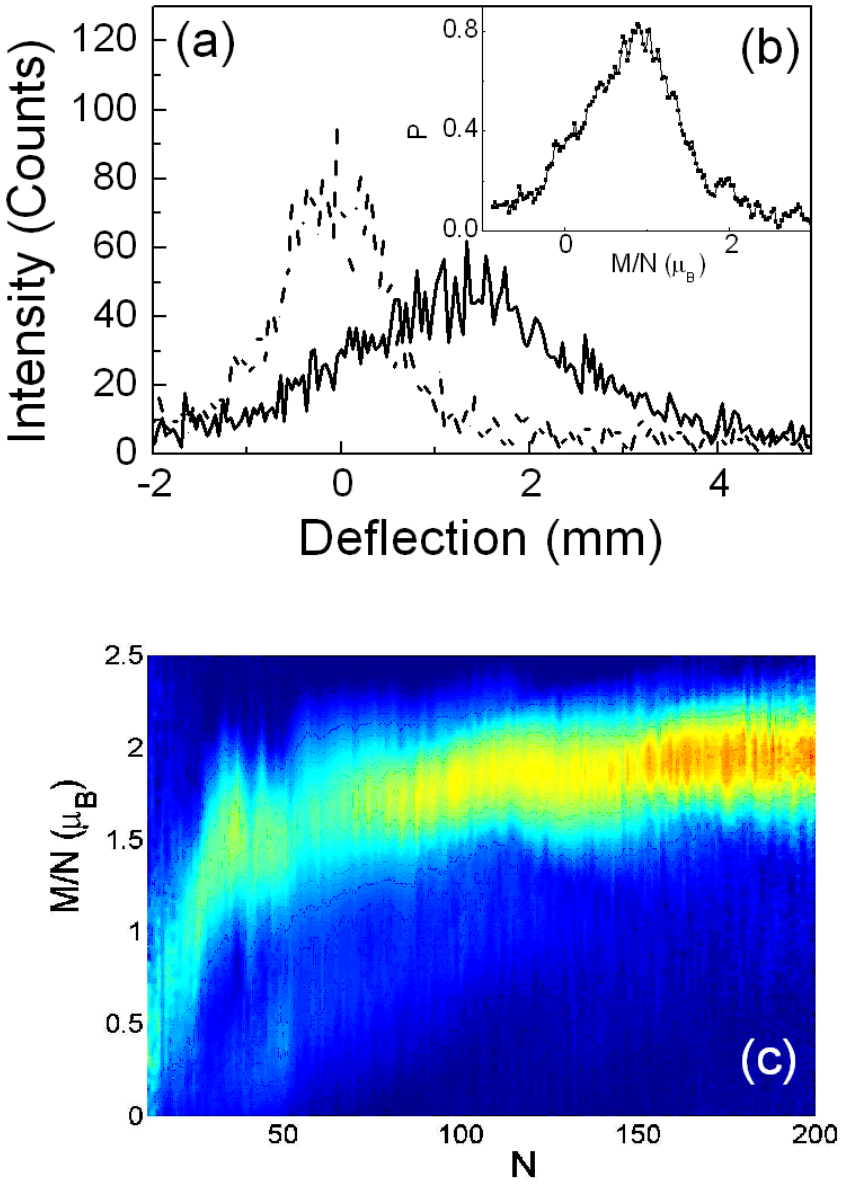

Figure 13: Deflections and magnetization distributions of Co_N at $T = 40$ K and $B = 2$ T. (a) Position sensitive mass peak of Co_{20} showing the field off (dashes) and the field on ($B = 2$ T, solid) deflections (the entire spectrum is composed of about 200 distinct mass peaks). Note the single-sided deflections. (b) The normalized magnetization probability distribution determined from the deflections in (a)$N = 20$; $M/N = 0.83\ \mu_B$; $\mu/N = 2.3\ \mu_B$; $x = 1.5$; $\Delta M/N \approx 0.4$. (c) Normalized magentization distributions of Co_N ($12 \leq N \leq 200$, $T = 40$ K, $B = 2$ T). Amplitudes are represented in color (blue: low; red: high). The magnetization is linear with N for small N and saturates at about $\mu(N) \approx 2N\ \mu_B$ for large N.

In Appendix B, we estimate that at these low source temperatures, there are no phonons in the clusters. So the spin relaxation model cannot be applied to explain the single sided deflections (see 2.2.1).

4.1.2 Average magnetization

The magnetization distribution of Co_N is not a simple delta function, which needs to be explained. We first look at the average magnetization.

4.1.2.1 Raw data

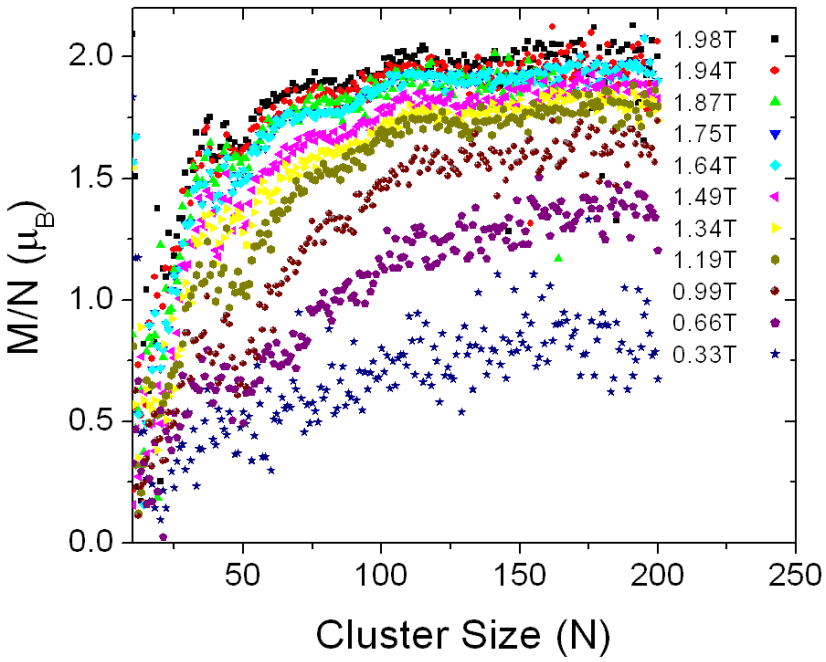

Figure 14: Average magnetization of Co_N clusters at source temperature $T = 25$ K.

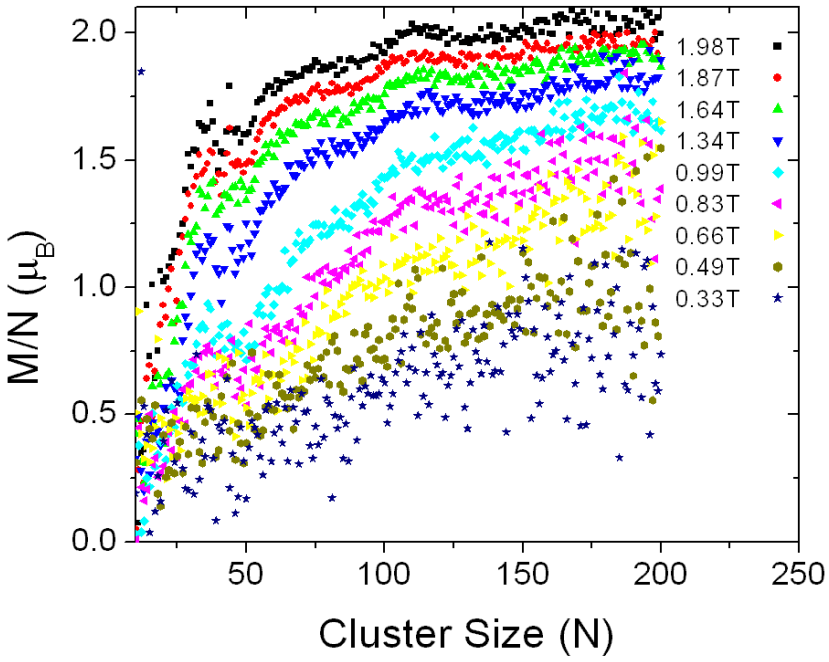

Figure 15: Average magnetization of Co_N clusters at source temperature $T = 35$ K.

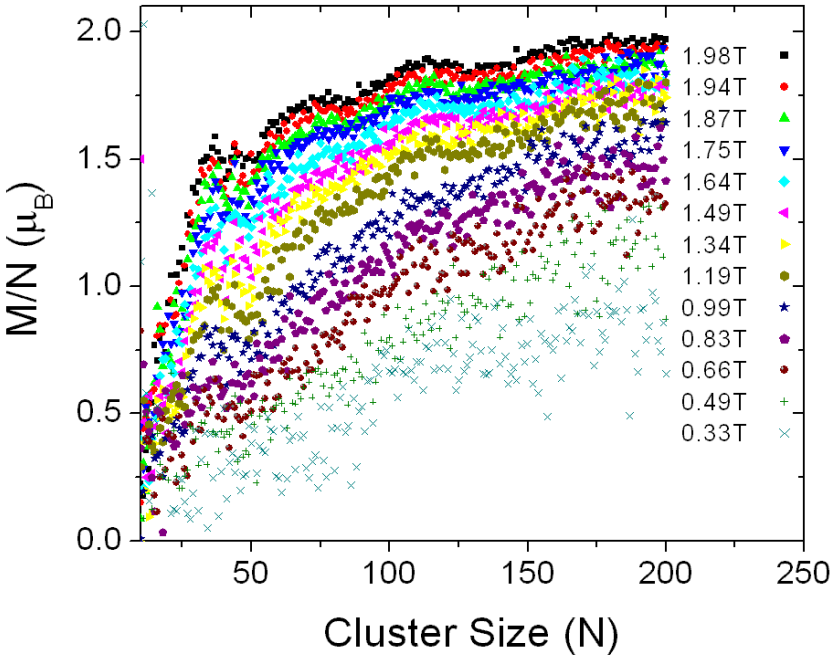

Figure 16: Average magnetization of Co_N clusters at source temperature $T = 40$ K.

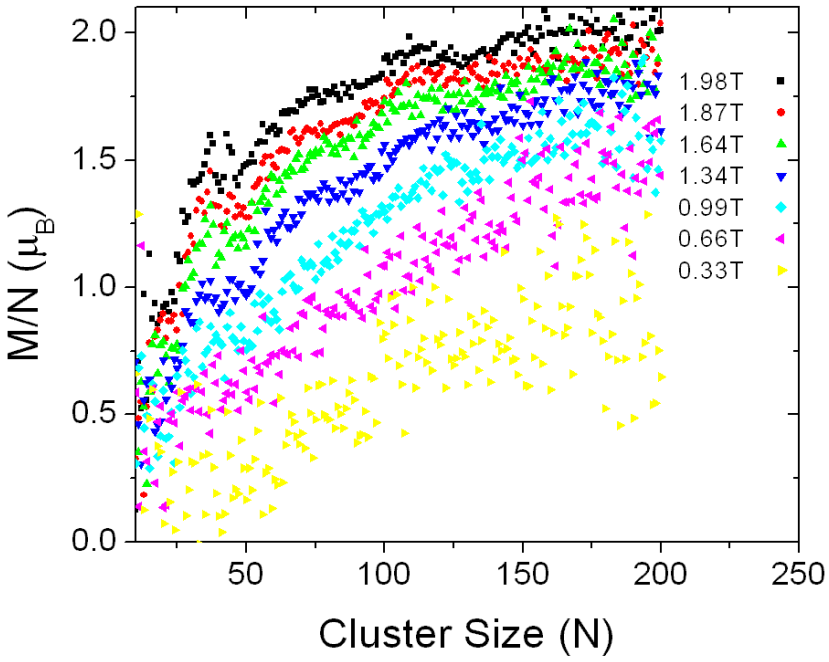

Figure 17: Average magnetization of Co_N clusters at source temperature $T = 50$ K.

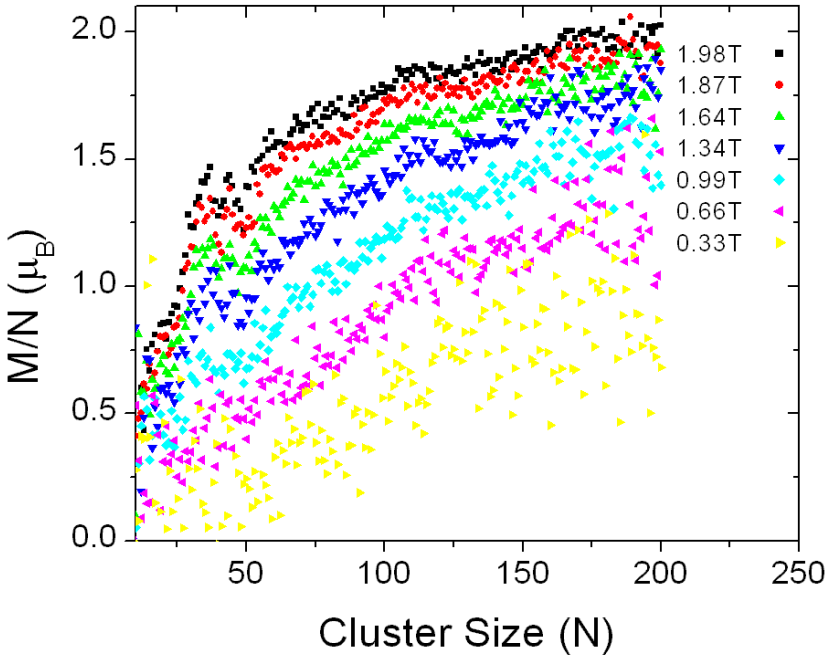

Figure 18: Average magnetization of Co_N clusters at source temperature $T = 60$ K.

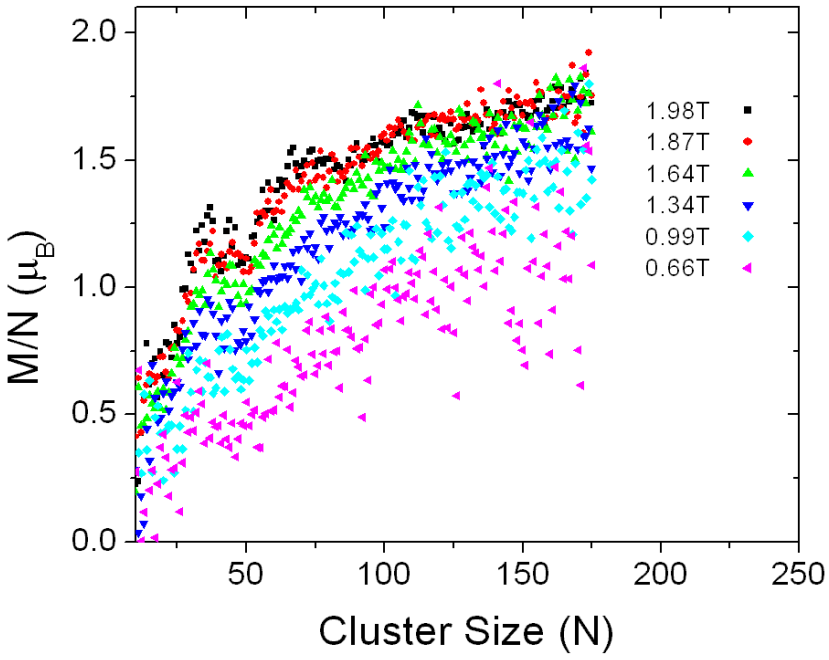

Figure 19: Average magnetization of Co_N clusters at source temperature $T = 70$ K.

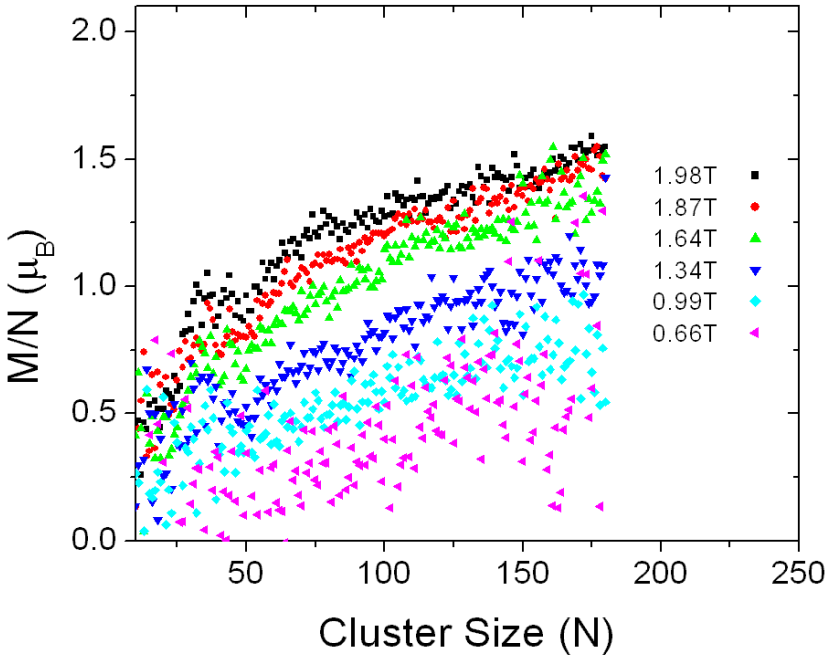

Figure 20: Average magnetization of Co_N clusters at source temperature $T = 80$ K.

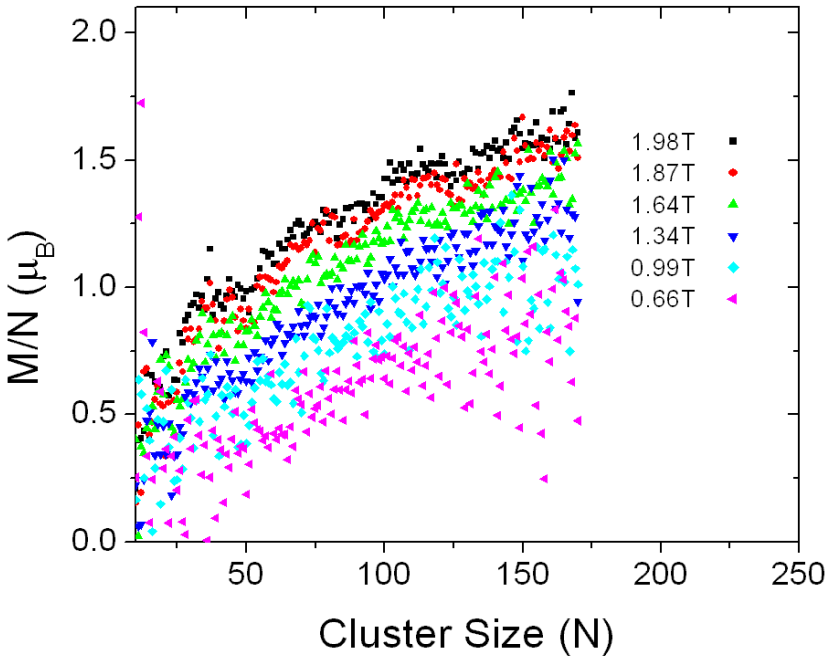

Figure 21: Average magnetization of Co_N clusters at source temperature $T = 90$ K.

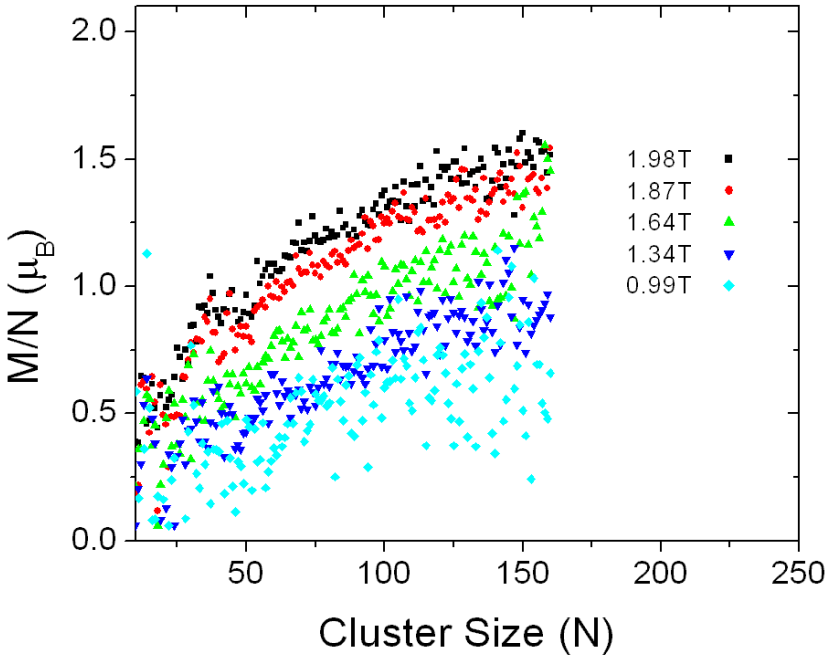

Figure 22: Average magnetization of Co_N clusters at source temperature $T = 100$ K.

Figure 14 through Figure 22 show the average magnetization of Co_N clusters for various source temperatures and magnetic fields. The average magnetization is obtained from the $1st$ moment of the beam profiles. The error bars are not plotted. Since the uncertainties are inversely proportional to deflections, the error bars are smaller for larger deflections. This can be seen from the dispersion of the data.

4.1.2.2 Analysis

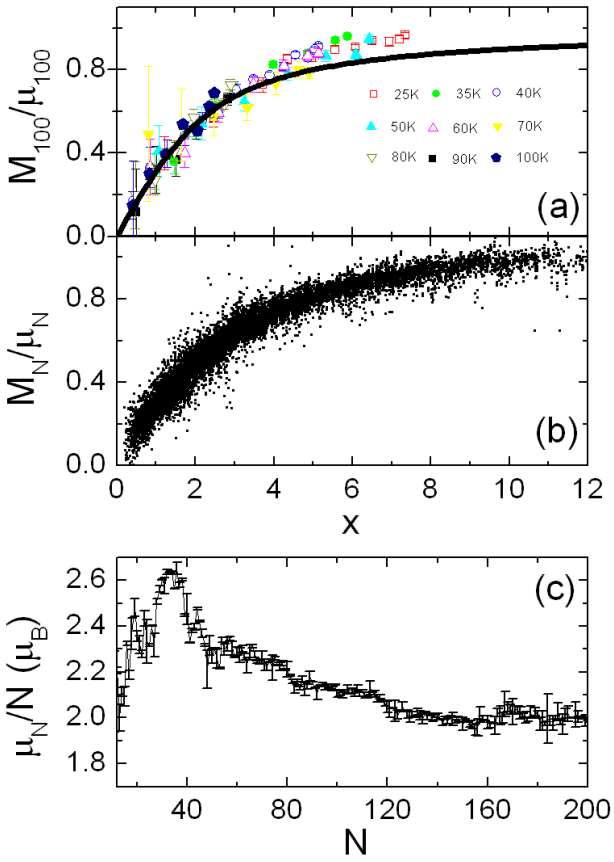

Figure 23: Magnetic moments μ_N and normalized magnetization M_N/μ_N of Co_N. (a) M_N/μ_N of Co_{100} for 25 K$\leq T \leq$ 100 K and $0 < B \leq 2$ T, corresponding to x ($\frac{\mu B}{k_B T}$) ranging from 0.4 to 12. The data scale with x. Note the linear increase for small x: $M_{100}/\mu_{100} \approx 0.3x$ and $M_{100}/\mu_{100} = 1$ for large x. The trend is consistent with the Langevin function (bold line) however the Langevin function approaches saturation more slowly. (b) M_{100}/μ_{100} for $12 \leq N \leq 200$, 20 K$\leq T \leq$ 100 K and $B \leq 2$ T measured in 71 data sets, plotted as a function of x. (c) Magnetic moments per atom for Co_N. Note that $M_{12}/12 \approx 2\ \mu_B$; M_N/N increases to a maximum at $N = 37$ followed by a gradual decrease with weak oscillations converging to 2 μ_B for $N = 150$.

We carefully analyze the magnetization data in order to verify (39). First, we note that the magnetization of large clusters saturate so that their magnetic moments can be immmediately deduced, since in this limit the magnetization is the magnetic moment. In detail, consider the experimental relation $\frac{M_N}{\mu_N} = f(x)$ where $x \equiv \frac{\mu_N B}{k_B T}$. As shown in Figure 23a, for Co_{100} the relation $f(x)$ found from different fields and temperatures falls on a universal curve which resembles the Langevin function $L(x)$, as indicated by the bold line. In the low x range $f(x)$ matches $L(x)$ very well. Note however that for large x, $f(x)$ saturates faster than predicted by $L(x)$.

Since the total magnetic moments are smaller for smaller clusters, the available magnetic fields (≤ 2 T) are too small to saturate the magnetization. Therefore, the magnetic moments of small clusters cannot be found by that method. However, because we already have a well defined magnetization curve $\frac{M_N}{\mu_N} = f(x)$ that is shown to be universal for large clusters, we can extrapolate the magnetic moments of small clusters by fitting their magnetization curves to this universal curve.

Figure 23b show the magnetization curve $\frac{M_N}{\mu_N} = f(x)$ for all cluster sizes investigated. The universal curve $f(x)$ is represented by more than $10,000$ experimental points. The magnetic moments per atom for all cluster sizes were also found, which are consistent with the magnetic moments found previously [30] [48] [21], as shown in Figure 23c, more details have been revealed however: the magnetic moments oscillate with the cluster size dramatically with a maximum around $N = 37$; at $N = 23$, 41, 51, 83 and 121, the magnetic moments have local minima. The magnetic moments converge to 2 μ_B per atom for cluster $N > 150$.

4.1.3 Magnetization distribution

As shown in Figure 13, the magnetization distribution of a cluster beam is by no means a delta function. The average magnetization is only one parameter for characterizing the magnetization distribution. We next look at the broadening of the beam profiles when the magnetic field is turned on. This is related to the width of the magnetization distributions. The broadening ΔW is defined as the geometric difference between second moment of $I^{on}(\delta)$

(W^{on}) and second moment of $I^{off}(\delta)$ (W^{off}): $\Delta W = \sqrt{(W^{on})^2 - (W^{off})^2}$. If we convert ΔW from deflection to magnetization using (47), we obtain the width of the magnetization distribution ΔM.

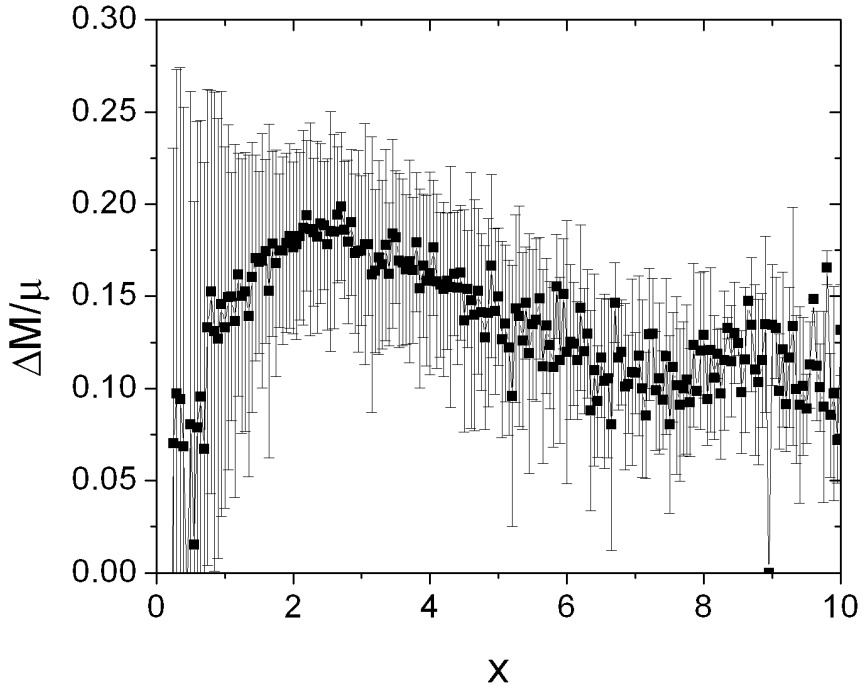

Figure 24: The normalized width of magnetization $\frac{\Delta M}{\mu}$ distribution as a function of ratio $x = \frac{\mu B}{k_B T}$. The data points are found by averaging the values of $\frac{\Delta M}{\mu}$ for clusters conditions over a small range of $\frac{\mu B}{k_B T}$. Note that the 2nd moment of a beam profile is more sensitive to random noise than its 1st moment, which brings significant uncertainty.

From the analysis of the average magnetization, we have found the scaling rule for the average magnetization and the magnetic moments for all the clusters. Based on that, we can look at the relative width of magnetization distribution $\frac{\Delta M}{\mu}$.

Figure 24 gives a qualitative picture of the magnetization distribution. The distribution width starts small at low fields, increases to a maximum at intermediate fields and reduces again at high fields.

4.2 Explanation: Avoided crossing theory

We next address the following paradox: while the statistical thermodynamics of the SR model fails for small clusters at low temperatures as pointed out in 2.2.1, nevertheless the experiment (Figure 23) shows that the Langevin function (39), which follows from the SR model is a reasonable approximation. Clearly, the Langevin function (39) is approximately valid for some other reason. We investigate this carefully below.

For a system in a magnetic field, one has the generic Hamiltonian

$$H_{total} = H_{B=0} + H_{mag},$$

where $H_{B=0}$ is the Hamiltonian when there is no magnetic field and H_{mag} is the part of Hamiltonian that is magnetic field dependent. The magnetization is

$$M \equiv -\frac{1}{V} \ll \frac{\partial H_{mag}}{\partial B} \gg,$$

where V is the volume and $\ll\gg$ denotes the average over the duration of measurement time.

Recall from 2.2.1 that the SR model breaks down at low temperatures for small cold isolated clusters because there is no heat bath. Here the term "heat bath" denotes the degrees of freedom with which H_{mag} may exchange energy and angular momentum. For reference, we list possible heat baths of various systems in Table 3.

Table 3: Possible heat baths and selection rules for different systems.

Systems	Free atoms	Free clusters	Supported clusters	Bulk
Heat bath	electronic excitation	rotation, vibration, electronic excitation	torsion, vibration, excitations from substrate	vibration, electronic excitation
Selection rules	E_{total}, J_z constant	E_{total}, J_z constant		

For free atoms (atoms in a beam), the only degree of freedom available to be the heat bath is the electronic excitation. In contrast, free clusters have rotations and vibrations with

much lower energy scales. For bulk systems, there are vibrations and electronic excitations but no rotations. The heat bath for supported clusters can be the substrate and/or their own vibrations and rotations.

The other critical difference between these systems is the ergodicity. As discussed in Appendix B.3, ergodicity is lowered by selection rules. Systems that have no selection rules are ergodic and are also called irregular systems, while the opposite are called regular systems [142] [18]. Table 3 shows the selection rules of different systems. Free atoms are very regular systems because the electronic degree of freedom are normally not excited at all, leaving H_{mag} almost the only term in the total Hamiltonian. The supported clusters and bulk are the most irregular systems. Free clusters are in between. In this case, we should take into account the details of the total Hamiltonian and the selections rules.

4.2.1 The spin Hamiltonian of free ferromagnetic clusters

For iron group clusters, we can write $H_{mag} \approx -g_{Lande}\mu_B \overrightarrow{S} \cdot \overrightarrow{B} = -g_{Lande}\mu_B S_z B$ as a good approximation, where $g_{Lande} \approx 2$, even though still there may be residual orbital contributions to the total electronic angular momentum. The magnetic moment of the cluster is defined as $\mu \equiv g_{Lande}\mu_B S \approx 2\mu_B S$. The total Harmiltonian of free clusters can be written in the form:

$$\begin{aligned} H_{cluster}(B) &\approx H_{Vib} + H_{Rot} + H_{couple} - g_{Lande}\mu_B S_z B \\ &= H_{Vib} + H_{Rot} + H_{couple} - 2\mu_B S_z B, \end{aligned} \tag{49}$$

where H_{Vib} is the vibrational Hamiltonian, H_{Rot} is the rotational Hamiltonian and H_{couple} is the off-diagonal term that couples different states while conserving energy and angular momentum.

4.2.2 Physical process

4.2.2.1 Cluster generation

Clusters are generated in the source at temperature T in magnetic field $B = 0$, therefore clusters populate energy levels $E_i(0)$. We assume that H_{couple} is small compared to all the other terms in (49) (see 4.2.3.1). Therefore, the eigenstates are linear combinations

of eigenstates of vibrations and rotations E_i^{VR}. The cluster is described by a Boltzmann distribution

$$n(E_i(0)) \propto e^{-E_i(0)/k_BT} = e^{-E^{VR}/k_BT}. \tag{50}$$

4.2.2.2 Adiabatic evolution of energy levels

A cluster in the beam will enter the magnetic field where its magnetization is measured. If there is no coupling between the spin and rotations, the energy levels will evolve as

$$E_i^{uncouple}(B, S_z) = E_i^{VR} - 2\mu_B S_z B.$$

However, if the coupling is nonzero, then when the two levels $E_i^{uncouple}(B, S_z)$ and $E_j^{uncouple}(B, S_z')$ become degenerate, at say $B = B_0$, and if they have the same J_z, they will interact. In the vicinity of that degeneracy, the energies are determined using degenerate perturbation theory. For two nearly degenerate levels $E_i(B, S_z)$ and $E_j(B, S_z')$ (assuming a constant spin-rotation coupling Δ_{SR}), the secular equation [159] that describes the perturbation is:

$$H_{cluster} = \begin{bmatrix} E_i^{VR} - 2\mu_B S_z B & \Delta_{SR} \\ \Delta_{SR} & E_j^{VR} - 2\mu_B S_z' B \end{bmatrix}. \tag{51}$$

Hence the perturbed energy levels are:

$$\begin{aligned} E_i^{couple}(B) &= \frac{E_i^{VR} + E_j^{VR} - 2\mu_B S_z' B - 2\mu_B S_z B}{2} \\ &\quad + \frac{\sqrt{(E_i^{VR} - E_j^{VR} - 2\mu_B S_z' B + 2\mu_B S_z B)^2 + 4\Delta_{SR}^2}}{2} \; and \\ E_j^{couple}(B) &= \frac{E_i^{VR} + E_j^{VR} - 2\mu_B S_z' B - 2\mu_B S_z B}{2} \\ &\quad \frac{-\sqrt{(E_i^{VR} - E_j^{VR} - 2\mu_B S_z' B + 2\mu_B S_z B)^2 + 4\Delta_{SR}^2}}{2}. \end{aligned} \tag{52}$$

As shown in Figure 25, an avoided level crossing occurs at the level intersection. The magnetization (which is the slope of the adiabatic level) reverse at the degeneracy point $B = B_0$. At the degeneracy point, S_z is not a good quantum number because of the coupling. The magnetization is effectively the average of the two levels, as shown in Table 4.

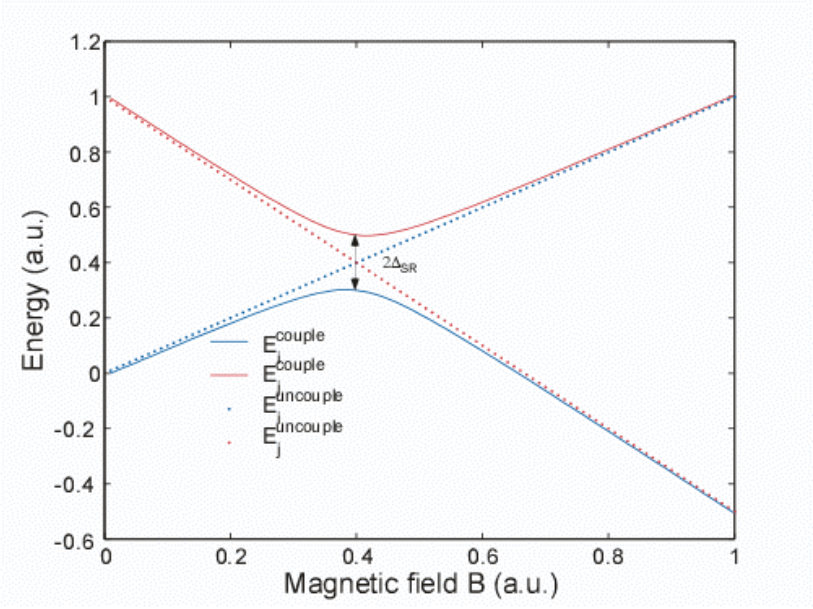

Figure 25: Schematic illustration of an avoided level crossing. Notice that the coupling makes the spin orientation "flip" at the degeneracy point, since the crossing of the two levels is avoided.

Table 4: Energies and magnetizations of two levels with an avoided crossing.

	$B \ll B_0$	$B = B0$	$B \gg B_0$
$E_i^{couple}(B)$	$E_i^{couple}(B)$	$\frac{E_i^{couple}(B)+E_i^{couple}(B)}{2} + \Delta_{SR}$	$E_j^{couple}(B)$
$E_j^{couple}(B)$	$E_j^{couple}(B)$	$\frac{E_i^{couple}(B)+E_i^{couple}(B)}{2} - \Delta_{SR}$	$E_i^{couple}(B)$
$M_i^{couple}(B)$	$2\mu_B S_z$	$\mu_B S_z + \mu_B S'_z$	$2\mu_B S'_z$
$M_j^{couple}(B)$	$2\mu_B S'_z$	$\mu_B S_z + \mu_B S'_z$	$2\mu_B S_z$

Because of the large density of rotational levels, a cluster will negotiate a large number of avoided crossings in its passage through the magnetic field. At each crossing, the number of interacting levels can be more than two. For clusters that follow the energy levels $E_i^{couple}(B)$ adiabatically, their magnetization will switch at every avoided level crossing. This results in a reduced average magnetization. Note that spin relaxation is not involved. In fact, the process is, in principle, reversible.

We next show the energy diagram of Co_{10} as an example. Figure 26 shows a small region of the Zeeman diagram with all the level crossings avoided. For each level the average slope is more or less the same negative number because of the level repulsion.

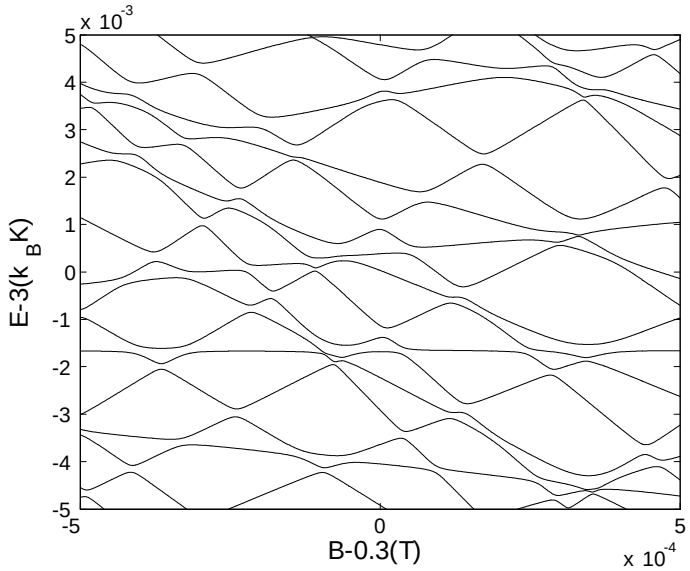

Figure 26: Zeeman diagram of Co_{10} with $J_z = 0$ at the vicinity of $B = 0.3$ T, $E^{couple}/k_B = 3$ K. Note that every level crossing is avoided.

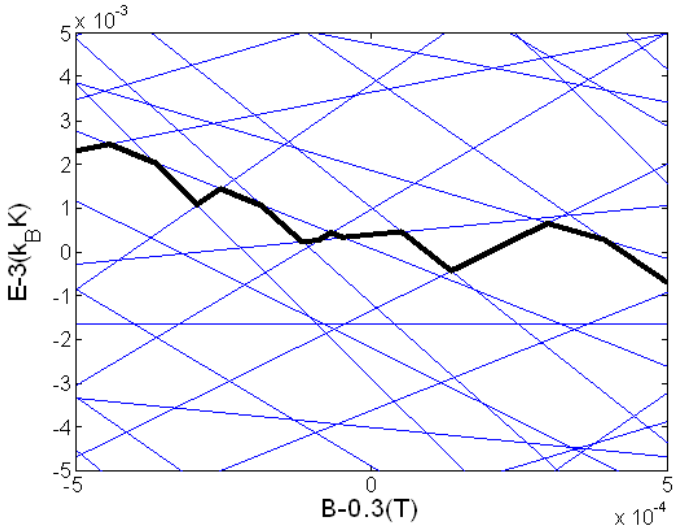

Figure 27: The energy levels of cluster Co_{10} with $J_z = 0$ at the vicinity of $B = 0.3$ T, $E^{couple}/k_B = 3$ K in a range of $dB = 10^{-3}$ T, $dE/k_B = 10^{-2}$ K. The blue curves are the uncoupled levels. The black bold curve is one of the adiabatic energy levels.

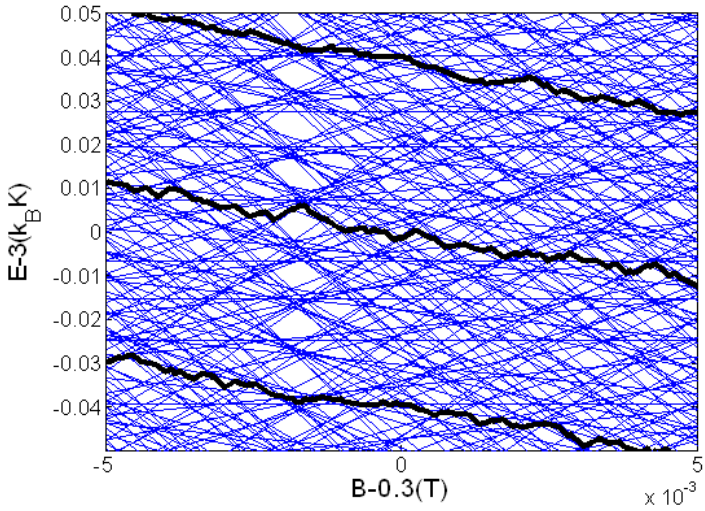

Figure 28: The energy levels of cluster Co_{10} with $J_z = 0$ at the vicinity of $B = 0.3$ T, $E^{couple}/k_B = 3$ K in a range of $dB = 0.01$ T, $dE/k_B = 0.1$ K. The blue curves are the uncoupled levels. The black bold curves are some of the adiabatic energy levels.

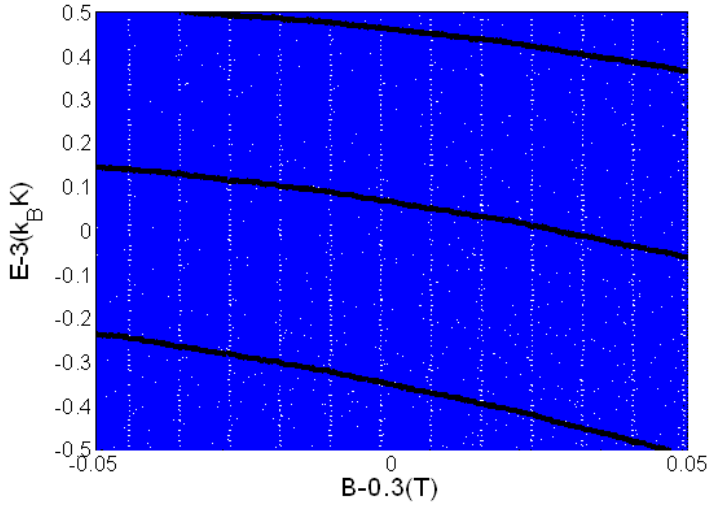

Figure 29: The energy levels of cluster Co_{10} with $J_z = 0$ at the vicinity of $B = 0.3$ T, $E^{couple}/k_B = 3$ K in a range of $dB = 0.1$ T, $dE/k_B = 1$ K. The blue curves that represent the uncoupled levels are barely resolved. The black bold curves are some of the adiabatic energy levels.

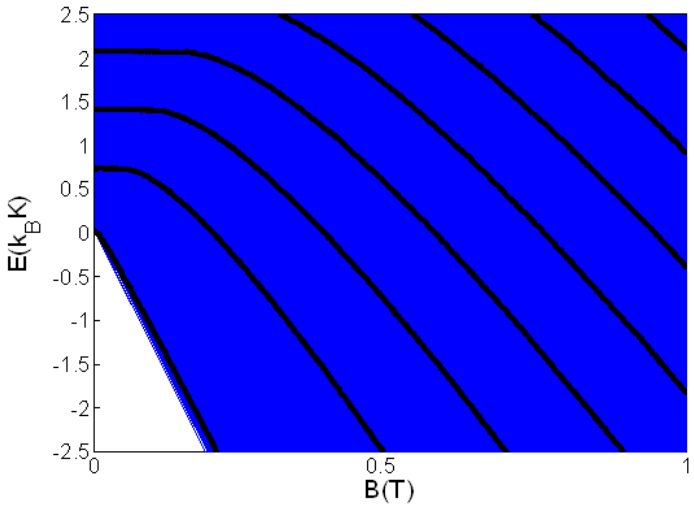

Figure 30: The energy levels of cluster Co_{10} with $J_z = 0$. The uncoupled levels(blue) are so many that they become the blue background. The black bold curves are some of the adiabatic energy levels.

Figure 27 through Figure 29 show the adiabatic levels as well as the uncoupled levels on different scales. It is clear that for the larger scales, the adiabatic levels become smoother. Figure 30 shows a global view of the energy levels which reveals the key features of these energy levels: they start with zero slope and get steeper and steeper until the slope reaches saturation at high field; the slopes of the levels are all negative, which explains the single sided deflection. Clusters at different adiabatic levels have different magnetization, which explains the broadening of the deflected beam profiles compared to the beam profiles without magnetic field. It is important to notice again that the measurements are taken with magnetic fields in the range 10^{-3} T to 10^{-2} T, which means fine details of the adiabatic levels are not measured. These details are smeared so that the averages over the range in Figure 29 or in Figure 28 are measured.

4.2.2.3 Magnetization of the cluster beam

Magnetization of a single cluster If we know the adiabatic levels, we can calculate the magnetization of a specific cluster. Recall from Table 4 that the magnetization of an adiabatic level is the average over all the interacting uncoupled levels in a certain range, we can write down the magnetization of a cluster with energy E at magnetic field B

$$M_{cluster}(E,B) = 2\mu_B \frac{\sum_{S_z=-S}^{S} S_z D(E^{uncouple}(B,S_z))}{\sum_{S_z=-S}^{S} D(E^{uncouple}(B,S_z))}, \tag{53}$$

where $D(E^{uncouple}(B,S_z))$ is the number of uncoupled levels in the measurement range (a range ΔB centered at B). Since the number of levels in the measurement range is much greater than 1, we can treat the summation as an integral

$$\begin{aligned} M_{cluster}(E,B) &= 2\mu_B \frac{\int_{-S}^{S} S_z D_{os}(E^{uncouple}(B,S_z))dS_z}{\int_{-S}^{S} D_{os}(E^{uncouple}(B,S_z))dS_z} \\ &= 2\mu_B \frac{\int_{-S}^{S} S_z D_{os}(E^{VR} - 2\mu_B S_z B)dS_z}{\int_{-S}^{S} D_{os}(E^{VR} - 2\mu_B S_z B)dS_z}, \end{aligned} \tag{54}$$

where $D_{os}(E^{uncouple}(B,S_z))$ is the density of states for the uncoupled levels.

Equations (53) and (54) allow us to find the average slope of an adiabatic level over the measurement range without diagonalizing the Hamiltonian. In the experiments, we

accumulate data for many clusters so that in fact we measure the statistical behavior of the entire cluster beam. Therefore, to compare with experiments, we have to average over the ensemble of the cluster beam.

Magnetization of the cluster beam To find the ensemble average, we have to deal with the cluster population at various energies. Since the clusters follow their energy levels adiabatically into the magnetic field, the cluster populations are not determined by the energies in the magnetic field but by the energies before they enter the magnetic field (i.e., their energies in the source). Thus, we should trace the adiabatic level $E^{couple}(B)$ back to $E^{couple}(0) = E^{VR}$, and use the Boltzmann statistics corresponding to the source conditions. Therefore, the magnetization of the cluster beam is

$$M_{beam}(B) = < M_{cluster} > \quad (55)$$

$$= \frac{\int M(E^{couple}(B)) e^{-E^{couple}(0)/k_B T} D_{os}(E^{couple}(0)) dE^{couple}(B)}{\int e^{-E^{couple}(0)/k_B T} D_{os}(E^{couple}(0)) dE^{couple}(B)}. \quad (56)$$

High field limit According to Figure 30, the magnetization of almost all the clusters saturates at $M_{cluster} = 2\mu_B S$, so the high field average should be

$$M_{beam} = M_{cluster} = 2\mu_B S = \mu.$$

The high field magnetization distribution should be a delta function $\delta(M - \mu)$ with width $\Delta M = 0$.

Low field limit In this case, the density of states in (54) can be expanded

$$D_{os}(E^{VR} - 2\mu_B S_z B) \approx D_{os}(E^{VR}) - 2\mu_B S_z B \frac{\partial D_{os}(E^{VR})}{\partial E}.$$

Therefore

$$M_{cluster}(E, B) \approx \frac{4S^2 \mu_B^2 B}{3 D_{os}(E^{VR})} \frac{\partial D_{os}(E^{VR})}{\partial E}.$$

Since the magnetization of the clusters is small, a first order approximation

$$E^{VR} \approx E^{couple}(0) \approx E^{couple}$$

can be used in (55). Hence, the average magnetization of the beam is

$$\begin{aligned} M_{beam} &= \frac{\int \frac{4S^2\mu_B^2 B}{3D_{os}(E^{VR})}\frac{\partial D_{os}(E^{VR})}{\partial E}D_{os}(E^{VR})e^{-E^{VR}/k_BT}dE^{VR}(B)}{\int e^{-E^{VR}/k_BT}D_{os}(E^{VR})dE^{couple}(B)} \\ &= \frac{4S^2\mu_B^2 B}{3}\frac{\int \frac{\partial D_{os}(E^{VR})}{\partial E}e^{-E^{VR}/k_BT}dE^{VR}(B)}{\int e^{-E^{VR}/k_BT}D_{os}(E^{VR})dE^{VR}(B)} \\ &= \frac{4S^2\mu_B^2 B}{3k_BT} = \frac{\mu^2 B}{3k_BT}. \end{aligned} \tag{57}$$

Note that this corresponds to the low field limit of Langevin function (40)!

The magnetization distribution is

$$P(M) = \left|\frac{D_{os}(E^{VR})e^{-E^{VR}/k_BT}}{\partial M_{cluster}(E,B)/\partial E}\right|.$$

Suppose that $D_{os}(E^{VR}) = C_{DOS}(E^{VR})^{g_{DOS}}$, where C_{DOS} is a constant, one finds

$$P(M) = C_{DOS}(\frac{4S^2\mu_B^2 B g_{DOS}}{3})^{g_{DOS}+1}\frac{1}{M^{g_{DOS}+2}}e^{-\frac{4S^2\mu_B^2 B g_{DOS}}{3k_BT}}.$$

The distribution width will be

$$\begin{aligned} \Delta M &= \sqrt{< M_{Cluster}^2 > - < M_{Cluster} >^2} \\ &= \sqrt{< M_{Cluster}^2 > - M_{beam}^2} \\ &= \sqrt{\frac{\int M^2 P(M)dM}{\int P(M)dM} - (\frac{\mu^2 B}{3k_BT})^2} \\ &= \frac{\mu^2 B}{3k_BT}\sqrt{\frac{1}{g_{DOS}-1}}. \end{aligned}$$

Note that this is only for the case that $g_{DOS} > 1$. For other cases, the calculation should be done differently.

Intermediate field In this case, we have to calculate (54) and (55) numerically. What we need to know here is the power law of density of states. Assuming that $D_{os}(E^{VR}) \propto (E^{VR})^{g_{DOS}}$, we can calculate the beam magnetization. The power g_{DOS} is related to the degrees of freedom that are excited. If no vibrational modes are excited, then $g_{DOS} = 0$ (because of the J_z conservation). If one vibrational mode is excited, $g_{DOS} = 1$.

Figure 31 shows the magnetization distribution profile calculated for Co_{10} under various conditions. For different g_{DOS}, all the peaks of the distributions follow the overall trend:

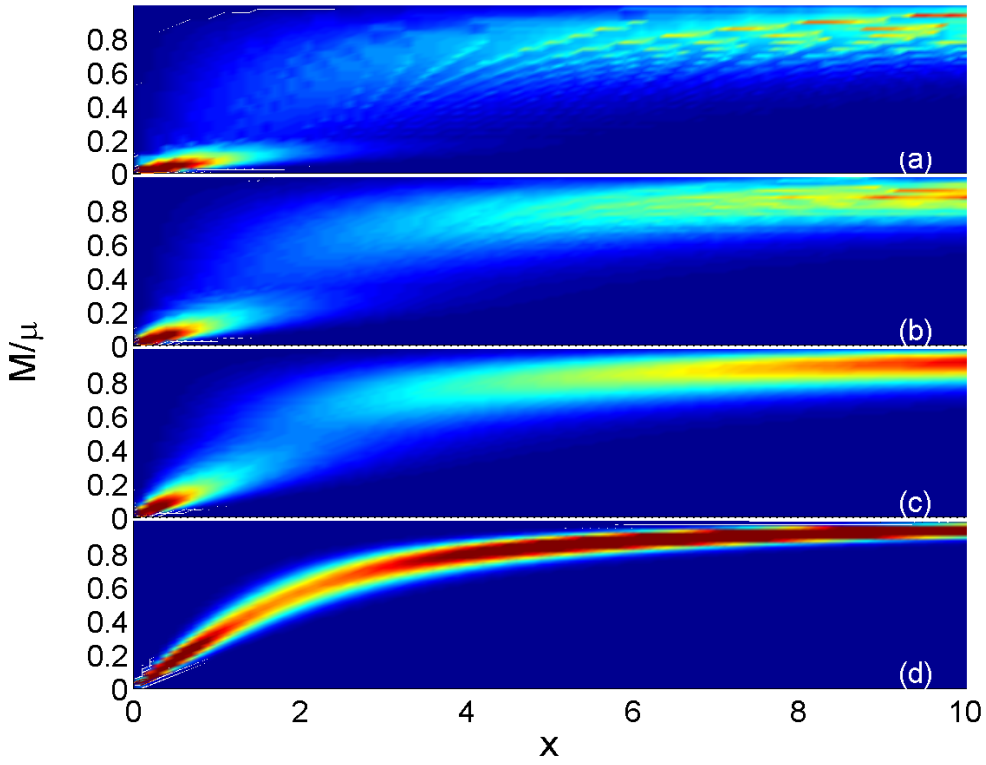

Figure 31: Calculated magnetization distribution for cluster Co_{10} for various conditions $x = \frac{\mu B}{k_B T}$. (a) $g_{DOS} = 0.5$; (b) $g_{DOS} = 1$; (c) $g_{DOS} = 2$; (d) $g_{DOS} = 20$; Amplitude are represented in color (blue: low; red: high).

start at $\frac{M}{\mu} = 0$ for low field and saturate at $\frac{M}{\mu} = 1$. The widths of the distributions for various g_{DOS} are clearly different: the larger the g_{DOS}, the narrower the distribution. However, the distributions are all narrow for low field and become wider for higher field until they reach a maximum and become narrow again at very high field. The average magnetization and the distribution width are found from the first and second moments of these magnetization distributions.

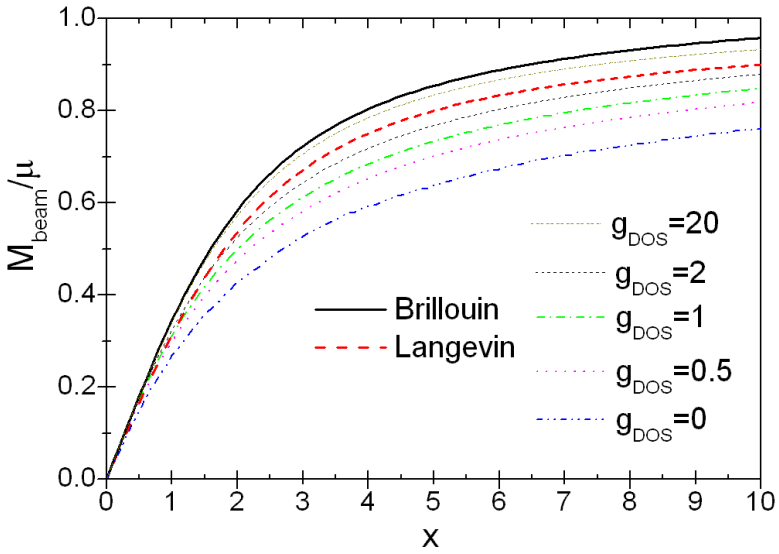

Figure 32: Average magnetization of Co_{10} in the beam calculated for various different conditions for various g_{DOS}.

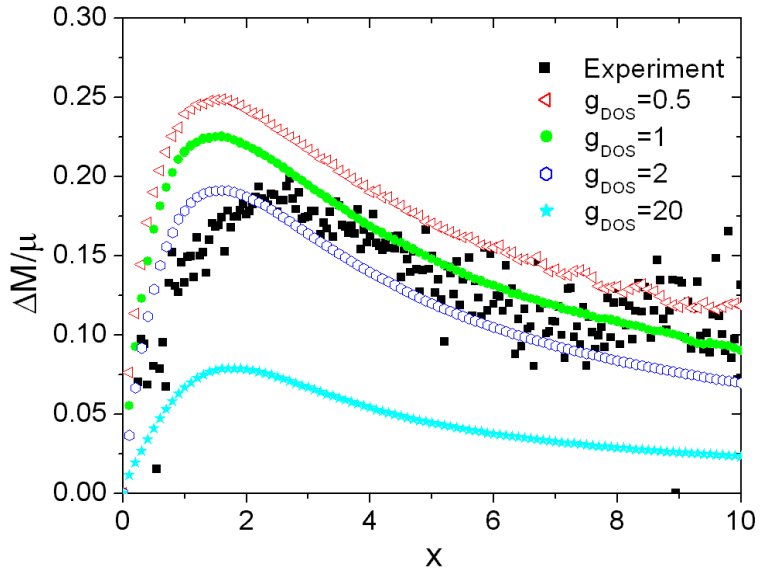

Figure 33: Width of magnetization distribution for Co_{10} in the beam calculated as a function of $x = \frac{\mu B}{k_B T}$ for various g_{DOS} and compared with experimental results.

Figure 32 shows the average magnetization for cluster Co_{10} as a function of $\frac{\mu B}{k_B T}$. For all different g_{DOS}, the low field limits show the same trend for all clusters, large and small (see (57)). At high field, the larger the power g_{DOS} is, the faster the magnetization saturates. For very large g_{DOS}, this relation converge to the Brillouin function rather than the Langevin function because the total spin of Co_{10} is not large enough.

Figure 33 shows the calculated width of the magnetization distribution as well as the experimental values (same as Figure 24 but without error bars). Note that the width of magnetization distribution is narrower for larger g_{DOS}.

4.2.3 Discussions

We return to the coupling term H_{couple} in Hamiltonian (49). First, we should emphasize that the nature of the coupling is extremely complicated especially for clusters that are asymmetric [175]. We only discuss the order of magnitude of the strength and also some limiting cases.

4.2.3.1 Coupling strength

If we ignore the nuclear spin, the generic form of the coupling is

$$H_{couple} = \alpha_{SR} \overrightarrow{S} \cdot \overrightarrow{R} + \alpha_{SA} (\overrightarrow{S} \cdot \overrightarrow{A})^2,$$

where $\overrightarrow{S}$ is the spin of the electrons, $\overrightarrow{R}$ is the rotation of the cluster, $\overrightarrow{A}$ is one of the body axes of the cluster (assuming single axis anisotropy), α_{SR} and α_{SA} are the strength for spin-rotation coupling and of the spin-body axis coupling respectively. As mentioned in 4.2.2, when the coupling is weak, we can diagonalize the Hamiltonian ignoring the coupling to get the eigenstates $|R, R_z, R_a, S, S_z\rangle$, where R_z and R_a are the projection of $\overrightarrow{R}$ on the magnetic field $\overrightarrow{B}$ and the body axis $\overrightarrow{A}$ respectively. Because of the off-diagonal terms

$$\left\langle R', R'_z, R'_a, S', S'_z \right| H_{couple} \left| R, R_z, R_a, S, S_z \right\rangle \propto \delta_{S_z + R_z, S'_z + R'_z},$$

the crossings of unperturbed energy levels are avoided.

In principle the electron spin only couples to its orbital angular momentum (spin-orbit coupling). For an atom in a cluster or in the bulk, the electric field from other atoms

(crystal field) is not spherically symmetric. Therefore due to the low symmetry of the crystal field, the orbital motion of the electrons has a preferred direction. Different spin-orbit coupling strength and different crystal fields result in different magnetic anisotropy energies [136]. If spin-orbit coupling is larger than the crystal field energy, then the orbital angular momentum is still a good quantum number. The crystal field will eventually cause strong spin-body axis coupling, which is reflected in the anisotropy energy. If the effect of crystal field is larger than the effect of spin-orbit coupling, we have to rediagonalize the electron orbital Hamiltonian including the crystal field energy as off-diagonal terms, which will give eigenstates without orbital angular momentum as good quantum numbers. In other words, the average angular momenta for these eigenstates are quenched. In this case the spin-orbit coupling will be very weak, resulting in less anisotropy energy, as is the case for iron group metals.

In the bulk, the spin-body axis coupling is dominant. For a cluster in a beam, we also have to take into account the rotations, which complicates the problem [175] [179]. Rotational angular momentum may uncouple the electronic spin angular momentum from the body axis and eventually couple it to the rotations, especially for those clusters with no electronic orbital angular momentum.

There are two important mechanisms for the spin-rotation coupling [175].

In one, the rotation of the cluster is like that of a charged sphere which generates a magnetic field parallel to the axis of rotation. In the classical picture, we can estimate the coupling energy. The coupling energy can be treated as the energy of a magnetic dipole moment in a magnetic field, thus

$$\Delta_{SR} \approx \frac{N\mu_B\mu_0 e\omega_{cluster}}{r_{cluster}},$$

where μ_0 is the vacuum magnetic permeability, $\omega_{cluster}$ is the angular frequency of the cluster rotation and $r_{cluster}$ is the radius of the cluster. The average angular frequency of the cluster depends on the rotational temperature as $\frac{2}{5}mr_{cluster}^2\omega_{cluster}^2 = 3k_BT_{rot}$.As shown in Figure 34, the coupling energy is on the order of 10^{-8} eV to 10^{-7} eV and is larger for smaller clusters and higher temperatures.

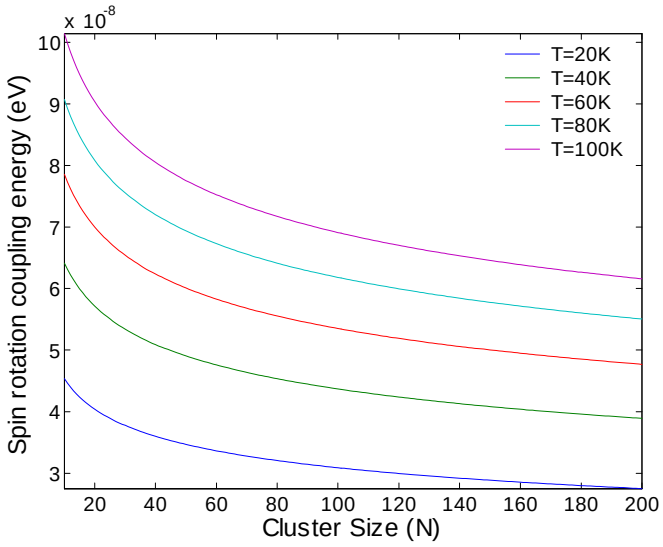

Figure 34: Spin rotation coupling energy calculated using the classical model for Co_N clusters.

The other is momechanism re important: electrons follow the rotation of the cluster and get excited from zero rotation states to higher rotation states. Because of the spin-orbit coupling, the electronic spin is coupled to the direction of rotation. According to van Vleck [179], this is a second order process and the energy is

$$\Delta_{SR} \sim \frac{B_r E_{spinorbit}}{\Delta_e},$$

where B_r is the rotation constant, $E_{spinorbit}$ is the spin-orbit coupling strength, and Δ_e is the energy needed to excite the electrons to higher angular momentum states. If the Δ_e is from the collective rotation of the electrons in the cluster, $B_r/\Delta_e \sim 10^{-3}$. The spin-orbit coupling energy for an electron is about 10^{-4} eV, therefore we get $\Delta_{SR} \sim 10^{-7}$ eV.

Recall from (49) that H_{mag} is on the order of 1 μB. For our experiments, $\mu \approx 2\ \mu_B N$ and $B \sim 1$ T. Hence $H_{mag} \sim 10^{-3}$ eV is much larger than the spin-rotation coupling strength. Thus the approximation we made earlier is justified: the coupling can be treated as a perturbation.

4.2.3.2 Landau-Zener tunneling

We have assumed that the clusters traverse their energy levels adiabatically. Actually, if the magnetic field changes with a finite speed $\frac{dB}{dt}$, there is a finite probability for clusters

to jump between E_i^{couple} and E_j^{couple}. This nonadiabatic process is called a Landau-Zener transition [199]. For the case in Figure 25 the transition rate is given by

$$p_{LZ} = e^{-\frac{2\pi\Delta_{SR}^2}{\mu_B h|S_z - S_z'|\frac{dB}{dt}}} = e^{-\frac{\Delta_{SR}^2}{\Delta_{LZ}^2}},$$

where $\Delta_{LZ} \equiv \sqrt{\frac{\mu_B h|S_z - S_z'|\frac{dB}{dt}}{2\pi}}$.

We can estimate the rate of the changing field from Figure 7:

$$\frac{dB}{dt} \approx \frac{\frac{dB}{dz}\delta_{field}}{\frac{l_{field}}{v}}.$$

Invoking the deflection in a field (46), one gets

$$\frac{dB}{dt} \approx \frac{Ml_{field}(\frac{dB}{dz})^2}{2mv}.$$

For typical experiments, we find $\frac{dB}{dt} \approx 50$ T/s, therefore $\Delta_{LZ} \sim 10^{-8}$ eV.

Apparently $\Delta_{SR} \gg \Delta_{LZ}$, hence $p_{LZ} \sim 0$, which means that the Landau-Zener transitions are not important. In other words, the process is at least approximately adiabatic.

Actually, the process does not have to be totally adiabatic for the conclusion to hold. We can estimate the number of crossings within the measurement range

$$N_{crossing} \approx \frac{\mu\Delta B}{B_r},$$

where $\Delta B = \frac{dB}{dz}\delta_{field}$ is the field change in the measurement range and B_r is the rotational constant of the cluster. Using the formula (46), we find

$$N_{crossing} \approx \frac{\mu\frac{dB}{dz}\delta_{field}}{B_r} = \frac{(\mu\frac{dB}{dz}l_{field})^2}{2mv^2B_r}.$$

For a typical experiment, we find for cluster Co_{100} that $N_{crossing} \approx 1000$. Even if only one of these crossings is actually avoided, the average magnetization will still show significant reduction compared with totally uncoupled cases.

4.2.3.3 Strong coupling cases

For iron group metal clusters, we can treat the couplings as perturbations (see 4.2.3.1). Still there are other cases in which the coupling energy is stronger than the Zeemam energy H_{mag}. One example is the clusters with strong spin-axis coupling or a large anisotropy

energy. Some rare earth metal clusters fall into this category. The other case is from clusters with large spin-rotation coupling. This occurs for very small clusters because they rotate very fast [175].

Strong spin-body axis coupling Here, we can consider the electronic spin fixed to one of the body axes. The Hamiltonian will be similar to (49)

$$H_{cluster}(B) \approx H_{Vib} + H_{Rot} + H_{couple} - g_{Lande}\mu_B S\frac{J_z J_a}{J(J+1)}B,$$

where J is the total angular momentum including electronic spin and cluster rotations. J_z and J_a are the projection of $\overrightarrow{J}$ on magnetic field ($\overrightarrow{B}$) and body axis (same as $\overrightarrow{S}$) respectively [175]. We can follow the same procedure as we did for (49). Plotting the energy $H_{Vib} + H_{Rot} - g_{Lande}\mu_B S\frac{J_z J_a}{J(J+1)}B$, we will see many level crossings. The spin-rotation coupling H_{couple} at the degenerate point for the levels with same J_z will cause the crossing to be avoided. Therefore if clusters follow these levels adiabatically, we should see a very similar behavior as in the weak coupling case. Bertsch et al. have shown [68] that this is indeed the case (40). The magnetization distribution is also similar to that described by (49), which shows exclusively single-sided deflections. However, Bertsch et al. ignored that the magnetization is measured within a finite range of magnetic fields, so they concluded the magnetization distribution should be wide and clusters should show negative deflections. In fact, the experimental averaging mechanism causes narrow widths. For example, magnetic deflection experiments on holmium clusters that have large anisotropy energy do not show negative magnetic deflection at all [195].

Strong spin-rotation coupling In this case, we can consider the electronic spin to be perfectly aligned with the cluster rotation, in other words $J = S + R$, therefore

$$H_{cluster}(B) \approx H_{Vib} + H_{Rot} + H_{couple} - g_{Lande}\mu_B SB\frac{J_z}{J},$$

which means that the magnetization distribution is uniform, spanning from $-\mu$ to μ [175]. Again, when the level crossings are avoided, the magnetization distribution will change

significantly. However, the quantitative magnetization distribution in this case has not yet been studied.

4.2.3.4 Crossings that are not avoided

If the crossings are not avoided, we should see a very different behavior in both average magnetization and distribution of magnetization, as summarized in Table 5.

Table 5: Average and distribution of magnetization at low field.

	No coupling	Spin-axis coupling	Spin-orbit coupling
$< M >$	0	$\frac{2}{9}\frac{\mu^2 B}{k_B T}$ (2nd order)	$\frac{2}{9}\frac{\mu^2 B}{k_B T}$ (2nd order)
$P(M)$	$\sum_{S_z=-S}^{S} \delta(M - g_{Lande}\mu_B S_z)$	$\frac{1}{2\mu} ln \left\lvert \frac{\mu}{M} \right\rvert$	$\frac{1}{2\mu}$

If crossings are not avoided at all, the average magnetization is zero to 1st order. For the 2nd order perturbation, the strong coupling case will give an average magnetization that is $\frac{2}{3}$ of what we find from (40). The detailed calculation can be found in [20] [175].

4.2.3.5 Selection rules

As shown in Table 3, the selection rules for different systems are very different causing different behaviors. The selection rules for free clusters are the most complicated. In the calculations so far, we assumed conservation of J_z and energy only. Actually, if we consider spin-rotation coupling $H_{couple} = \alpha_{SR} \overrightarrow{S} \cdot \overrightarrow{R} = \frac{1}{2}\alpha_{SR}(\overrightarrow{J}^2 - \overrightarrow{S}^2 - \overrightarrow{R}^2)$, the eigenstates become $|J, J_z, S, R\rangle$. Since the Clebsch-Gordan [33] coefficient $\langle J, J_z, S, R \,|S', R', S'_z, R'_z\rangle \propto \delta_{S,S'}\delta_{R,R'}\delta_{J,J'}$, the coupling does not mix states with different rotations. Therefore, additional selection rules have to be considered. In this case, the deflections will not be single-sided, because the highest energy levels with positive slope do not intersect any other levels. A good example of this case is a paramagnetic cluster with an unpaired spin [130]. However for a ferromagnetic cluster, the total spin of the cluster is not a good quantum number [127] [31], therefore the spin selection rules do not apply, causing the mixing of states with different rotations. The avoided crossing theory then follows.

4.2.4 Conclusion

The avoided crossing theory explaines the magnetization of small clusters, therefore the spin relaxation paradox is resolved. In summary:

- The single-sided deflections of iron group clusters are not caused by spin relaxation, but are due to the repulsions between the adiabatic levels that reduce the magnetization.
- The broadening of the deflected beam profiles is caused by the magnetization distributions
- Magnetization of cluster beam is found to be close to Langevin function in the high field and the low field limit, but not for intermediate fields.

CHAPTER V

TWO STATES

5.1 Experiment

In the preceding chapter we have examined how a ferromagnetic cluster behaves in the Stern-Gerlach inhomogeneous magnetic field. We found how to extract the magnetic moments from cluster deflections. That is not our goal however. We have just sharpened our tools to deal with the original problem. The question we posed in 1.2.3.12 is: what are the magnetic moments of ferromagnetic clusters?

It may seem that the magnetic moments can be deduced from Figure 23 [192], where the values confirm the previous work mentioned in 2.2.2: the magnetic moments are higher for smaller clusters than for bulk and decrease with cluster size in a oscillating way. It turns out that the real case is more subtle.

As discussed in 3.2, clusters are generated in the laser ablation source, where they thermalize with the source. When the clusters are generated from the metal vapor, they are hot and in excited states. Thermalization of a cluster is acquired by collisions with cold carrier gas atoms that carry away energy from clusters and quench them in lower energy states.

The thermalization is crucial for two reasons. First, only when the thermalization is complete and when clusters reach equilibrium with background gas, we have control of the temperature of the cluster beams. Second, if we thermalize the clusters at very low temperatures, we can quench the clusters in their ground states. While we are most interested in ground state properties, the excited states are also important sources of interaction that reveal the nature of the ground states. To study the excited states, we restrict the thermalization process in a controlled way.

This is clearly more complicated than the perfect thermalization case, as discussed in Appendix B. We take advantage of the different thermalization rates to keep some of the

degrees of freedoms excited. Nevertheless, great care is taken in the analysis when the thermalization is restricted.

5.1.1 Cobalt clusters

5.1.1.1 Magnetic deflections

Magnetic deflection experiments have been carried out both with complete and with restricted thermalization conditions by either reducing the length of the nozzle or the amount of helium gas injected into the source (see Appendix 3.2). Results for Co_{30} are shown in Figure 35.

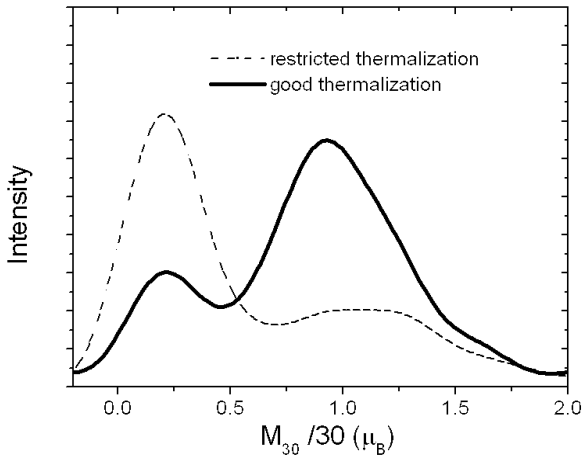

Figure 35: Magnetization distribution profiles of cobalt clusters of 30 atoms in two thermalization conditions. Solid line is for the good thermalization condition; dashed line is for a restricted thermalization condition. $T = 20$ K and $B = 2$ T.

When the thermalization is restricted, the magnetization distribution profile changes. A second peak that deflects less than the original peak becomes distinct. The deflection of original peak does not change, however, but its intensity is reduced. Because the two peaks differ in their deflections (therefore magnetization), we will call them the more-magnetic peak and the less-magnetic peak respectively. The emergence of a second peak occurs for all the clusters observed. The proportion of the two peaks in the beam changes continuously when the thermalization condition is tuned, as shown in Figure 36. One can quench either peak (Figure 36a, Figure 36c) or keep them both (Figure 36b) by tuning the thermalization condition. Again, no matter what the proportion of the two peaks is, their positions are

unchanged as long as the source temperature and the magnetic field are unchanged.

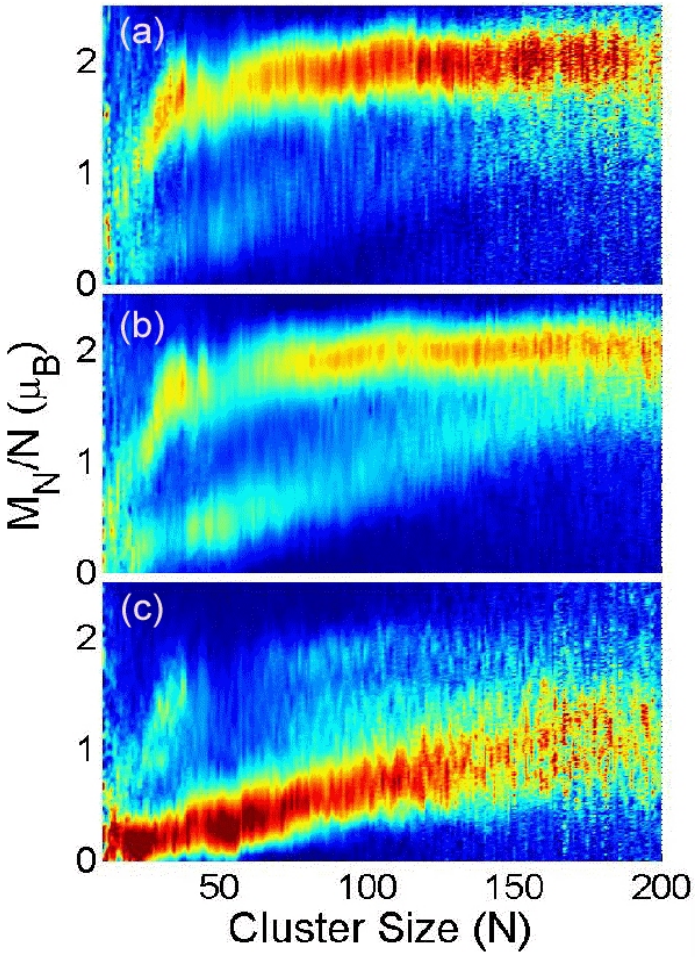

Figure 36: The normalized magnetization probability distribution of Co_N ($10 \leq N \leq 200$, $T = 20$ K, $B = 2$ T). (a) Ideal thermalization. (b) Intermediate thermalization. (c) Restricted thermalization. Amplitudes are represented in color (blue:low; red:high).

The obvious question is: what is the nature of the less-magnetic peaks? Is the cluster source operating in a bimodal way or are they in fact two distinct energy states? If by changing the thermalization condition, we only change the temperature of the cluster beam, we expect a shift of the peak distribution instead of the appearance of a well defined, second, less-magnetic peaks (see 4.1.2.2). In addition to that, the shift should vary continuously with the thermalization. These features are not observed. Hence the less-magnetic peak does not reflect the same beam at a different temperature. Thus it is not due to bimodal source

operation. Rather these peaks represent another state of the clusters. As shown in Figure 35, the more-magnetic peak is dominant when the thermalization is ideal. In a well thermalized cold beam (T = 20 K e.g.), clusters should be in their vibrational and electronic ground state (Appendix B). This suggests that the more-magnetic peaks correspond to clusters in their vibrational and electronic ground states (Co_N) and the less-magnetic peaks are in metastable excited states (Co_N^*).

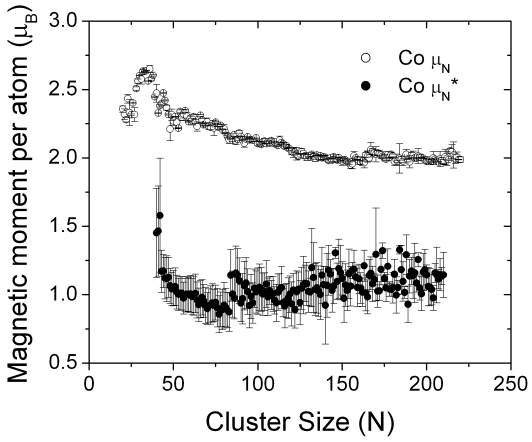

Figure 37: Magnetic moments per atom of Co_N clusters. Magnetic moments of ground state clusters are constant in the temperature range of the experiment(20 K $\leq T \leq$ 100 K). Magnetic moments of excited state clusters are field dependent. Magnetic moments of ground state(μ_N) and excited state(μ_N^*) Co_N clusters. μ_N^* were measured at B = 0.5 T and T = 30 K.

The magnetization of the excited states clusters (Co_N^*) in low fields is given by (40). At high field, deviations are seen. The magnetic moments found at low field μ_N^*/N converge to 1 μ_B (Figure 37). At high field, μ_N^*/N increases with the field. The high field magnetization anomaly of the excited states could be related to some coupling between the two states, as discussed in 5.2.4.

5.1.1.2 Photon heating

The nature of the excited state is revealed in photon heating experiments [162] [41] [61]. The cluster beam is illuminated by a light from 500 nm laser before it enters the inhomogeneous Stern-Gerlach magnetic field. The magnetization profiles are compared with those without

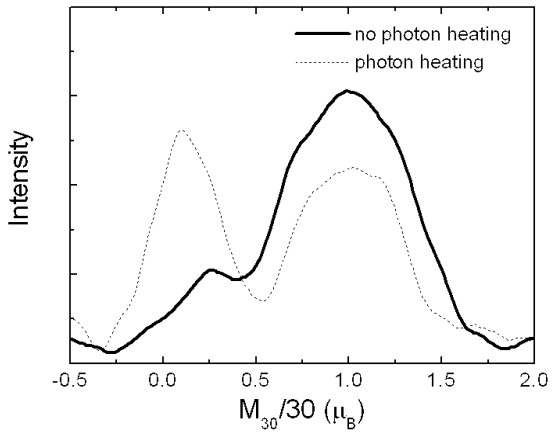

Figure 38: Magnetization distribution profiles of Co_{30} clusters in different conditions. Solid line is for good thermalization condition without laser heating; dashed line is for good thermalization condition, but the cluster beam is illuminated by a 500 nm laser before it enters the inhomogeneous magnetic field. $T = 30$ K and $B = 2$ T.

laser heating. Low fluence laser light is used. Note that the absorption of a photon does not significantly alter the rotational state, but it will increase the internal cluster energy.

We find that the laser heating has a similar effect to restricting the thermalization. It is clear from Figure 38 that much of the intensity of the magnetization distribution has been transferred from the more-magnetic peak to the less-magnetic peak when clusters are heated. This happens for all the clusters observed, as shown in Figure 39.

Now we have better idea of what these peaks in the magnetization distribution profile are: the more-magnetic peaks are from clusters in their ground states Co_N and the less-magnetic peaks are from clusters in their excited states Co_N^*.

5.1.1.3 Photo-ionization

Knowledge of the energy separation between the two states should help to understand the nature of the excitations. Therefore, the ionization potentials of cobalt clusters were measured from the photo-ionization efficiencies (PIE). The thermalization conditions were tuned to make either energy state dominant and the clusters were ionized by the tunable OPO laser. The number of clusters ionized and intensity of the OPO laser were recorded as the wavelength of OPO was scanned between 250 nm and 215 nm, and the ionization

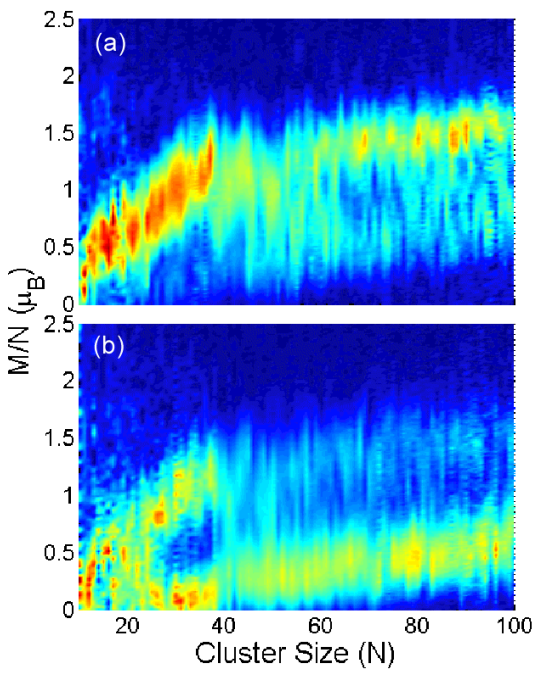

Figure 39: Magnetization distribution profiles of cobalt clusters (a) with and (b) without laser heating at $T = 30$ K, $B = 2$ T.

efficiencies were calculated as the number of ionized clusters divided by the intensity of the OPO laser.

Figure 40 shows the ionization potentials for the ground state (IP_N) and the excited state cobalt clusters (IP_N^*), which are consistent with previous measurements [193]. This confirms again that the more-magnetic peaks correspond to clusters in their ground states because those clusters have higher ionization potentials. Note that the energy separation between the ground states and the excited states are on the order of 0.1 eV for small clusters and vanish for larger clusters ($N > 100$). The quantitative values of the ionization potential differences indicate that the less-magnetic states are metastable electronically excited states.

5.1.1.4 Electric deflections

To further probe the electronic structure difference between the two states, the polarizabilities of cobalt clusters were studied. The collimated cluster beam (0.1 mm $\times$5 mm slit) was deflected in an inhomogeneous electric field ($0 \leq E \leq 80$ kV/cm; $dE/dz = 400E$ kV/cm^2) [129], and the polarizabilities (α) were calculated from the deflection (δ) using (48). The

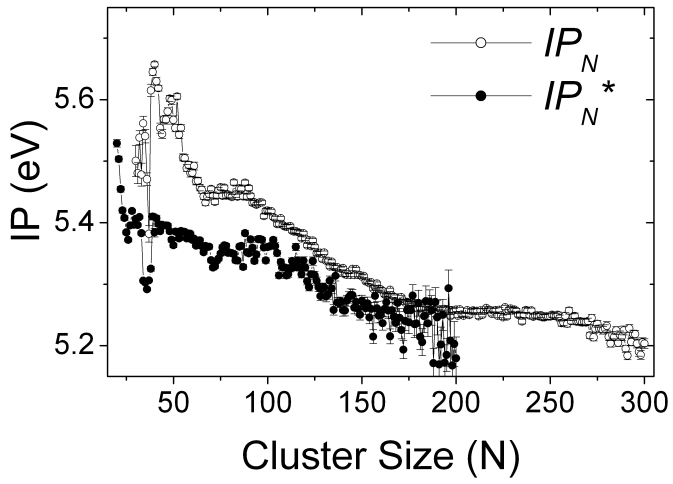

Figure 40: Photo-ionization potentials of cobalt clusters at $B = 0$ T and $T = 30$ K.

results are astonishing. The excited states have lower polarizability than the ground states (Figure 41). Polarizability is closely related to the volume of the mobile electronic cloud [41]. One expects a higher mobility for the excited states, corresponding to a larger polarizability, which contradicts the experimental results. In contrast to the excited states, the polarizability of the ground states has a rich structure in its size dependence.

5.1.2 Iron clusters

If the two states with quantized magnetic moments per atom are the common feature of ferromagnetic clusters, we should see this phenomenon for other ferromagnetic clusters, like iron and nickel clusters. However, the deflection experiment is complicated for the clusters with more than one isotope, because of the molecular beam method we use here. That is why cobalt clusters have been extensively studied. We next carried out magnetic and electric deflection experiments on iron clusters using isotopically pure ^{56}Fe.

5.1.2.1 Magnetic deflections

Figure 42 shows the magnetization distribution profiles for iron clusters under different thermalization conditions. Strikingly, for iron clusters, we found the same phenomenon as we did for cobalt clusters. Under good thermalization conditions, the more-magnetic

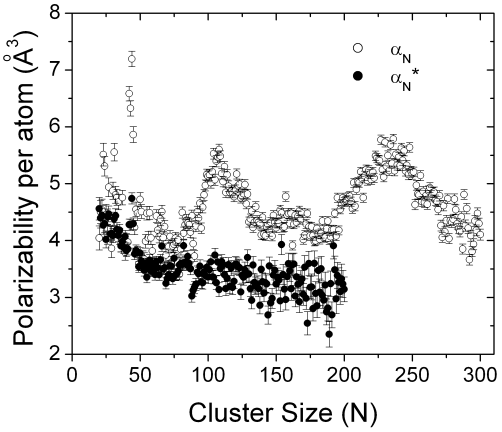

Figure 41: Polarizabilities per atom of cobalt clusters at $T = 20$ K. Ground state polarizabilities (α_N) are higher than excited state polarizabilities (α_N^*) because their electronic structure comprises more $4s$ electrons that are more dispersed in space. Fitting by jellium model, $\alpha = (r_s + \frac{\delta_s}{N^{1/3}})^3 N$, gives $\delta_s = 1.1$ $\mathring{A}$ for the ground state and $\delta_s = 0.7$ $\mathring{A}$ for the excited state.

clusters are dominant. When the thermalization condition is restricted, the less-magnetic peaks emerge. As for cobalt, the proportion of the two peaks in the beam profile changes continuously with the thermalization condition but the positions of the two peaks basically stay the same.

Similar to cobalt clusters, these two peaks represent two microscopic states for iron clusters. The more-magnetic peaks are the ground state Fe_N because they persist for good thermalization. The less-magnetic peaks are the excited states Fe_N^*. We can use the same analysis as we did for cobalt and the magnetic moments. The magnetic moments we have found for iron clusters are again quantized. The magnetic moments for the ground state clusters (μ_N) are around 3 μ_B per atom. And again the magnetic moments for the excited states are field dependent. At low field, μ_N^* converges to 1 μ_B per atom. Note that the magnetic moment per atom found here is again quantized (3 μ_B and 1 μ_B), similar to cobalt (2 μ_B and 1 μ_B). The fractional magnetic moments per atom for bulk (cobalt:1.7 μ_B; iron: 2.1 μ_B) fall in the quantized values found in the beam.

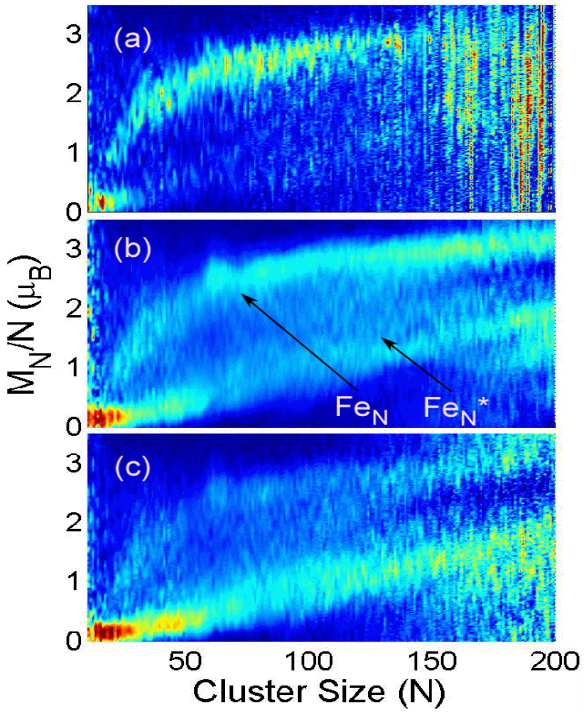

Figure 42: The normalized magnetization probability distribution of Fe_N ($10 \leq N \leq 200$, $T = 20$ K). (a) Ideal thermalization, $B = 1.3$ T. (b) Intermediate thermalization, $B = 1.2$ T. (c) Restricted thermalization, $B = 1.2$ T. Amplitudes are represented in color (blue:low; red:high).

5.1.2.2 Electric deflections

Electric deflection experiments have been done on iron clusters as well. The results are different from those from cobalt clusters. The polarizabilities of the two states are shown in Figure 44. The ground states and the excited states have virtually the same polarizability. Besides that, neither Fe_N nor Fe_N^* show strong oscillations when the cluster size is changed. The polarizability decreases monotonically with size.

5.1.3 Manganese clusters

Bulk manganese is antiferromagnetic while some manganese clusters show ferromagnetic behavior [89].

Since we have found two states for both cobalt and iron, and manganese is right next to them in the periodic table. It makes sense to study manganese clusters.

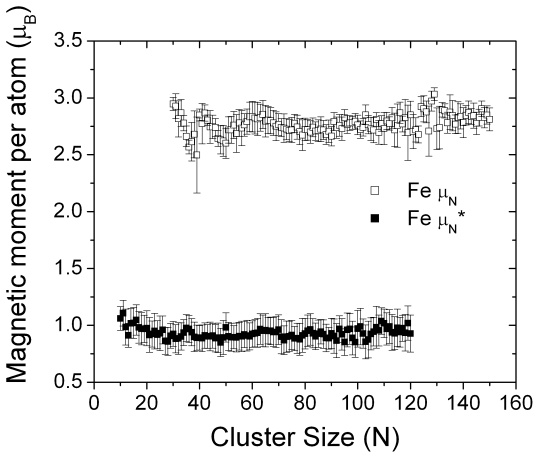

Figure 43: Magnetic moments per atom of Fe_N clusters. Magnetic moments of excited state clusters are field dependent. μ_N^* were measured at $B = 1.0$ T and $T = 20$ K.

The results for manganese clusters are shown in Figure 45. From Figure 45a, one can see that for some clusters ($N \sim 60$ and $N > 120$), there appear to be very broad peaks that resemble two peaks. Because the magnetic moments of manganese clusters are not as high as cobalt and iron clusters, we cannot find the magnetic moments from the saturation magnetization. If we convert the vertical scale of Figure 45a from magnetization M into magnetic moment μ assuming (39), one obtains Figure 45b. The figure shows two branches of manganese clusters. The one with smaller magnetic moment was observed earlier by Knickelbein [89]. The one with larger magnetic moment is only observed for certain cluster sizes, but strikingly, the magnetic moments are very close to 1 μ_B per atom. Again, the magnetic moments are quantized.

5.1.4 Cobalt manganese cluster

Alloy clusters have been an important subject in cluster physics [70] [150] [203]. How the properties of alloys evolve with size is intriguing. In addition to that, using a small amount of impurity as a probe to examine the properties of the host cluster is also interesting, especially given that we can know precisely how many impurity atoms we have in the clusters. We added manganese impurity atoms into host cobalt clusters to see how the two states behave.

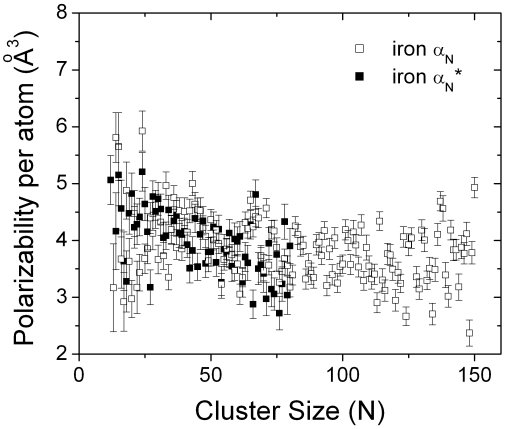

Figure 44: Polarizabilities per atom of iron clusters at $T = 20$ K. Ground state polarizabilities (α_N) are similar to excited state polarizabilities (α_N^*). Fitting by jellium model, $\alpha = (r_s + \frac{\delta_s}{N^{1/3}})^3 N$, gives $\delta_s = 0.6$ $\AA$.

A sample rod with 15% manganese and 85% cobalt was used in the experiment. As shown in Figure 46, the mass peaks follow a binomial distribution consistent with the mass ratio of the sample rod. Apparently, the two peaks feature persists even when manganese atoms replace some cobalt atoms.

The ground state has been studied carefully, showing that every manganese atom enhances the magnetic moment of the cluster by 1.7 μ_B [196], suggesting that the impurity energy level is close to the host's band structure. The enhancement comes from the deficiency of $3d$ electron of manganese atom. Therefore the impurity does not alter the band structure of the host very much. The existence of the two states in the cobalt manganese alloy clusters that have a similar band structure as the cobalt cluster suggests that the two states are a property of the global electronic structure of the cluster.

5.1.5 Possibility of structure isomers

It has been discussed above that the two populations observed are two electronic states from the energy point of view. Actually, the bulk properties of cobalt and iron show that the structures are not closely related to magnetism, at least not to an extent that is observed here.

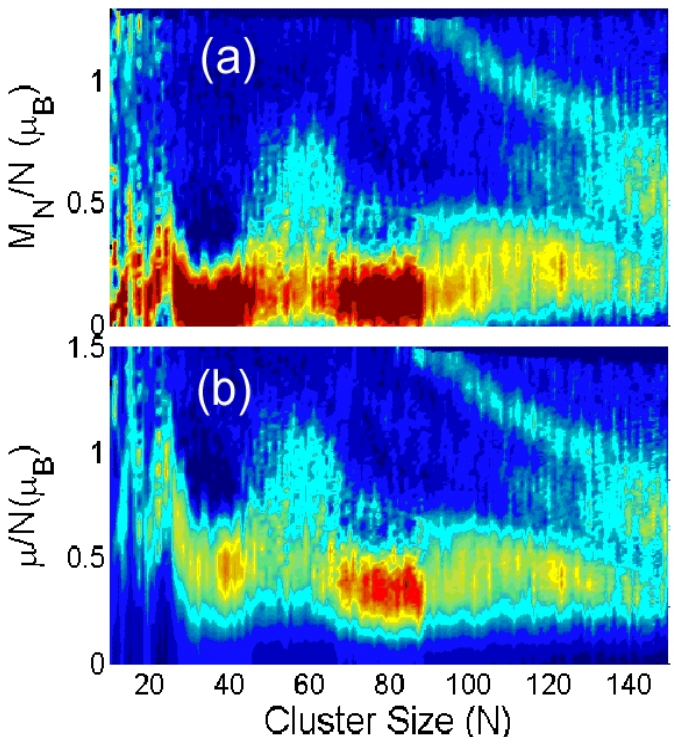

Figure 45: Magnetizations (a) and magnetic moments (b) per atom for manganese clusters. Note that for cluster size $N \sim 60$ and $N > 120$, a second state that has 1 μB per atom is observed.

For bulk iron, there are two possible structures, bcc ($T < 900$ K and $T > 1400$ K) and fcc (900 K $< T <$ 1400 K). Because bcc is not close-packed structure, the phase change of structure will cause a significant change of density. However, experiments show no evidence of saturation magnetization change related to the structural change at temperature around 900 K [189]. For bulk cobalt, the two phases are hcp ($T <$ 430 K) and fcc ($T >$ 430 K). They are both close-packed structures, so the density change is not so much. While most experimental groups report no correlation between structure change and saturation magnetization, one group did see such effect at around 400 K. But the change is only 1.5% [189].

As mentioned in 2.2.2.2, structures of ferromagnetic clusters are intriguing from both experimental and theoretical point of views. However, so far our knowledge of cluster structures is very limited. Experiments show the tendency of icosahedral structure for ferromagnetic clusters, which is confirmed by theoretical work. However, theoretical calculation also

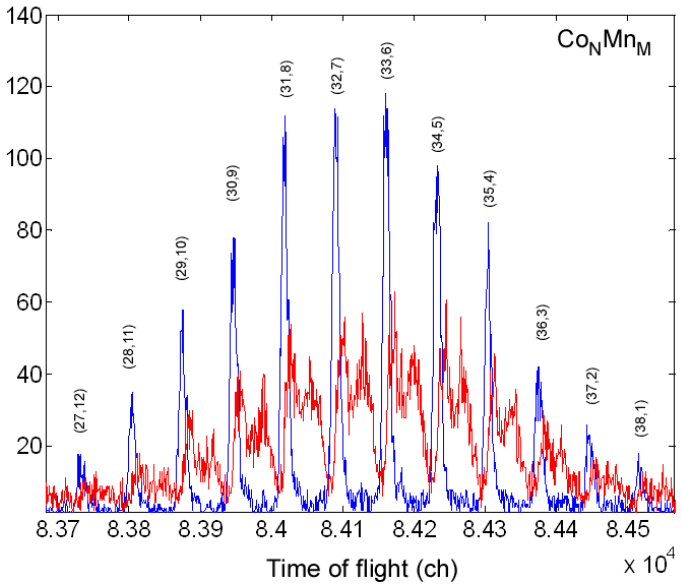

Figure 46: Mass spectrum of $Co_N Mn_M$ clusters for which $N + M = 39$. The intensities of the mass peaks follow the binomial distribution. Every individual peak is identified and marked with (N, M). The blue curve is the spectrum with magnetic field $B = 0$, while the red curve is the spectrum with magnetic field $B = 2$ T. The thermalization condition was tuned intermediate.

found many isomers with energies very close to the ground-state energy. The existence of two structures of cobalt and iron clusters over such a large size range ($20 \leq N \leq 200$) has never been predicted.

5.2 Theory

5.2.1 Electronic configurations

Free iron group metal atoms always have two $4s$ electrons. The electronic configurations for free iron and cobalt atoms are $3d_{\uparrow}^5 3d_{\downarrow}^1 4s^2$ and $3d_{\uparrow}^5 3d_{\downarrow}^2 4s^2$ respectively [170]. When atoms come together in clusters, the $4s$ electrons tend to form a free-electron-like $4s$ band. Electrons overflow from $4s$ band into $3d$ orbitals to reduce the total energy. So we expect the ground state electronic configurations for Fe_N and Co_N to be $3d_{\uparrow}^5 3d_{\downarrow}^2 4s^1$ and $3d_{\uparrow}^5 3d_{\downarrow}^3 4s^1$ respectively. While $4s$ electrons become itinerant, $3d$ electrons are more localized. Even in bulk, not all the $3d$ electrons are itinerant [168]. Actually the $3d$ electrons are more localized in clusters [60] [126] than in the bulk for two reasons: First, due to the reduced

coordination, the width of the tight-binding band width will be reduced [21]. Second, the loss of translation symmetry creates the disorder that will localize the $3d$ electrons [4] [1].

As we know, $4s$ electrons are not magnetically polarized and the orbital angular momenta are quenched due to the crystal field (1.2.3.1) [64]. Based on these arguments, Hund's rule predicts the magnetic moment per atom to be $3\mu B$ and $2\mu B$ for Fe_N and Co_N respectively, according to their electronic configurations. These values are reasonably close to the experimental observations [21] [192] [30] [49]. We can also write down the electronic configuration of the excited states Fe_N^* and Co_N^* observed in experiments from their magnetic moments, say $3d_\uparrow^4 3d_\downarrow^3 4s^1$ and $3d_\uparrow^5 3d_\downarrow^4 4s^0$ respectively.

Other measured properties support these proposed electronic configurations. For example, magic numbers in the IPs and polarizabilities of Co_N both suggest an electronic shell structure that can only come from the loosely bonded s electrons. According to the electronic configuration $3d_\uparrow^5 3d_\downarrow^3 4s^1$, in Co_N every cobalt atom contributes one $4s$ electron that is delocalized over the whole cluster and promotes the shell structure. In contrast, Co_N^* has no $4s$ electrons in the electronic configuration $3d_\uparrow^5 3d_\downarrow^4 4s^0$, which agrees with the fact that both IP and polarizabilities of Co_N^* almost monotonically decrease with increasing size. In addition, the fact that there are more $4s$ electrons in Co_N than in Co_N^* explains why α_N are systematically larger than α_N^* for cobalt clusters. For iron clusters, the polarizabilities of Fe_N are very similar to those of Fe_N^*, which is consistent with the proposed electronic configurations because Fe_N and Fe_N^* have similar $4s$ electron populations.

5.2.2 Cobalt clusters

5.2.2.1 Falicov-Kimball model

To understand the two states found for the cobalt clusters, one needs to consider the interaction between the $3d$ and $4s$ electrons. As shown by Appendix D, the Falicov-Kimball model describes this interaction. In this model, the total energy can be written as

$$E_t = \varepsilon_s N_s + \frac{W}{2N} N_s^2 + \varepsilon_d N_d + \frac{G}{2N} N_s N_d,$$

where N_s and N_d are the number of electrons in the $4s$ band and highest $3d$ orbitals, ϵ_d is the single electron energy of the highest $3d$ orbital, ϵ_s is the electron energy at the bottom

of the $4s$ kind band, W is the effective width of the $4s$ and G is the intra-atomic repulsion between the $4s$ and $3d$ electrons.

The total number of electrons in the $4s$ band and the $3d$ orbitals is constant: $N{=}N_s{+}N_d$. Hence the energy of a system with N_s electrons in the $4s$ band is

$$E_t(N_s) = -(G - W/2)N_s^2/N + (G - \varepsilon_d + \varepsilon_s)N_s + N\varepsilon_d, \tag{58}$$

which is a parabola with respect to N_s, as shown in Figure 47. Because $0 \leq N_s \leq N$ the parabola has two minima at the two limits. They are $E_t(N_s = 0) = N\varepsilon_d$ and $E_t(N_s = N) = NW/2 + N\varepsilon_s$. The vertex of the parabola is maximum at $N_s^{\max} = N/2 - (W - 2\varepsilon_d + 2\varepsilon_s)/(4G - 2W)N$, with energy $E^{max} = (G - \varepsilon_d + \varepsilon_s)^2/(4G - 2W)N + N\varepsilon_d$.

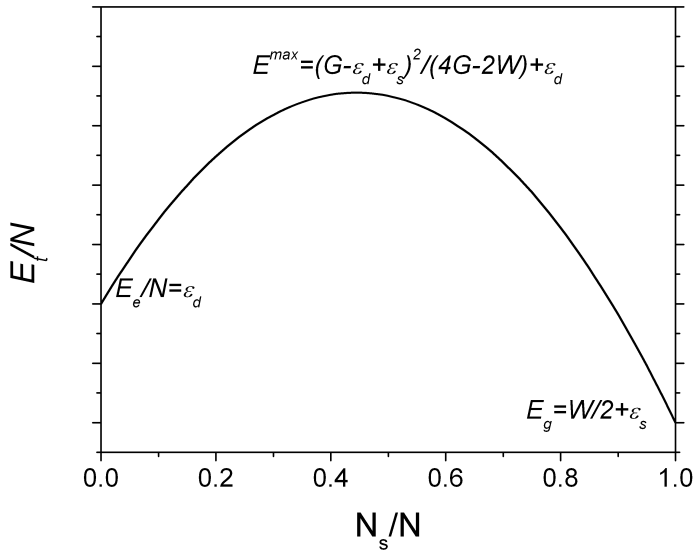

Figure 47: Total energy predicted by the Falicov-Kimball model. The picture explains the existence of two states of with local minimum energy: One is the ground state, the other is the metastable excited state.

5.2.2.2 The two states

As shown in Figure 47, the two minima correspond to the two states observed in the experiment: One of them is the ground state, the other is the metastable excited state. In the case of small clusters, the band width is not as large as that in bulk, therefore $W/2 < \varepsilon_d - \varepsilon_s$. Hence the ground state corresponds to $N_s = N$ with energy $E_g = NW/2 + N\varepsilon_s$,

which for cobalt corresponds to the electronic configuration $3d^5_\uparrow 3d^3_\downarrow 4s^1$. The excited state corresponds to $N_s = 0$ with energy $E_e = N\varepsilon_d$, which for cobalt is the electronic configuration $3d^5_\uparrow 3d^4_\downarrow 4s^0$.

5.2.2.3 The metastable excited state

The fact that two minima are separated by an energy barrier explains why the excited state is metastable. In an interaction with the environment the lifetime of this state can be very long. Apparently it can survive the transition from source to detector ($\sim 1ms$).

5.2.2.4 Size effect

The size effect is discussed based on the model. When the cluster size increases, the number of electrons on the cluster surface decreases. When the surface becomes less important, the electron density increases, because the electrons on the surface are less congested. Therefore the Fermi energy becomes larger for the $4s$ electrons, resulting in a larger band width W. The energy difference between the two states $E_e - E_g = (\varepsilon_d - \varepsilon_s - W/2)N$ then reduces. For a certain cluster size, the two states will be degenerate in energy.

When the cluster size increases, the $4s$ electrons are more confined in the interior, which makes the interaction between $4s$ and $3d$ electrons G stronger.

The band width of the $4s$ electron is assumed to be roughly proportional to the Fermi energy of an free electron gas. In terms of the electron spillout δ_s and the classical radius of the cluster R, the band width is $W \propto (1 - 2\delta_s/R)$, given that $\delta_s \ll R$. The Coulomb repulsion between the $4s$ and the $3d$ electrons G also increases with cluster size, although the dependence on the cluster radius is not easy to estimate. However, the effective single electron energies ε_d and ε_s are more or less constant. Hence, the energy barrier decreases when the cluster size increases, which explains the closing of the energy gap between the two states observed in the IP experiments.

5.2.3 Iron clusters

If we apply the same theory to iron clusters, we get two states with magnetic moments $3\mu B$ per atom and $2\mu B$ per atom instead of the observed $3\mu B$ and $1\mu B$ per atom. The

polarizability data also do not show significant differences between Fe_N and Fe_N^*, nor magic numbers either.

However, if we assume that the interaction is between localized and itinerant $3d$ electrons, the experimental data can be explained. Because iron has more than half filled $3d$ orbitals, exchanging electrons between different orbitals will result in a change of $2\mu B$ per atom. In these two states, the electron population in the $4s$ bands are the same. Therefore the polarizabilities should be rather similar.

5.2.4 Coupling between the two states

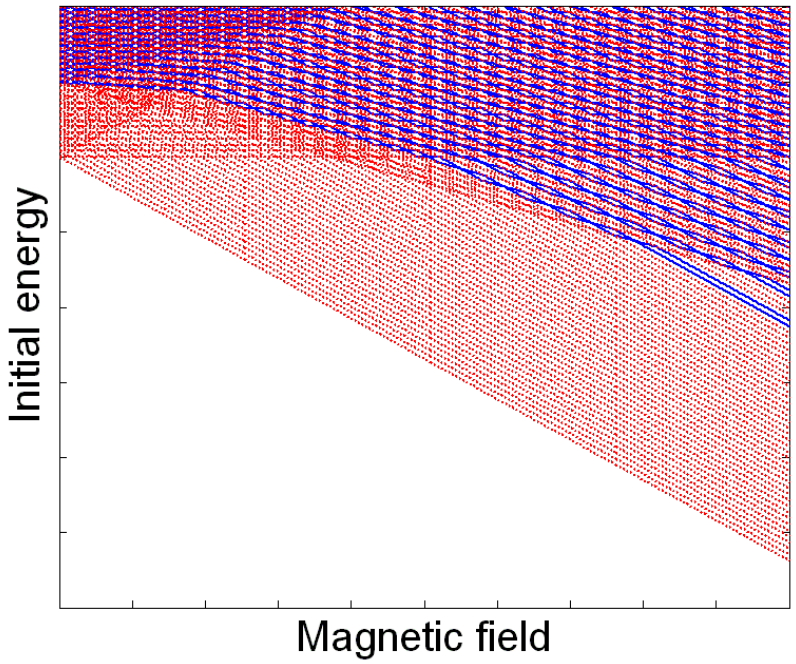

Figure 48: Schematic energy diagram of cobalt clusters with two states assuming all crossing between energy levels are avoided. The dashed red lines are the energy levels starting from the ground spin state (e.g., Co_N). The solid blue lines are the energy levels starting from the excited spin state (e.g., Co_N^*). At a large enough field, all energy levels tend to have magnetization μ_N.

The magnetic moment of cobalt and iron clusters are found from their low-field magnetization because at low field, the clusters in the two states follow (40). However, at high field, the magnetization of the excited state converges to that of the ground state, which

suggests some coupling between the two states.

It is possible to understand this using the avoided crossing theory. If there is some coupling between the two states (Co_N and Co_N^*), the crossings between the energy levels of the two states can be avoided. The effect of the magnetic field can be depicted using the Zeeman diagram (Figure 48). The clusters start from their various rotational, vibration and electronic levels outside the magnetic field. When they enter the magnetic field, the additional Zeeman energy will mix levels with different initial states. In most cases, the crossings between cluster levels are avoided. The adiabatic energy levels zigzag with increasing magnetic field, but the overall trend is a monotonic enhancement of the magnetization. For large magnetic fields, the magnetization will converge to the magnetization behavior of the lowest level, which is μ_N.

5.2.5 Narrow-band phenomenon

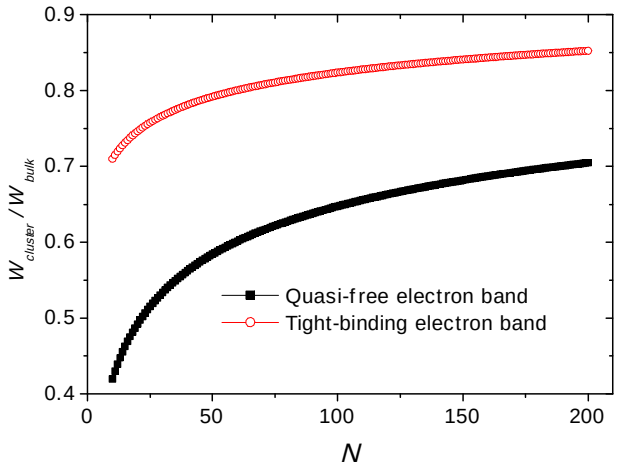

Figure 49: Estimated band width of cobalt clusters as a function cluster size, normalized to the resepctive bulk limit. The electronic spillout $\delta_{spillout}$ is taken to be $1.0\mathring{A}$. An atom on the surface is assumed to have half the neighbours of an interior atom.

In Falicov-Kimball mode (58), $G > W/2$ is required in order to predict two energy minima separated by a barrier, indicating that this is a narrow-band phenomenon (NBP) [59] [139]. For a well-delocalized electron system, the band width is normally very large,

while for well-localized electrons the language of an energy band is not appropriate any more. Narrow-band case stands in between these two limits. NBP has been an important issue for a long time in the bulk material [59] [139]. A lot of interesting physical properties come from narrow bands, for example valence mixing [63], which occurs when the electron energy band at the Fermi energy is narrow. In bulk, the band width varies with the itinerancy of electrons. Normally, the itinerancy is sorted as $4f < 5f < 3d < 4d < 5d$ [166]. Therefore, NBP exists for certain materials. Here we show another aspect: NBP emerges for certain sizes.

The band width of clusters is reduced compared to the bulk limit for both quasi-free electrons and tight-binding electrons. The density of a quasi-free-electron cloud is lower in a cluster than that in the bulk because of the electronic spillout $\delta_{spillout}$. The less congested electrons result in reduced quasi-free-electron band width, as shown in Figure 49. For tightly bound electrons, the band width is proportional to the overlap of the neighbouring atoms and the number of neighbours. In clusters, since there are many atoms on the surface with fewer neighbors, the band width will also be reduced (Figure 49).

5.2.6 From atom to the bulk

Free atoms of iron group metals are better understood than clusters and the bulk. Electrons occupy single electron orbitals from low energy to high energy. Although $4s$ orbital is supposed to be higher than $3d$, the real case is the opposite when electrons from the inner shell are considered. Therefore, the effective single electron energy ε_d is greater than ε_s, as shown in Figure 50.

When atoms come together, both $4s$ and $3d$ electrons tend to form energy bands, but in very different ways. The $4s$ electrons are more free-electron like, and the width of the band depends on Fermi energy of the quai-free electrons. The $3d$ electrons are more tightly bound to the ion cores, the band width depends on the overlapping of electron cloud from the neighboring atoms and the coordination. The evolution of physical properties from atom to bulk is closely related to the evolution of the band structures.

Clusters are in between free atoms and the bulk. They have narrow bands. We have

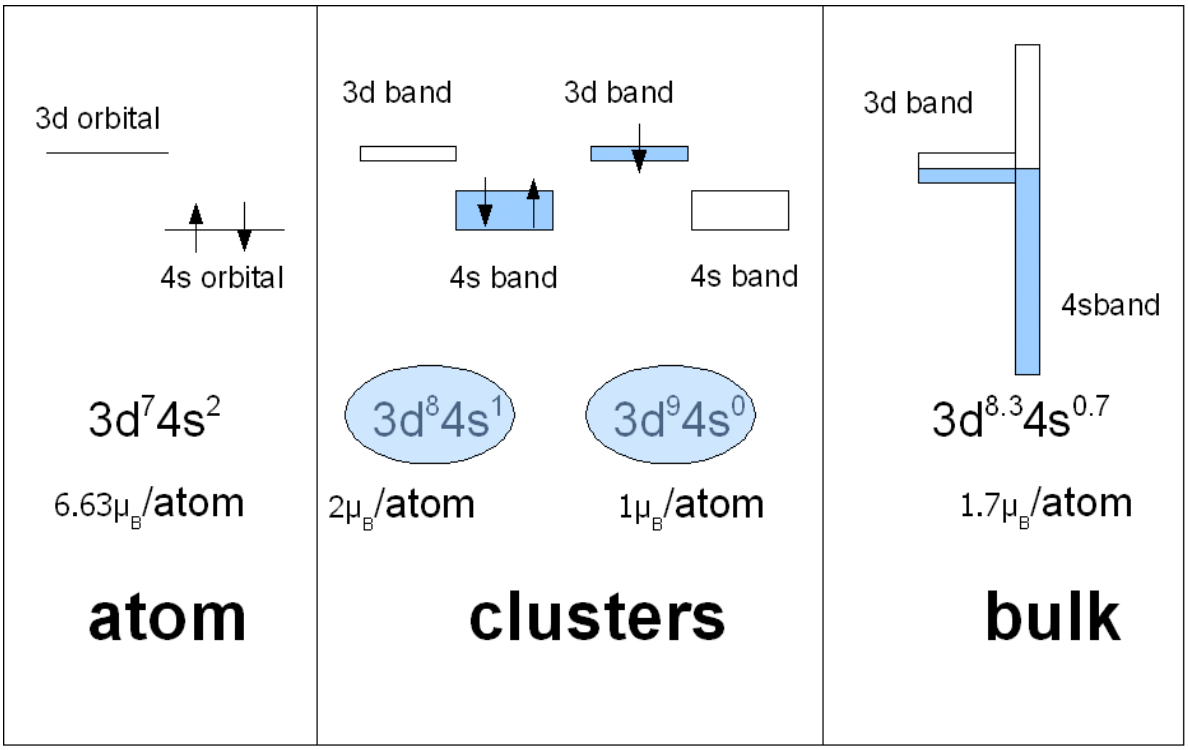

Figure 50: The energy diagram of cobalt from free atom to the bulk.

shown that the Falicov-Kimball model works very well in explaining novel properties of ferromagnetic clusters. The size effect of cluster properties was also discussed. One of the major reasons we wanted to study the ferromagnetic clusters was to see how their properties evolve in size and to get a complete picture of the physics. We have shown the existence of the two states separated by an energy barrier, and the merging of the two states in energy when the cluster size becomes large. The question is: are those two states with quantized magnetic moments unique in clusters or do they actually remain in bulk in a different form?

The Falicov-Kimball model predicts two states and an energy barrier for small clusters. The energy difference decrease with increasing size is also predicted by the model. The behavior of the energy gap is more complicated. As the size of the cluster becomes larger and eventually approaches bulk limit, there can be two possibilities.

The first possibility is that the picture of the two states separated by an energy barrier persists, but the two states become degenerate in energy. The energy barrier also can be much lower in bulk. In this case, the bulk actually fluctuates between the two states, causing

the average magnetic moment a fractional number between the quantized numbers. We can easily estimate the average magnetic moment weighted by the spin degeneracy. For cobalt $< \mu_{Co} >= \frac{2\mu_B(2N+1)+1\mu_B(N+1)}{(2N+1)+(N+1)} \approx 1.7\mu_B$, and for iron $< \mu_{Fe} >= \frac{3\mu_B(3N+1)+1\mu_B(N+1)}{(3N+1)+(N+1)} \approx 2.5\mu_B$ for large N. Both are very close to their bulk value. This is actually another way to describe itinerant ferromagnetism and explain fractional magnetic moment per atom.

The second possibility is that the energy maximum between the two states actually becomes a minimum. In this case, the two states eventually evolve into one state with a fractional number of magnetic moments per atom. This is more like the picture of Stoner's model [188].

CHAPTER VI

CONCLUSION

Magnetic deflections of cobalt clusters Co_N are carefully studied. It is shown that even at very low temperature ($T = 20$ K) and for small sizes ($N = 10$), the magnetization of cobalt clusters closely follows the Langevin function. This is explained by the avoided crossing model assuming adiabatic processes when the clusters pass through the inhomogeneous magnetic field. The apparent relaxation of the magnetization of clusters results from the evolution of adiabatic energy levels rather than from simple energy exchange with a heat bath.

Two states (a ground state and a metastable excited state), both with quantized magnetic moments per atom, have been found for cobalt and iron clusters. The spin weighted average magnetic moments of the two states are very close to the bulk value. The energy difference of the two states decreases with increasing cluster size. The observations can be understood in the Falicov-Kimball model, which predicts the existence of two states separated by an energy barrier. The fact that the two states become close in energy at large sizes and that the average magnetic moments are close to bulk value suggests that the fractional magnetic moment in the bulk may come from a fluctuating ground state.

APPENDIX A

TWO-ELECTRON MODEL

Magnetism is a complicated many-body problem, even for a system of very small size. Among many different magnetic systems, metallic ferromagnets are no doubt the most intractable. We hereby will study the simplest system (two electron problem), which already contains crucial ingredients for larger systems.

A.1 Homopolar Molecule - a Test for various exchange interaction models

A homopolar molecule consists of two identical nuclei and two electrons. It is like hydrogen molecule, but we treat the system as a fictitious one for which we can vary parameters and change the magnetic order. Using the Born-Oppenheimer approximation [117], the Hamiltonian in this case can be solved exactly. We will also apply Stoner [188] and Hubbard [74] model to this problem and compare their results with the exact solution.

A.1.1 Original Hamiltonian and exact solution

The full Hamiltonian is

$$H = \frac{p_1^2}{2m_e} + \frac{p_2^2}{2m_e} + \frac{e^2}{4\pi\epsilon_0}(-\frac{1}{r_{1A}} - \frac{1}{r_{2A}} - \frac{1}{r_{1B}} - \frac{1}{r_{2B}} + \frac{1}{r_{12}}), \tag{59}$$

where 1 and 2 are two electrons, A and B are two nuclei.

Approximation 1 *The two nuclei are assumed fixed in space, which is Born-Oppenheimer approximation.*

For simplicity, we can let $\frac{e^2}{4\pi\epsilon_0}$ be unity. One can always regroup the Hamiltonian as

$$H = H_1 + H_2 + H_{12},$$

where

$$\begin{aligned} H_1 &= \frac{p_1^2}{2m_e} - \frac{1}{r_{1A}} - \frac{1}{r_{1B}} \\ H_2 &= \frac{p_2^2}{2m_e} - \frac{1}{r_{2A}} - \frac{1}{r_{2B}} \\ H_{12} &= \frac{1}{r_{12}}. \end{aligned}$$

In fact, H_1 and H_2 are identical single electron Hamiltonian except for the coordinates. To solve this single electron Hamiltonian, we can start from the eigenstates of atomic Hamiltonian $H_{atom} = \frac{p_1^2}{2m_e} - \frac{1}{r_{1A}}$ as basis, diagonalize H_1 to get the solution.

Approximation 2 *For simplicity, we have to make the second approximation to only consider the lowest eigenstates of the atomic Hamiltonian, say, $\phi_A(r_1)$ which represents the lowest atomic eigenstates (atomic orbital) surrounding nucleus A occupied by electron* 1*. This can be considered as single band model.*

Using second quantization representation, we can rewrite the Hamiltonian:

$$H = \epsilon \sum_{i,\sigma} C_{i\sigma}^+ C_{i\sigma} + t \sum_{i \neq j,\sigma} C_{i\sigma}^+ C_{j\sigma} + \frac{1}{2} \sum_{ijkl,\sigma\sigma'} U_{ijkl} C_{i\sigma}^+ C_{j\sigma'}^+ C_{k\sigma'} C_{l\sigma},$$

where $i = A, B$ and the parameters are defined as following

$$\begin{aligned} \epsilon &\equiv \langle \phi_A(r_1) | \frac{p_1^2}{2m_e} - \frac{1}{r_{1A}} - \frac{1}{r_{1B}} | \phi_A(r_1) \rangle \\ t &\equiv \langle \phi_B(r_1) | - \frac{1}{r_{1B}} | \phi_A(r_1) \rangle \\ U_{ijkl} &\equiv \langle \phi_i(r_2) | \langle \phi_i(r_1) | \frac{1}{r_{12}} | \phi_k(r_1) \rangle | \phi_l(r_2) \rangle . \end{aligned}$$

The two body term $\frac{1}{2} \sum_{ijkl,\sigma\sigma'} U_{ijkl} C_{i\sigma}^+ C_{j\sigma'}^+ C_{k\sigma'} C_{l\sigma}$ should be addressed carefully here, because it involves many different type of integrals, which include

$$\begin{aligned} u &\equiv U_{AAAA} \\ v &\equiv U_{ABBA} = U_{BAAB} \\ J &\equiv U_{ABAB} = U_{BABA} \\ p &\equiv U_{ABBB} = U_{BAAA} \\ q &\equiv U_{AABB} = U_{BBAA}. \end{aligned}$$

Using the second quantization basis

$$\begin{aligned}
\mathbf{e}_1 &\equiv |\uparrow_A\uparrow_B\rangle \\
\mathbf{e}_2 &\equiv |\downarrow_A\downarrow_B\rangle \\
\mathbf{e}_3 &\equiv |\uparrow_A\downarrow_A\rangle \\
\mathbf{e}_4 &\equiv |\uparrow_A\downarrow_B\rangle \\
\mathbf{e}_5 &\equiv |\downarrow_A\uparrow_B\rangle \\
\mathbf{e}_6 &\equiv |\uparrow_B\downarrow_B\rangle ,
\end{aligned}$$

we can write down the matrix elements of the Hamiltonian.

Approximation 3 *As a matter of fact, because the overlap integral* $\langle\phi_B(r_1)|\,\phi_A(r_1)\rangle$ *is not necessarily zero, the assumption that the six basis are orthorgonal is the third approximation we make here.* [176]

An important observation is that the 6 dimension space can be reduced to 3 subspaces which do not mix with each other. The first two subspaces are one dimensional, including $\mathbf{e}_1$ ($S_z = 1$) and $\mathbf{e}_2$ ($S_z = -1$) respectively. The third subspace consists $\mathbf{e}_3$ through $\mathbf{e}_6$ ($S_z = 0$). It is straightforward however tedious to calculate the matrix elements. We hereby will show a few examples.

$$\begin{aligned}
\langle\mathbf{e}_1|\,H\,|\mathbf{e}_1\rangle &= \langle\uparrow_B\uparrow_A|\,\epsilon\sum_{i,\sigma}C^+_{i\sigma}C_{i\sigma} + t\sum_{i\neq j,\sigma}C^+_{i\sigma}C_{j\sigma} + \frac{1}{2}\sum_{ijkl,\sigma\sigma'}U_{ijkl}C^+_{i\sigma}C^+_{j\sigma'}C_{k\sigma'}C_{l\sigma}\,|\uparrow_A\uparrow_B\rangle \\
&= 2\epsilon_B\,\langle\uparrow_B\uparrow_A|\,|\uparrow_A\uparrow_B\rangle \\
&\quad +\frac{1}{2}_B\,\langle\uparrow_B\uparrow_A|\,U_{ABBA}C^+_{A\uparrow}C^+_{B\uparrow}C_{B\uparrow}C_{A\uparrow} + U_{BAAB}C^+_{B\uparrow}C^+_{A\uparrow}C_{A\uparrow}C_{B\uparrow} \\
&\quad +U_{ABAB}C^+_{A\uparrow}C^+_{B\uparrow}C_{A\uparrow}C_{B\uparrow} + U_{BABA}C^+_{B\uparrow}C^+_{A\uparrow}C_{B\uparrow}C_{A\uparrow}\,|\uparrow_A\uparrow_B\rangle \\
&= 2\epsilon + \frac{1}{2}(U_{ABBA} + U_{BAAB}) - \frac{1}{2}(U_{ABAB} + U_{BABA}) \\
&= 2\epsilon + v - J.
\end{aligned}$$

$$\begin{aligned}
\langle \mathbf{e}_3 | H | \mathbf{e}_3 \rangle &= \langle \downarrow_A \uparrow_A | \epsilon \sum_{i,\sigma} C^+_{i\sigma} C_{i\sigma} + t \sum_{i \neq j,\sigma} C^+_{i\sigma} C_{j\sigma} + \frac{1}{2} \sum_{ijkl,\sigma\sigma'} U_{ijkl} C^+_{i\sigma} C^+_{j\sigma'} C_{k\sigma'} C_{l\sigma} | \uparrow_A \downarrow_A \rangle \\
&= 2\epsilon + \frac{1}{2}(U_{AAAA} + U_{AAAA}) \\
&= 2\epsilon + u.
\end{aligned}$$

$$\begin{aligned}
\langle \mathbf{e}_4 | H | \mathbf{e}_4 \rangle &= \langle \downarrow_B \uparrow_A | \epsilon \sum_{i,\sigma} C^+_{i\sigma} C_{i\sigma} + t \sum_{i \neq j,\sigma} C^+_{i\sigma} C_{j\sigma} + \frac{1}{2} \sum_{ijkl,\sigma\sigma'} U_{ijkl} C^+_{i\sigma} C^+_{j\sigma'} C_{k\sigma'} C_{l\sigma} | \uparrow_A \downarrow_B \rangle \\
&= 2\epsilon + \frac{1}{2}(U_{ABBA} + U_{BAAB}) \\
&= 2\epsilon + v.
\end{aligned}$$

$$\begin{aligned}
\langle \mathbf{e}_4 | H | \mathbf{e}_5 \rangle &= \langle \uparrow_B \downarrow_A | \epsilon \sum_{i,\sigma} C^+_{i\sigma} C_{i\sigma} + t \sum_{i \neq j,\sigma} C^+_{i\sigma} C_{j\sigma} + \frac{1}{2} \sum_{ijkl,\sigma\sigma'} U_{ijkl} C^+_{i\sigma} C^+_{j\sigma'} C_{k\sigma'} C_{l\sigma} | \uparrow_A \downarrow_B \rangle \\
&= -\frac{1}{2}(U_{ABAB} + U_{BABA}) \\
&= -J.
\end{aligned}$$

Then the matrix of the Hamiltonian is

$$\begin{bmatrix}
v-J & 0 & 0 & 0 & 0 & 0 \\
0 & v-J & 0 & 0 & 0 & 0 \\
0 & 0 & u & t+p & -t-p & q \\
0 & 0 & t+p & v & -J & t+p \\
0 & 0 & -t-p & -J & v & -t-p \\
0 & 0 & q & t+p & -t-p & u
\end{bmatrix}, \tag{60}$$

where the constant 2ϵ for every diagonal element is abbreviated for simplicity. If we only consider the subspace $\mathbf{e}_3$ through $\mathbf{e}_6$, the Hamiltonian is reduced to:

$$\begin{bmatrix}
u & t+p & -t-p & q \\
t+p & v & -J & t+p \\
-t-p & -J & v & -t-p \\
q & t+p & -t-p & u
\end{bmatrix}.$$

Define $T \equiv t + p$, one has

$$\begin{bmatrix} u & T & -T & q \\ T & v & -J & T \\ -T & -J & v & -T \\ q & T & -T & u \end{bmatrix}.$$

Then we have the eigenvectors and their eigenenergies:

Eigenstate	*Eigenenergy*
$\boldsymbol{\xi}_1 = \mathbf{e}_1$	$v - J$
$\boldsymbol{\xi}_2 = \mathbf{e}_2$	$v - J$
$\boldsymbol{\xi}_3 = \frac{1}{\sqrt{2}}(\mathbf{e}_4 + \mathbf{e}_5)$	$v - J$
$\boldsymbol{\xi}_4 = \frac{1}{\sqrt{2}}(-\mathbf{e}_3 + \mathbf{e}_6)$	$u - q$
$\boldsymbol{\xi}_5$	$v + \frac{1}{2}(u + q - v + J) - \frac{1}{2}\sqrt{(u + q - v - J)^2 + 16T^2}$
$\boldsymbol{\xi}_6$	$v + \frac{1}{2}(u + q - v + J) + \frac{1}{2}\sqrt{(u + q - v - J)^2 + 16T^2}$

,

where the the 5th and 6th eigenvectors are the superpositions of basis $\mathbf{e}_3$ through $\mathbf{e}_6$ but too complicated to show.

There are several important observations:

- The triplet (magnetic) states $\boldsymbol{\xi}_1$, $\boldsymbol{\xi}_2$ and $\boldsymbol{\xi}_3$ have the same energy, but the singlet state is not an eigenstate.

- The ground state can be magnetic or nonmagnetic depending on the parameters u, v, J, q and T. Apparently the two lowest energies are $v - J$ and $\frac{1}{2}(u + q + v + J) - \frac{1}{2}\sqrt{(u + q - v - J)^2 + 16T^2}$. If

$$J^2 + J(u + q - v) > 2T^2, \tag{61}$$

  $\boldsymbol{\xi}_1$ through $\boldsymbol{\xi}_3$ are the ground states, otherwise, the nonmagnetic state $\boldsymbol{\xi}_5$ is the ground state. Hence, J is an extremely important parameter, although it may be much smaller than u and T. As we know, u should be the largest among these parameters, so it is not so difficult to satisfy (61) even if J is much smaller than T.

Integral J represents the energy for exchanging two nearest neighbor indistinguishable particles, which is completely a quantum effect. The two particles have to have the same spin to be able to do this. So this is really an "exchange" energy, which favors alignment of spins to the same orientation.

Let's take a look at these parameters now in the case of two $3d$ electrons.

Parameter u is the on-site repulsion energy, Hubbard [74] estimated u as 20 eV for $3d$ electrons.

Parameter v is the coulomb energy of two electrons on nearest neighbors, estimated as 1/40 eV by Hubbard.

Parameter J is the exchange energy of two electrons in two nearest neighbor sites, 3 eV for $3d$ electrons again according to Hubbard, considering the screening.

Parameter p is like the hopping energy of single electron, which is estimated as 1/2 eV by Hubbard for $3d$ electrons.

Parameter q is the hopping energy of two electrons from one site to the nearest neighbor at the same time, Hubbard estimated it of order as v, 1/40 eV.

Parameter t is the single electron hopping energy considered in single electron picture, which is basically the band-width divided by twice of the number of nearest neighbors. This should be on the order of 1/2 eV.

If we plug in these numbers

$$\begin{aligned} u &= 20 \text{ eV} \\ v &= 1/40 \text{ eV} \\ J &= 3 \text{ eV} \\ t &= 1/2 \text{ eV} \\ p &= 1/2 \text{ eV} \\ q &= 1/40 \text{ eV}, \end{aligned}$$

we actually get $uJ \gg 2T^2$, which means $v - J$ is lower energy.

A.1.2 Hubbard model

In Hubbard model [74], the only parameters that are retained are u and T. Therefore, the Hamiltonian becomes

$$H_R^{Hubbard} = \begin{bmatrix} 0 & 0 & 0 & 0 & 0 & 0 \\ 0 & 0 & 0 & 0 & 0 & 0 \\ 0 & 0 & u & T & -T & 0 \\ 0 & 0 & T & 0 & 0 & T \\ 0 & 0 & -T & 0 & 0 & -T \\ 0 & 0 & 0 & T & -T & u \end{bmatrix}.$$

The eigenstates and eigenenergies are

Eigenstate	Eigenenergy
$\boldsymbol{\xi}_1^{Hubbard} = \mathbf{e}_1$	0
$\boldsymbol{\xi}_2^{Hubbard} = \mathbf{e}_2$	0
$\boldsymbol{\xi}_3^{Hubbard} = \frac{1}{\sqrt{2}}(\mathbf{e}_4 + \mathbf{e}_5)$	0
$\boldsymbol{\xi}_4^{Hubbard} = \frac{1}{\sqrt{2}}(-\mathbf{e}_3 + \mathbf{e}_6)$	u
$\boldsymbol{\xi}_5^{Hubbard} = \frac{4T\mathbf{e}_3+(-u-\sqrt{16T^2+u^2})\mathbf{e}_4+(u+\sqrt{16T^2+u^2})\mathbf{e}_5+4T\mathbf{e}_6}{4u^2+64T^2+4u\sqrt{16T^2+u^2}}$	$\frac{1}{2}u - \frac{1}{2}\sqrt{u^2+16T^2}$
$\boldsymbol{\xi}_6^{Hubbard} = \frac{4T\mathbf{e}_3+(-u+\sqrt{16T^2+u^2})\mathbf{e}_4+(u-\sqrt{16T^2+u^2})\mathbf{e}_5+4T\mathbf{e}_6}{4u^2+64T^2-4u\sqrt{16T^2+u^2}}$	$\frac{1}{2}u + \frac{1}{2}\sqrt{u^2+16T^2}$.

Falicov studied this problem carefully [54] using Hubbard model and found the same result as ours: the system is never magnetic no matter how you tune the parameters u and T. It is not difficult to see that the nonmagnetic state $\boldsymbol{\xi}_5^{Hubbard}$ is always the ground state. From the criteria (61) we can see that this is simply because the model ignored the important parameter J.

A.1.3 Stoner model

It is interesting that by applying the two parameters u and T, Stoner model [188] actually is able to predict the possible existence of magnetic states. The Stoner model can be treated as a Hubbard model in molecular orbital space, considering only the on-diagonal terms. To deal with this problem, using Stoner's model, we should get the Hamiltonian in molecular orbital basis. The two atomic orbitals are

$$\begin{aligned}\varphi_a &= \frac{1}{\sqrt{2}}(\phi_A + \phi_B) \\ \varphi_b &= \frac{1}{\sqrt{2}}(\phi_A - \phi_B),\end{aligned}$$

with energy $\epsilon_a = -T$ and $\epsilon_b = T$. The second quantization basis are

$$\begin{aligned}\mathbf{f}_1 &\equiv |\uparrow_a \uparrow_b\rangle \\ \mathbf{f}_2 &\equiv |\downarrow_a \downarrow_b\rangle \\ \mathbf{f}_3 &\equiv |\uparrow_a \downarrow_a\rangle \\ \mathbf{f}_4 &\equiv |\uparrow_a \downarrow_b\rangle \\ \mathbf{f}_5 &\equiv |\downarrow_a \uparrow_b\rangle \\ \mathbf{f}_6 &\equiv |\uparrow_b \downarrow_b\rangle\,,\end{aligned}$$

The transformation matrix between $\{\mathbf{e}_i\}$ and $\{\mathbf{f}_i\}$ is

$$\alpha = \begin{bmatrix} 1 & 0 & 0 & 0 & 0 & 0 \\ 0 & 1 & 0 & 0 & 0 & 0 \\ 0 & 0 & 1/2 & -1/2 & 1/2 & 1/2 \\ 0 & 0 & -1/2 & -1/2 & 1/2 & 1/2 \\ 0 & 0 & 1/2 & -1/2 & 1/2 & -1/2 \\ 0 & 0 & 1/2 & 1/2 & -1/2 & 1/2 \end{bmatrix}$$

Hence

$$H_k = \alpha^T * H_R * \alpha,$$

and we have

$$H_k = \begin{bmatrix} v-J & 0 & 0 & 0 & 0 & 0 \\ 0 & v-J & 0 & 0 & 0 & 0 \\ 0 & 0 & \begin{matrix}-2T+\frac{1}{2}J+\frac{1}{2}u \\ +\frac{1}{2}q+\frac{1}{2}v\end{matrix} & 0 & 0 & \begin{matrix}-\frac{1}{2}J+\frac{1}{2}u \\ +\frac{1}{2}q-\frac{1}{2}v\end{matrix} \\ 0 & 0 & 0 & \begin{matrix}-\frac{1}{2}J+\frac{1}{2}u \\ -\frac{1}{2}q+\frac{1}{2}v\end{matrix} & \begin{matrix}\frac{1}{2}J-\frac{1}{2}u \\ +\frac{1}{2}q-\frac{1}{2}v\end{matrix} & 0 \\ 0 & 0 & 0 & \begin{matrix}\frac{1}{2}J-\frac{1}{2}u \\ +\frac{1}{2}q-\frac{1}{2}v\end{matrix} & \begin{matrix}-\frac{1}{2}J+\frac{1}{2}u \\ -\frac{1}{2}q+\frac{1}{2}v\end{matrix} & 0 \\ 0 & 0 & \begin{matrix}-\frac{1}{2}J+\frac{1}{2}u \\ +\frac{1}{2}q-\frac{1}{2}v\end{matrix} & 0 & 0 & \begin{matrix}2T+\frac{1}{2}J+\frac{1}{2}u \\ +\frac{1}{2}q+\frac{1}{2}v\end{matrix} \end{bmatrix}.$$

If we ignore v, J and q, we have Hubbard Hamiltonian

$$H_k^{Hubbard} = \begin{bmatrix} 0 & 0 & 0 & 0 & 0 & 0 \\ 0 & 0 & 0 & 0 & 0 & 0 \\ 0 & 0 & -2T+\frac{1}{2}u & 0 & 0 & \frac{1}{2}u \\ 0 & 0 & 0 & \frac{1}{2}u & -\frac{1}{2}u & 0 \\ 0 & 0 & 0 & -\frac{1}{2}u & \frac{1}{2}u & 0 \\ 0 & 0 & \frac{1}{2}u & 0 & 0 & 2T+\frac{1}{2}u \end{bmatrix}.$$

Looking only at the on-diagonal terms, the difference $u/2 - 2T$ will decide if the system is magnetic. Although the Stoner model is able to predict the existence of magnetic states, the conclusion is dubious, because if two atoms are remote ($T = 0$), the model still predicts spin alignment, which is against common sense. The exact solution, from this case yields $J = 0$ as well as $T = 0$, causing the magnetic and non-magnetic states degenerate. Thus, the spin alignment has nothing to do with energy there.

A.2 Two electron atom problem

A small modification of Hamiltonian (59) will lead us to the two-electron atom problem. This is like the helium atom, but again we treat it as fictitious atom for which we can tune the parameters.

$$H = \frac{p_1^2}{2m_e} + \frac{p_2^2}{2m_e} + \frac{e^2}{4\pi\epsilon_0}(-\frac{1}{r_1} - \frac{1}{r_2} + \frac{1}{r_{12}}).$$

This time, we don't need to apply Born-Oppenheimer approximation because there is only one nucleus. Again one can regroup the Hamiltonian as

$$H = H_1 + H_2 + H_{12},$$

where

$$\begin{aligned} H_1 &= \frac{p_1^2}{2m_e} - \frac{1}{r_1} \\ H_2 &= \frac{p_2^2}{2m_e} - \frac{1}{r_2} \\ H_{12} &= \frac{1}{r_{12}}. \end{aligned}$$

We can choose the two lowest solution of H_1 ϕ_a and ϕ_b as the starting point and write down the second quantization Hamiltonian:

$$H = \epsilon_i \sum_{i,\sigma} C_{i\sigma}^+ C_{i\sigma} + \frac{1}{2} \sum_{ijkl,\sigma} U_{ijkl} C_{i\sigma}^+ C_{j\sigma'}^+ C_{k\sigma'} C_{l\sigma},$$

where the basis are

$$\begin{aligned} \mathbf{g}_1 &\equiv |\uparrow_a \uparrow_b\rangle \\ \mathbf{g}_2 &\equiv |\downarrow_a \downarrow_b\rangle \\ \mathbf{g}_3 &\equiv |\uparrow_a \downarrow_a\rangle \\ \mathbf{g}_4 &\equiv |\uparrow_a \downarrow_b\rangle \\ \mathbf{g}_5 &\equiv |\downarrow_a \uparrow_b\rangle \\ \mathbf{g}_6 &\equiv |\uparrow_b \downarrow_b\rangle . \end{aligned}$$

Now we have more types of integrals.

$$\begin{aligned} u_a &\equiv U_{aaaa} \\ u_b &= U_{bbbb} \\ v &\equiv U_{abba} = U_{baab} \\ J &\equiv U_{abab} = U_{baba} \\ p_a &\equiv U_{baaa} \\ p_b &\equiv U_{abbb} \\ q &\equiv U_{aabb} = U_{bbaa}. \end{aligned}$$

The matrix of the Hamiltonian is

$$\begin{bmatrix} \epsilon_a + \epsilon_b & 0 & 0 & 0 & 0 & 0 \\ +v - J & & & & & \\ 0 & \epsilon_a + \epsilon_b & 0 & 0 & 0 & 0 \\ & +v - J & & & & \\ 0 & 0 & 2\epsilon_a + u_a & p_a & -p_b & q \\ 0 & 0 & p_a & \epsilon_a + \epsilon_b + v & -J & p_a \\ 0 & 0 & -p_b & -J & \epsilon_a + \epsilon_b + v & -p_b \\ 0 & 0 & q & p_a & -p_b & 2\epsilon_b + u_b \end{bmatrix},$$

Unfortunately, the analytical solution of this Hamiltonian defies a simple interpretation. However we can look at some very useful special cases.

A.2.1 Case 1: $\epsilon_a = \epsilon_b = \epsilon$, $p_a = p_b = p$, $u_a = u_b = u$

In this case the two states ϕ_a and ϕ_b are degenerate. The solution is

Eigenstate	*Eigenenergy*
$\boldsymbol{\xi}_1 = \mathbf{e}_1$	$2\epsilon + v - J$
$\boldsymbol{\xi}_2 = \mathbf{e}_2$	$2\epsilon + v - J$
$\boldsymbol{\xi}_3 = \frac{1}{\sqrt{2}}(\mathbf{e}_4 + \mathbf{e}_5)$	$2\epsilon + v - J$
$\boldsymbol{\xi}_4 = \frac{1}{\sqrt{2}}(-\mathbf{e}_3 + \mathbf{e}_6)$	$2\epsilon + u - q$
$\boldsymbol{\xi}_5$	$2\epsilon + v + \frac{1}{2}(J + q + u - v) - \frac{1}{2}\sqrt{(u - v - J + q)^2 + 16p^2}$
$\boldsymbol{\xi}_6$	$2\epsilon + v + \frac{1}{2}(J + q + u - v) + \frac{1}{2}\sqrt{(u - v - J + q)^2 + 16p^2}$

Whether the magnetic states are the ground states depends on the relative size of $J^2 + J(u + q - v)$ and $2p^2$. Normally, the former is much larger than the latter, which favors the alignment of the two spins. This is actually one of the Hund's rules.

A.2.2 Case 2: $p_a = p_b = 0$

In thise case the mixing of the two states is ignored. The solution is

Eigenstate	*Eigenenergy*
$\boldsymbol{\xi}_1 = \mathbf{e}_1$	$\epsilon_1 + \epsilon_2 + v - J$
$\boldsymbol{\xi}_2 = \mathbf{e}_2$	$\epsilon_1 + \epsilon_2 + v - J$
$\boldsymbol{\xi}_3 = \frac{1}{\sqrt{2}}(\mathbf{e}_4 + \mathbf{e}_5)$	$\epsilon_1 + \epsilon_2 + v - J$
$\boldsymbol{\xi}_4 = \frac{1}{\sqrt{2}}(-\mathbf{e}_4 + \mathbf{e}_5)$	$\epsilon_1 + \epsilon_2 + v + J$
$\boldsymbol{\xi}_5 = \frac{[-(\epsilon_1-\epsilon_2)-\sqrt{q^2+(\epsilon_1-\epsilon_2)^2}]\mathbf{e}_3 + q\mathbf{e}_6}{2q^2+2(\epsilon_1-\epsilon_2)^2+2(\epsilon_1-\epsilon_2)\sqrt{q^2+(\epsilon_1-\epsilon_2)^2}}$	$\epsilon_1 + \epsilon_2 + v + u - \sqrt{q^2 + (\epsilon_1 - \epsilon_2)^2}$
$\boldsymbol{\xi}_6 = \frac{[-(\epsilon_1-\epsilon_2)+\sqrt{q^2+(\epsilon_1-\epsilon_2)^2}]\mathbf{e}_3 + q\mathbf{e}_6}{2q^2+2(\epsilon_1-\epsilon_2)^2-2(\epsilon_1-\epsilon_2)\sqrt{q^2+(\epsilon_1-\epsilon_2)^2}}$	$\epsilon_1 + \epsilon_2 + v + u + \sqrt{q^2 + (\epsilon_1 - \epsilon_2)^2}$

The condition for magnetic states to be the ground states is that $u + J > \sqrt{q^2 + (\epsilon_1 - \epsilon_2)^2}$. Apparently, if the energy difference $\epsilon_1 - \epsilon_2$ is large enough, electrons will both occupy the lower states. Otherwise the Coulomb repulsion will keep them apart.

A.3 Summary

The exact solution of two electron homopolar molecule problem has been discussed, which clarifies the deficiency of Hubbard and Stoner models. Both magnetic and non-magnetic

states are predicted by the exact solution under certain conditions.

It is not so difficult to extend this model to a molecule with more sites, or maybe even to the infinite single band system. However, the multiband case can be much more complicated.

APPENDIX B

STATISTICAL THERMODYNAMICS OF CLUSTER BEAM

In a laser ablation source, the metal sample is vaporized by intense laser pulses creating a hot metal-ion plasma. Clusters are generated out of the hot plasma which releases the heat. Therefore clusters are very hot when they are created and all degrees of freedom (translational, rotational, vibrational and electronic) are excited. There are two mechanisms that can take away energy from the clusters and thereby reduce their temperature. Thermalization occurs with the background gas in the source cavity and in the subsequent adiabatic expansion through the nozzle. We are going to discuss these two mechanisms.

B.1 Thermalization in the source

B.1.1 Degrees of freedom

In the source cavity, clusters are thermalized by collisions with background He gas. The thermalization rate or relaxation time is different for the various degrees of freedom. The translational temperature (T_T) is the easiest to thermalize, then the rotational temperature (T_R) and vibrational temperature (T_v). It has been shown [119] [23] that in the source with a pressure of about 100 Torr and temperature 300 K, the vibrational relaxation time is on the order 10 μs. The relaxation time is inversely proportional to number of collisions per unit time

$$n_{collision} \sim \frac{\sigma_{cross} P}{\sqrt{k T_{He} m_{He}}}, \tag{62}$$

where σ_{cross} is the cross-section of the collision, P is the pressure, T_{He} is the temperature of the background He gas and m_{He} is the mass of He atom. We find that the vibrational relaxation time at 1 Torr and 20 K is about 0.2 ms, which is well below the dwell time in the source that we measured in the experiment ($\sim$ 2 ms at 20 K). The relaxation times for

rotations and translations are shorter than for the vibration, so that the thermalization with the background gas should be complete too. Hence, thermalization of these three degrees of freedom are complete for all source conditions used in the experiments [58]. However, the electronic degree of freedom is more difficult to thermalize than the other three. If the relaxation time for electronic energy is one order of magnitude greater than for vibration, the experiment will be running on the edge. In other words, the thermalization of electronic energy will be very sensitive to the source conditions (i.e., pressure and temperature). In the next section, we'll show how to adjust the source condition to change thermalization.

B.1.2 Two-chamber system

Here we are concerned with the problem of gas discharge in the reservoir and source cavity. We can consider this problem generically as a two-chamber problem shown in Figure 51, where chamber 1 represents the reservoir, chamber 2 represents the source cavity.

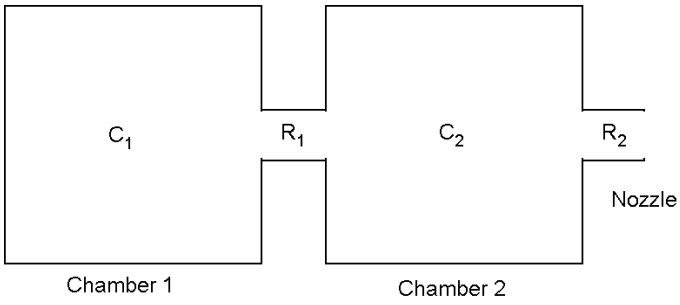

Figure 51: The generic problem of two chambers.

Make an analogy with electric circuit, we can imagine that those two-chambers have capacitance C_1 and C_2 and amount of gas N_1 and N_2. The connection between first and the second chamber should have a resistance R_1, and for the nozzle, we have R_2, which represents the resistance of the gas discharge via nozzle. The differential equations are:

$$-\frac{dN_1}{dt} = \frac{N_1}{C_1R_1} - \frac{N_2}{C_2R_1} \tag{63}$$

$$-\frac{dN_1}{dt} - \frac{dN_2}{dt} = \frac{N_2}{C_2R_2}. \tag{64}$$

From (63), we get

$$N_2 = (\frac{dN_1}{dt} + \frac{N_1}{C_1R_1})C_2R_1,$$

plug into (64), one gets the second order differential equation

$$C_2R_1\frac{d^2N_1}{dt^2} + (\frac{C_2}{C_1} + \frac{R_1}{R_2} + 1)\frac{dN_1}{dt} + \frac{N_1}{C_1R_2} = 0.$$

Suppose the initial conditions is $N_1 = N_0$ and $N_2 = 0$, the solution is

$$\begin{aligned} N_1 &= a_1e^{-\upsilon_1 t} + a_2e^{-\upsilon_2 t} \\ N_2 &= C_2a_1(\frac{1}{C_1} - \upsilon_1R_1)e^{-\upsilon_1 t} + C_2a_2(\frac{1}{C_1} - \upsilon_2R_1)e^{-\upsilon_2 t}, \end{aligned}$$

where

$$\begin{aligned} \upsilon_1 &= \frac{\frac{C_2}{C_1} + \frac{R_1}{R_2} + 1 + \sqrt{(\frac{C_2}{C_1} + \frac{R_1}{R_2} + 1)^2 - 4\frac{C_2R_1}{C_1R_2}}}{2C_2R_1} \\ \upsilon_2 &= \frac{\frac{C_2}{C_1} + \frac{R_1}{R_2} + 1 - \sqrt{(\frac{C_2}{C_1} + \frac{R_1}{R_2} + 1)^2 - 4\frac{C_2R_1}{C_1R_2}}}{2C_2R_1} \\ a_1 &= \frac{\upsilon_2 - \frac{1}{C_1R_1}}{\upsilon_2 - \upsilon_1}N_0 \\ a_2 &= \frac{\upsilon_1 - \frac{1}{C_1R_1}}{\upsilon_1 - \upsilon_2}N_0. \end{aligned}$$

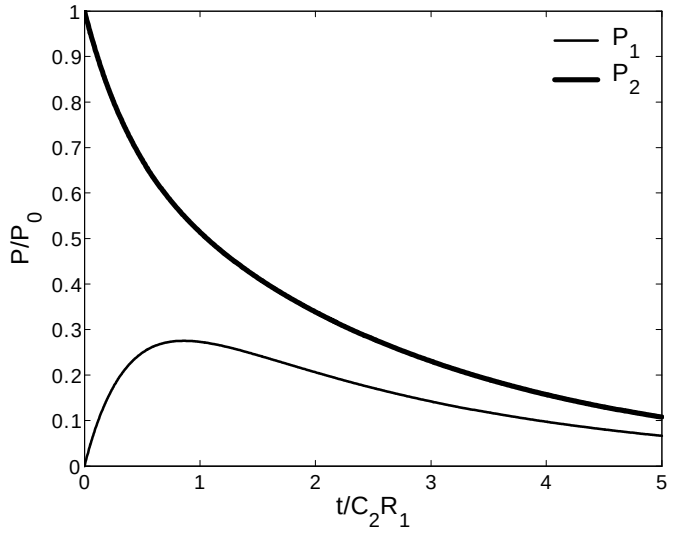

Figure 52: General behavior of discharge in the two-chamber system. Parameters assumed here are $\frac{C_2}{C_1} = 1$ and $\frac{R_2}{R_1} = 1$.

The behavior of gas discharge is shown in Figure 52. The pressure is defined as $P \equiv \frac{N}{C}$, and P_0 is the initial pressure in the first chamber. Basically, the pressure in first chamber decreased monotonically, in second chamber it shows a peak, which is crucial for the thermalization of metal vapor in the experiments.

The parameters used in Figure 52 are $\frac{C_1}{C_2} = 1$ and $\frac{R_2}{R_1} = 1$, which is not the case for the real source. For the real source, since the volume of the first and second chambers are 0.05 cm^3 and 0.25 cm^3 respectively, the ratio $\frac{C_1}{C_2}$ is about 5. For the resistance, because $R \propto \frac{l}{A}$, where l is the length and A is the area of the cross-section, we can estimate the ratio from the dimension of the nozzles and the tunnel between reservoir and the source cavity. The ratios $\frac{R_1}{R_2}$ are about 100, 70 and 50, for short, intermediate and long nozzle we used in the experiments.

Now we can plug in the real numbers for real case to get an idea of how the discharge depends on the source conditions.

Because the second pulsed valve connects the first and second chamber, and the duration (T_1) from which the valve is open can be controlled externally. We will tune T_1 and see the response. In Figure 53, the discharge with different T_1 is shown. Note that, when the valve is closed, the discharge in the second chamber becomes faster. Therefore, to get a stronger pulse, the duration T_1 should not be much less than C_2R_1. The calculation assumed that $\frac{C_1}{C_2} = 1$ and $\frac{R_1}{R_2} = 50$.

Another parameter that can be varied in the experiments is the length of the nozzle, corresponding to change of the resistance R_2.

In Figure 54, it is obvious that the smaller the resistance ratio $\frac{R_1}{R_2}$, the higher and the broader the peak is for the pressure in the second chamber. The three curves correspond more or less to the three nozzles we used in the experiments.

Another observation from Figure 53 and Figure 54 is the reduced pressure in the second chamber compared with the initial pressure in the first chamber. Assuming that the first chamber (reservoir) has a initial pressure $P_0 = 0.1$ bar$= 76$ Torr, we can find that the maximum pressure in the second chamber (source cavity) will be only about 1 Torr.

Hence, the conclusion is by the adjusting the second pulse value timing and the length

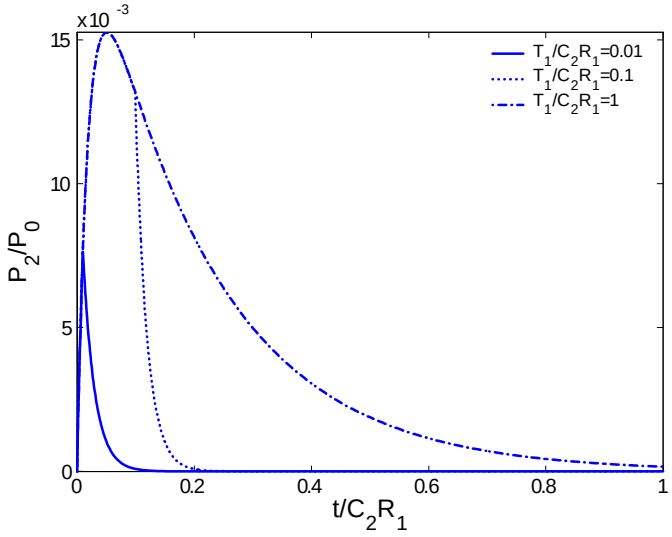

Figure 53: Gas discharge in first and second chamber with different pulse valve timing. Note that when the valve between first and second chamber close early, the gas pressure can not reach maximum. The parameters assumed here are $\frac{C_2}{C_1} = 5$, $\frac{R_1}{R_2} = 50$.

of the nozzle, thermalization conditions can be adjusted. As mentioned in B.1.1, for translation, rotation and vibration, the thermalization is complete for all source conditions used in the experiments. But for the electronic degree of freedom, thermalization can be adjusted from poor to good. Hence the parameter changes will affect the thermalization of the electronic states.

B.2 Free jet expansion

After the thermalization in the source cavity, the clusters mixed with the background gas will exit the source and freely expand out the nozzle. The free jet expansion will cool the background gas and it will also affect the temperature of the clusters. For He carrier gas, the only degree of freedom here is the translation, which is very easy to cool [161]. However for the clusters, the case is more complicated. Although the translational temperature of clusters is reduced, it has been shown experimentally that the vibrations of clusters are not affected by the expansion even at higher pressures [34]. The electronic degree of freedom should not be affected either. The rotational temperature may be reduced, but not much

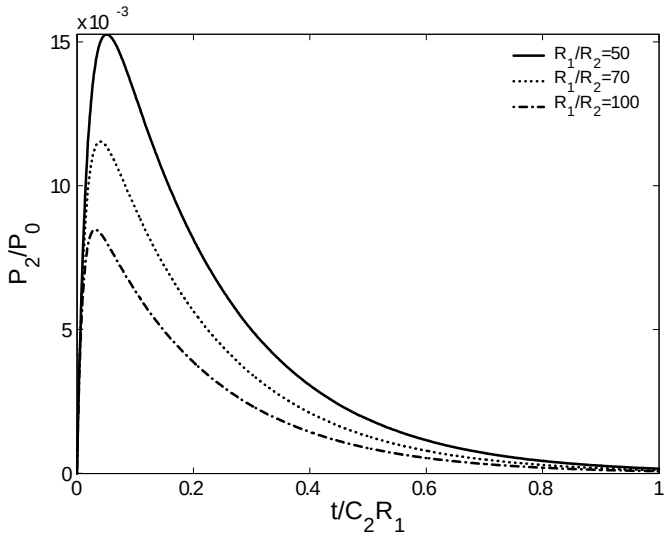

Figure 54: Gas discharge in first and second chamber with different nozzle length. Note that when the resistence of the nozzle is higher, corresponding longer nozzle, the distribution of amount of gas in second chamber is not only broader, but also with higher peak. The parameters assumed here are $\frac{C_2}{C_1} = 50$, $T_1 = \infty$.

more than the vibrational temperature [161]. In our two-chamber source, the reduced pressure will make the expansion quasi-effusive [23], reducing the beam speed. For supersonic expansion, the mean speed of background He gas is $\sqrt{\frac{5k_BT}{m_{He}}}$. For effusion the mean speed is $\sqrt{\frac{3k_BT}{m_{He}}}$ [3]. In contrast, we find the beam speed to be $\sqrt{\frac{2k_BT}{m_{He}}}$, suggesting a large velocity slip, which reduces the cooling effect of the expansion [93]. Because the pressure-nozzle diameter product (PD factor) for our source is 1 to 2 orders of magnitude smaller than reported in Ref [93], we expect little or no rotational cooling in experiment, extrapolating their empirical relation between PD and reduction of the rotational temperature.

B.3 Cluster beam

At about 10 nozzle diameters downstream from the source, the first skimmer extracts the center line of the free jet, generating the cluster beam. After the first skimmer, clusters enter the collision free chamber with much lower pressure (10^{-6} Torr). Note that statistics of clusters in a beam need to be treated carefully because they are measured in a very different environment than the source in which they were generated.

B.3.1 Frozen canonical ensemble

The cluster beam ensemble is a special ensemble compared with the common types, i.e., microcanonical, canonical and grand canonical ensembles. As discussed above, clusters are generated in the source at a well-defined temperature and reach equilibrium with the source. At this point clusters can be considered as canonical ensemble [71] with a well-defined temperature T_{source}. The energy of each cluster fluctuates quickly, but the ensemble average is constant. After the free jet expansion, the clusters are isolated from the background gas and other clusters. Each individual cluster has to be described using microcanonical ensemble, for which the energy is constant. Since the free jet expansion hardly affects the rotation, vibration and electronic energy, the collection of clusters still represents the canonical ensemble with temperature T_{source}, however the energy of each cluster does not fluctuate. It is like a snapshot of the canonical ensemble, which we call the frozen canonical ensemble.

B.3.1.1 Energy distribution

The energy distribution of clusters can be described by canonical ensemble characterized by the temperature T_{source}. The fact that the clusters are small and comprise only a few atoms makes a crucial difference here.

Continuous spectrum If the energy separation of the clusters is much smaller than $k_B T_{source}$, the spectrum can be consider continuous. Normally, for the temperature that is higher than 20 K, the spectra of translations and rotation can both be considered to be continuous. Therefore, the average energy is

$$< E >= \frac{\int_0^\infty E N(E) e^{-E/k_B T} dE}{\int_0^\infty N(E) e^{-E/k_B T} dE},$$

where E is the energy, $N(E)$ is the density of states. For a density of states that is proportional to γth power of energy, say $N(E) \propto E^\gamma$, one finds that

$$< E >= (\gamma + 1) k_B T.$$

We can also calculate the energy fluctuation defined by

$$\Delta E \equiv \sqrt{< (E - < E >)^2 >} = \sqrt{< E^2 > - < E >^2}.$$

Since $< E^2 >= (\gamma + 1)(\gamma + 2)(k_B T)^2$, so that $\Delta E = \sqrt{(\gamma + 1)} k_B T$.

An important observation is the relation between γ and number of degrees of freedom. Generally speaking, the total number of degrees of freedom for a cluster of N_a atoms is $3N_a$. Since $\gamma \sim \frac{3N_a}{2} - 1$, one has $\frac{\Delta E}{<E>} \sim \frac{1}{\sqrt{(\gamma+1)}} \sim \sqrt{\frac{2}{3N_a}}$, which suggests that the fluctuations for small clusters are much larger than for bulk.

Discrete spectrum If the energy level separation in the clusters is on the order of or larger than $k_B T_{source}$, then the spectrum has to be treated as discrete. For small clusters, at low temperature, the vibrational and electronic energies belong to this category. Therefore, the average energy is

$$< E >= \frac{\sum_{n=0}^{\infty} E_n D_n e^{-E_n/k_B T}}{\sum_{n=0}^{\infty} D_n e^{-E_n/k_B T}},$$

where D_n is the degeneracy. If we assume the energy spectrum is uniformly spaced (in other words $E_n = n\delta$ and $D_n = 1$, where δ is the energy spacing), we find the average

$$\begin{aligned} < \quad E >&= \delta \frac{e^{-\delta/k_B T}}{1 - e^{-\delta/k_B T}} = \frac{\delta}{e^{\delta/k_B T} - 1} \\ < \quad E^2 >&= \delta^2 \frac{1 + e^{-\delta/k_B T}}{(1 - e^{-\delta/k_B T})^2}. \end{aligned} \tag{65}$$

Therefore

$$\Delta E = \delta \frac{1 + e^{-\delta/k_B T} - e^{-2\delta/k_B T}}{1 - e^{-\delta/k_B T}}.$$

Cobalt clusters

- Rotations

The rotational energy of a cluster is $E_r = \frac{\hbar^2 N_r (N_r + 1)}{2 I_r}$, where N_r is the rotational quantum number and I_r is the moment of inertia. For a rough estimate, we can assume the same density for clusters as for the bulk, and calculate the constant $B_r \equiv \frac{\hbar^2}{2 I_r}$.

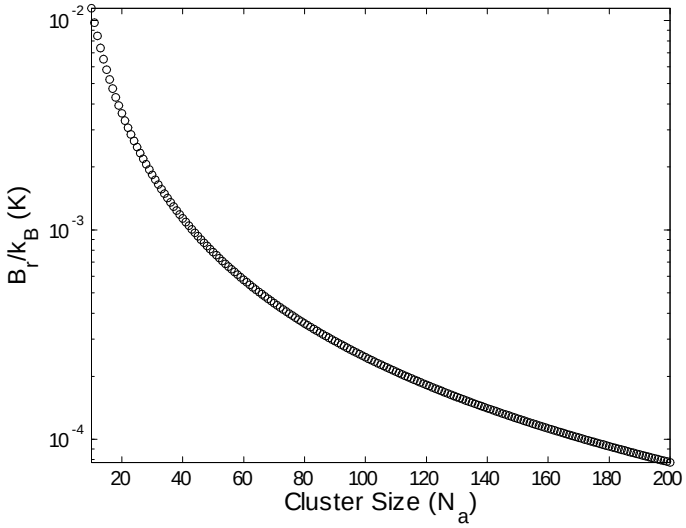

Figure 55: The rotational constant for cobalt clusters of different size.

The energy spacings of the rotational levels are much smaller than the lowest temperature we can achieve in experiment, therefore, rotation spectrum can be considered to be continuous.

- Vibrations

At low temperature, the vibrational spectrum of a cluster has to be treated as discrete. For the vibrational mode ω_i, the energy separation in (65) is $\delta_i = \hbar\omega_i$, hence the average number of phonons (i.e. occupied vibrational states) is $< n_i >= \frac{<E_i>}{\delta_i} = \frac{1}{e^{\delta/k_BT}-1}$. Since there are $3N_a-6$ modes in the clusters, where N_a is the number of atoms in the cluster. The total number of phonons in all the modes is $< n_{total} >= \sum_i < n_i >= \sum_i \frac{1}{e^{\delta/k_BT}-1}$. Because of the reduced size, clusters have a minimum frequency $\omega_{min} \sim \frac{\omega_{Debye}}{N_a^{1/3}}$, where ω_{Debye} is the bulk Debye frequency. The maximum frequency is also reduced from ω_{Debye}. Assuming a specific lattice structure and using the same spring constant as for the bulk, one can get an idea of of the distribution of vibrational modes.

Figure 56 shows an example of vibrational modes for Co_{10}. We can see the minimum frequency is almost one half of the ω_{Debye} ($T_{Debye} \equiv \frac{\hbar\omega_{Debye}}{k_B} = 445$ K [117]), and the maximum frequency is also lower than ω_{Debye}. This lower cutoff frequency inhibits the excitations of phonons in small clusters, as shown later below. Using the same assumptions

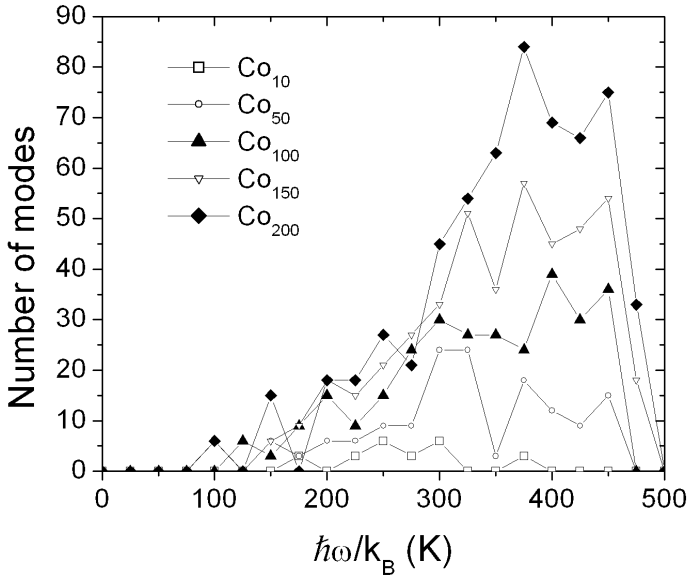

Figure 56: The number of vibrational modes of different energies assuming fcc lattice. Notice that the lower cutoff energy for small clusters is around 100 K.

as before, we can calculate total number of phonons in for different cluster sizes as a function of temperature.

Figure 57 shows the average total number of phonons for selected cobalt clusters. It is obvious that at $T = 20$ K, the average number of phonons is well below 0.1, even for cluster with as many as 200 atoms.

Alternatively we can calculate the probability that a cluster is in its ground vibrational state. For a certain mode ω_i, the probability is

$$p_i = \frac{e^{-\frac{1}{2}\hbar\omega_i/k_BT}}{\sum_{n=0}^{\infty} e^{-(n+\frac{1}{2})\hbar\omega_i/k_BT}} = 1 - e^{-\hbar\omega_i/k_BT}.$$

Considering all the modes, one has

$$p = \prod_i p_i = \prod_i (1 - e^{-\hbar\omega_i/k_BT}).$$

Figure 58 shows the probability p, which clearly shows the trend that at 20 K the clusters are frozen in their vibrational ground states.

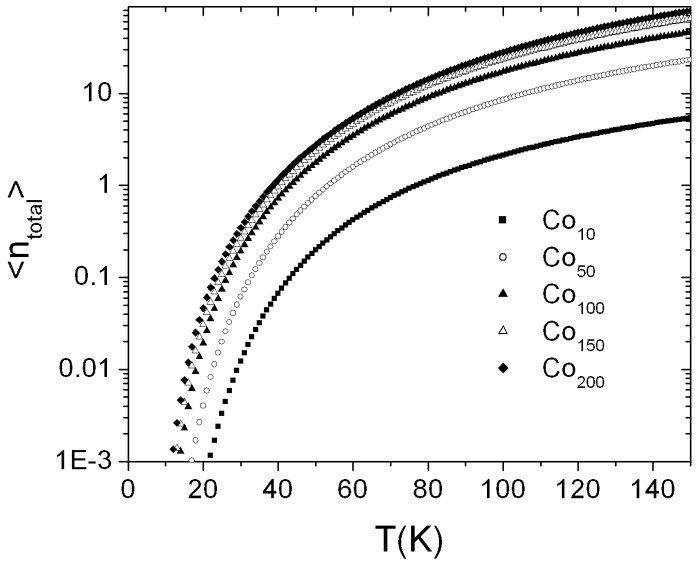

Figure 57: Average total number of phonons in Co_N clusters, which is based on fcc lattice and same spring constant between atoms as in the bulk.

B.3.2 Single clusters

The observed properties of clusters in a beam correspond to their ensemble behavior, yet the external perturbations we impose (magnetic field, electric field, photon illumination) are always on every single clusters, because the clusters are isolated. Therefore to analyze the response of the clusters to external perturbations, we start from isolated single clusters, which are described by the microcanonical ensemble.

For a normal microcanonical ensemble, energy is fixed, however there can be a large number of possible microstates. According to the equipartition theorem, the probability for every microstate is the same. If number of microstates at energy E is $\Omega(E)$, we can define the entropy of the system, and hence the temperature:

$$S(E) \equiv k_B ln\Omega \tag{66a}$$

$$\frac{1}{T} \equiv \frac{dS}{dE} = \frac{k_B dln\Omega}{dE}. \tag{66b}$$

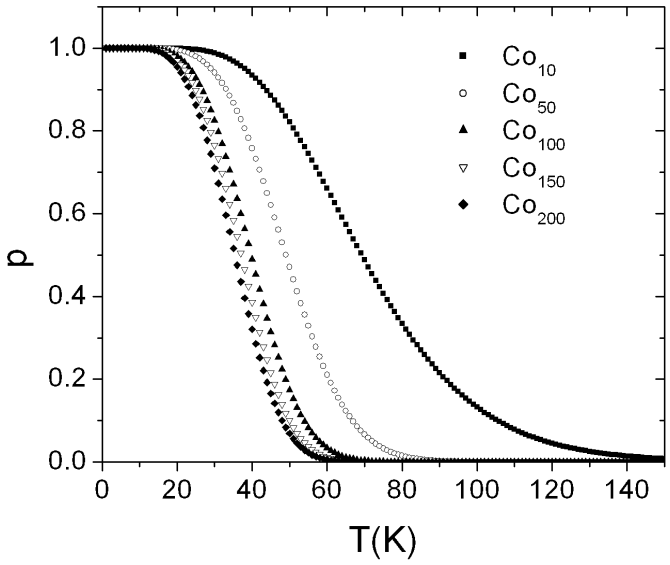

Figure 58: The propabilities for Co_N clusters to be at their ground vibrational states, which is based on fcc lattice and same spring constants between atoms in clusters as those in bulk.

B.3.2.1 Low energy

Because the picture of (66a) takes continuity and ergodicity as assumptions, it breaks down for low energy clusters.

Continuity At an energy scale less than the energy spacing, the energy spectrum can not be treated as continuous. We also showed that vibrations have a discrete spectrum. In this case, the definition of temperature using (66b) is not appropriate. Actually, it will give us unphysical temperature due to the crudeness of entropy energy relation. Therefore, for a single low-energy small particle, temperature is not a well-defined physical quantity. Total energy should be used instead.

Ergodicity While the vibrations become discrete for the low-energy clusters we study, the rotations remain almost continuous. However, because the clusters in the beam are free, we have to consider the conservation of angular moment. Note that conservation laws always destroy ergodicity [142] [18]. The more conservation laws the system has to obey,

the less ergodic the system is. To describe number of microstates, we have to be confined within a subspace that respects the conservation laws. For example, the equations (66a) should be replaced by $S(E, J, J_z) = k_B \ln \Omega(E, J, J_z)$, where J and J_z are the total angular momentum and the projection of angular moment on a certain direction. The consequence of the reduced ergodicity will be the incomplete relaxation.

B.3.2.2 High energy

In most of our experiments, clusters have very low energy. If vibrations are not excited, only three degrees of freedom corresponding to the rotations are left. Hence the mean energy is about $\frac{3}{2}k_BT$, which is a very small energy. On the other hand, if the energy of the cluster is actually much higher than $\hbar\omega_{Debye}$, we can use formula (66a) and (66b) to get the entropy, temperature, and even heat capacity.

Because of energy conservation, the total energy is the sum of the energy of each of the vibrational modes:

$$E_{vtotal} = \sum_{i=1}^{N_{modes}} n_i \hbar\omega_i, \tag{67}$$

where E_{vtotal} is total vibrational energy, N_{modes} is the number of vibrational modes of the cluster, n_i is the number of phonons for mode ω_i. If $E_{vtotal} \gg \hbar\omega_{Debye}$, one has $n_i^{max} = \frac{E_{vtotal}}{\hbar\omega_i}$, where n_i^{max} is the maximum number of phonons for mode ω_i. The number of microstates $\Omega(E_{vtotal})$ is the number of combinations of $\{n_i\}$ that satisfies (67).

To calculate $\Omega(E_{vtotal})$, we can consider a N_{modes} dimensional space for which the coordinates are $\{n_i\}$. Then $\Omega(E_{vtotal})$ is proportional the "area" of the $N_{modes} - 1$ dimensional plane described by (67). Apparently, using a geometry analogy, one has

$$\Omega(E_{vtotal}) \propto E_{vtotal}^{N_{modes}-1}. \tag{68}$$

From (68) and (66b), one gets the expression for temperature:

$$k_BT = \frac{E_{vtotal}}{N_{modes} - 1}. \tag{69}$$

Moreover, we can find the average number of phonons for mode ω_i,

$$\begin{aligned} < n_i >= & \frac{\int_0^{\frac{E_{vtotal}}{\hbar\omega_i}} n_i \Omega(E_{vtotal} - n_i\hbar\omega_i) dn_i}{\int_0^{\frac{E_{vtotal}}{\hbar\omega_i}} \Omega(E_{vtotal} - n_i\hbar\omega_i) dn_i} \\ = & \frac{\int_0^{\frac{E_{vtotal}}{\hbar\omega_i}} n_i (E_{vtotal} - n_i\hbar\omega_i)^{N_{modes}-2} dn_i}{\int_0^{\frac{E_{vtotal}}{\hbar\omega_i}} \Omega(E_{vtotal} - n_i\hbar\omega_i)^{N_{modes}-2} dn_i} \\ = & \frac{E_{vtotal}}{N_{modes}\hbar\omega_i}. \end{aligned} \tag{70}$$

It is interesting to look at the problem another way: assume that mode ω_i is connected the the rest of the modes which serve as a heat bath of temperature T. Thus

$$< n_i >= \frac{1}{e^{\hbar\omega_i/k_BT} - 1}.$$

For the high energy case $\hbar\omega_i/k_BT \ll 1$, $< n_i >= k_BT/\hbar\omega_i$. Invoking the temperature we just found in (69), one gets $< n_i >= \frac{E_{vtotal}}{(N_{modes}-1)\hbar\omega_i}$, which is slightly different from (70). The reason is that we did not consider change in the heat bath when we remove some energy from it. Nevertheless, even for cluster of 10 atoms, $N_{modes} = 24$, the difference is very small.

Example: photon heating In the photon heating experiment, if a cluster absorbs one photon of 500 nm wavelength, the additional energy is $E_{photon} = 2.5$ eV, which is several orders of magnitude higher than $\frac{3}{2}k_BT$. Because of angular momentum conservation, only a very small amount of energy will go into the rotational degree of freedom. Suppose the energy E_{photon} all goes to the vibrational degree of freedom, then, because $E_{photon} \gg \hbar\omega_{Debye}$, all of the vibrational modes will be excited.

Figure 59 shows the vibrational temperature for clusters of different size. Apparently, the temperature only depends on number of vibrational modes in the clusters, hence only on the number of atoms in cluster. In other words, as long as $E_{photon} \gg \hbar\omega_{Debye}$, Figure 59 presents a universal picture.

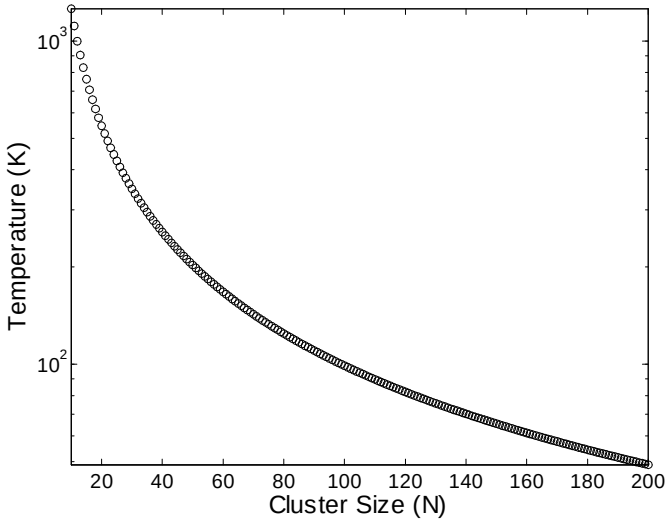

Figure 59: Vibrational temperature of clusters after absorption of a single photon of energy 2.5 eV, assuming no vibrational modes are excited before the absorption.

APPENDIX C

DECONVOLUTION OF BEAM PROFILE

As we know, in the Stern-Gerlach deflection experiment, when the field is off, the beam profile $I^{off}(\delta)$ observed represents the natural resolution of the apparatus, including collimation, time of flight uncertainty etc. When the field is turned on, the observed beam profile $I^{on}(\delta)$ is a convolution of the natural resolution ($I^{off}(\delta)$) and the distribution profile ($P(\delta)$) of clusters,

$$I^{on}(\delta) = I^{off}(\delta) \otimes P(\delta) \equiv \int_{-\infty}^{\infty} I^{off}(x)P(\delta - x)dx. \tag{71}$$

Hence, in principle if $I^{on}(\delta)$ and $I^{off}(\delta)$ are known, $P(\delta)$ can be found by deconvolution [81]. Clearly, the narrower the width of $I^{off}(\delta)$ is, the closer the profile $I^{on}(\delta)$ is to $P(\delta)$, which means that narrower collimation improves resolution. However, reduced collimation also reduces the intensity of the cluster beam. In other words increases the statistical uncertainty of the profile. Therefore the finite width of the $I^{off}(\delta)$ is unavoidable. We are really interested in $P(\delta)$. Hence it is of great significance in the data analysis to extract the profile $P(\delta)$ from the observed profiles $I^{on}(\delta)$ and $I^{off}(\delta)$.

The experimental data (i.e., I_i^{off} and δ_i) are sequences of N_p discrete numbers. The convolution is then

$$I_i^{on} = \sum_{j=1}^{N_p} I_j^{off} P_{i-j}, \tag{72}$$

where I_i^{on} I_i^{off} and P_i are the discrete profiles $I^{on}(\delta)$, $I^{off}(\delta)$ and $P(\delta)$. In principle, we can solve the profile P_i using linear algebra. Unfortunately, if we do that the result is always unsatisfactory: unphysical negative P_i will be found. This is because of the experimental errors in the data. Actually (71) and (72) only hold when the experimental data is collected for infinite amount of time, which will removes random noise in the profiles. In real cases, random noise is always there and not identical for $I^{on}(\delta)$ and $I^{off}(\delta)$, thus

$I^{on}(\delta) - RN_1(\delta) = (I^{off}(\delta) - RN_2(\delta)) \otimes P(\delta)$, where $RN_1(\delta)$ and $RN_2(\delta)$ are noise functions for profiles $I^{on}(\delta)$ and $I^{off}(\delta)$, respectively.

To deal with this problem, we introduced a method that allows deconvolution under certain circumstances. Instead of solving the linear equations (72), we build up a trial function $P^{trial}(\delta)$, and minimize the absolute difference $\left|I^{on}(\delta) - I^{off}(\delta) \otimes P^{trial}(\delta)\right|$. The algorithm is briefed as following:

- Calculate the first and second moments differences between profiles $I^{on}(\delta)$ and $I^{off}(\delta)$.
- Construct a Gaussian function using these differences just found as the initial trial function.
- Calculate the difference $I^{dif}(\delta) \equiv I^{on}(\delta) - I^{off}(\delta) \otimes I^{trial}(\delta)$.
- Use the function $I^{dif}(\delta)$ as a feedback to improve the trial function $P^{trial}(\delta) = P^{trial}(\delta) - \lambda_{feedback} I^{dif}(\delta)$, where $\lambda_{feedback}$ is the parameter for feedback strength. $\lambda_{feedback}$ is positive and much smaller than 1. $P^{trial}(\delta)$ is forced to be positive.
- Repeat the two proceeding steps until the difference is small enough.
- The function $P^{trial}(\delta)$ now is the deconvolved profile $P^{deconv}(\delta)$.

Figure 60 shows an example of the results of our deconvolution method. The convolution $I^{off}(\delta) \otimes P^{deconv}(\delta)$ fits the raw data $I^{on}(\delta)$ very well. After the deconvolution the two peaks become well resolved in the profile $P^{deconv}(\delta)$. The absolution value of profile $P^{deconv}(\delta)$ shows the intensity change between the profiles $I^{off}(\delta)$ and $I^{on}(\delta)$, which is shown by the relation

$$\int_{-\infty}^{\infty} P^{deconv}(\delta) d\delta = \frac{\int_{-\infty}^{\infty} I^{on}(\delta) d\delta}{\int_{-\infty}^{\infty} I^{off}(\delta) d\delta}.$$

Unfortunately this method is not universal. It works for the case that width of $I^{on}(\delta)$ is clearly larger than width of $I^{off}(\delta)$, in other words significant broadening of $I^{on}(\delta)$ compared with $I^{off}(\delta)$. Nevertheless, it is excellent for analyzing beam profiles of iron group clusters for which the width change is on the same order of the width of profile $I^{off}(\delta)$. The uncertainty of the method is reflected in the broadening of the profile $P^{deconv}(\delta)$. In fact,

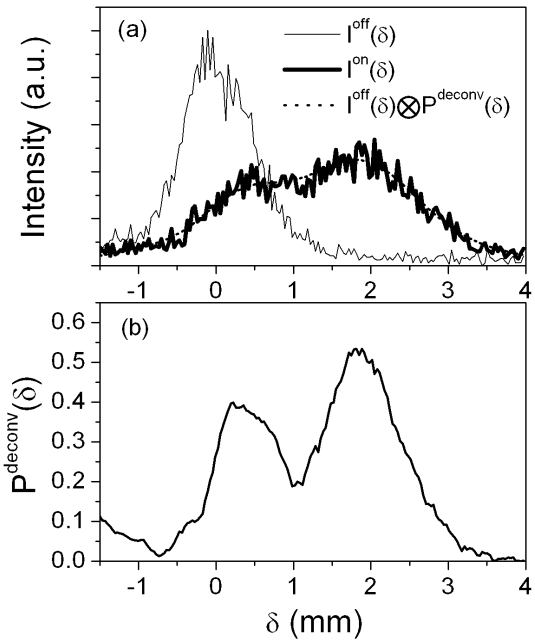

Figure 60: Example of deconvolution using beam profile of the cobalt cluster with 30 atoms. (a)Raw data of profile $I^{off}(\delta)$, $I^{on}(\delta)$, and the profile found from $I^{off}(\delta) \otimes I^{deconv}(\delta)$. (b)$I^{deconv}(\delta)$ found from deconvolution method.

the real peaks in Figure 60b should be sharper than shown there. Because of random noise, the method has to force $P^{deconv}(\delta)$ to be positive definite, by sacrificing fine structure in $I^{on}(\delta)$, as shown in Figure 60a. Hence the profile $I^{off}(\delta) \otimes P^{deconv}(\delta)$ is slightly broader than $I^{on}(\delta)$. This uncertainty can only be reduced by reducing random noise, hence by improving the quality of the raw data $I^{off}(\delta)$ and $I^{on}(\delta)$.

APPENDIX D

ENERGETICS OF IRON GROUP METAL CLUSTERS

The total energy E_t can be written as:

$$E_t = E_s^{single} + E_d^{single} + E_{d-d} + E_{s-s} + E_{d-s}$$

where every term will be explained in the following.

D.1 Single electron energy

Single electron energies are basically interactions between electrons and ionic cores. According to the Born-Oppenheimer approximation, the mass ratio between ions and electrons is so large that to first order approximation, we can study one of them and treat the other as an effective potential.

D.1.1 E_s^{single} single electron energy for 4s electrons

The electrons from $4s$ atomic orbitals become quasi-free when atoms come together in clusters and bulk. These quasi-free electrons form a wide band which is on the order of 20 eV for the bulk.

It is straightforward to get the total energy of a system of N_s electrons:

$$E_s^{single} = \frac{3}{5} E_F^0 \frac{N_s^{5/3}}{N^{2/3}} + E_s^0 N_s,$$

where E_F^0 is the Fermi energy when $N_s = N$, E_s^0 is approximately the single electron energy of s atomic orbital. Note that the bottom of the band is relatively fixed. If we simplify the quasi-free electron model by assuming a constant density of states for the band, we get the total energy:

$$E_s^{single} = \frac{W_s N_s^2}{2N} + E_s^0 N_s. \tag{73}$$

D.1.2 E_d^{single} single electron energies for $3d$ electrons

Unlike 4s electrons, 3d electrons are more tightly bound to the nuclei. When atoms come together in clusters, they also form an energy band but with much smaller width than that of the 4s band. In bulk, the 3d band width is about 5eV. These electrons are more localized than the 4s electrons, especially in clusters, because in clusters the coordination is reduced and the translational symmetry is lost.

The tight-binding model is a useful approximation to describe d electrons. The wave function of single d_i electron can be written as:

$$\psi_k^d(\overrightarrow{r}) = \sum_j a_j \phi_j^d(\overrightarrow{r}),$$

where $\phi_j^d(\overrightarrow{r})$ is the wave function of atomic d orbital of the jth atom. In the case of bulk,

$$a_j = \frac{1}{\sqrt{N}} e^{i\overrightarrow{k}\cdot\overrightarrow{R_j}}$$

where $\overrightarrow{R_j}$ is the position of the ith atom [117]. For cluster, only $\sum_j |a_j|^2 = 1$ is true however.

Assuming a band structure with constant density of states, the energy takes the form:

$$E_d^{single} = \frac{N_d^2}{2}\frac{W_d}{N} - \frac{N_d}{2}W_d + E_d^0 N_d, \tag{74}$$

where E_d^0 is approximately the single electron energy of $3d$ atomic orbital, W_d is the width of $3d$ band.

Note that, the center of 3d bands are more or less fixed in contrast to the fixed bottom of 4s band.

D.2 Electron-electron interaction energy

In the Hartree-Fock approximation, the multielectronic wave function can be represented as a single Slater determinant that combines the single-electron wave functions. If the jth single electron wave function is φ_j, then the electron-electron interaction energy will be [111]

$$E_{e-e} = \sum_{j_1,j_2} C_{j_1 j_2} - \sum_{j_1,j_2} J_{j_1 j_2} \delta\sigma_{j_1}\sigma_{j_2}.$$

The first term is the Coulomb repulsion, where

$$C_{j_1 j_2} = \int \varphi^*_{j_1}(\overrightarrow{r}_1)\varphi^*_{j_2}(\overrightarrow{r}_2)\frac{1}{r_{12}}\varphi_{j_1}(\overrightarrow{r}_1)\varphi_{j_2}(\overrightarrow{r}_2)d\tau_1 d\tau_2.$$

The second term is a quantum effect that comes from indistinguishability of fermions.

$$J_{j_1 j_2} = \int \varphi^*_{j_1}(\overrightarrow{r}_1)\varphi^*_{j_2}(\overrightarrow{r}_2)\frac{1}{r_{12}}\varphi_{j_1}(\overrightarrow{r}_2)\varphi_{j_2}(\overrightarrow{r}_1)d\tau_1 d\tau_2.$$

Note that this term vanishes when $\sigma_{j_1} \neq \sigma_{j_2}$.

D.2.1 E_{d-d} interaction between $3d$ electrons

The polarization of d electrons should be addressed first. It is easy to show that the condition $I_{d-d}/W_{d_i} \gg 1$ is satisfied, the d band will be fully polarized, where

$$I_{d-d} = \sum_{j_1} \int \left|a_{j_1}\right|^4 \phi^{*d}_{j_1}(\overrightarrow{r_1})\phi^{*d}_{j_1}(\overrightarrow{r_2})\frac{1}{r_{12}}\phi^{d}_{j1}(\overrightarrow{r_2})\phi^{d}_{j1}(\overrightarrow{r_1})d\tau_1 d\tau_2.$$

If we consider number of electrons in the $3d$ band as a variable, in the case of more than a half-filled $3d$ band, the interaction energy is:

$$E_{d-d} = (20N_d - 100)I_{d-d}.$$

Ignoring the constant term, we get

$$E_{d-d} = 20N_d I_{d-d}.$$

D.2.2 E_{s-s} interaction between $4s$ electrons

Compared to 3d electrons, 4s electrons are more free-electron like. So the correlation between 4s electrons is less important than that for 3d electrons. We can ignore this part for the first order approximation.

D.2.3 E_{d-s} interaction between d_l and s electrons

This part of interaction is basically the classical Coulomb repulsion. It is referred to as the 4s electron screening on 3d electrons. Symbolically, we can write down the energy as

$$E_{d-s} = \frac{N_s N_d}{2N} I_{d-s},$$

where we assume that interactions between the s orbital and various d orbitals are the same.

D.3 Summary of total energy

The expression of total energy becomes:

$$\begin{aligned} E_t &= \frac{W_s N_s^2}{2N} + E_s^0 N_s + \frac{N_d^2}{2}\frac{W_d}{N} + E_d^0 N_d + 20 N_d I_{d-d} + \frac{N_s N_d}{2N} I_{d-s} \\ &= E_s^0 N_s + \frac{W_s}{2N} N_s^2 + (20 I_{d-d} - \frac{W_d}{2}) N_d + \frac{W_d}{2N} N_d^2 + \frac{I_{d-s}}{2N} N_s N_d. \end{aligned}$$

Define

$$\begin{aligned} \varepsilon_s &= E_s^0 \\ \varepsilon_d &= 20 I_{d-d} - \frac{W_d}{2} \\ G &= I_{d-s} \\ W &= W_s, \end{aligned}$$

and ignore the narrow band width W_d, we get the total energy

$$E_t = \varepsilon_s N_s + \frac{W}{2N} N_s^2 + \varepsilon_d N_d + \frac{G}{2N} N_s N_d,$$

which is actually the Falicov-Kimball model [55] except that we have included the band width of the $4s$ electrons

REFERENCES

[1] Abrahams, E., Anderson, P. W., Licciardello, D. C., and Ramakrishnan, T. V., "Scaling theory of localization - absence of quantum diffusion in 2 dimensions," *Physical Review Letters*, vol. 42, no. 10, pp. 673–676, 1979.

[2] Alonso, J. A., "Electronic and atomic structure, and magnetism of transition-metal clusters," *Chemical Reviews*, vol. 100, no. 2, pp. 637–677, 2000.

[3] Anderson, J. B. and Fenn, J. B., "Velocity distributions in molecular beams from nozzle sources," *Physics of Fluids*, vol. 8, no. 5, pp. 780–, 1965.

[4] Anderson, P. W., "Absence of diffusion in certain random lattices," *Physical Review*, vol. 109, no. 5, pp. 1492–1505, 1958.

[5] Anderson, P. W., "Localized magnetic states in metals," *Physical Review*, vol. 1, no. 1, pp. 41–, 1961.

[6] Anderson, P. W., "Theory of magnetic exchange interactions - exchange in insulators and semiconductors," *Solid State Physics-Advances in Research and Applications*, vol. 14, pp. 99–214, 1963.

[7] Anderson, P. W., "Local moments and localized states," *Science*, vol. 201, no. 4353, pp. 307–316, 1978.

[8] Andriotis, A. N. and Menon, M., "Tight-binding molecular-dynamics study of ferromagnetic clusters," *Physical Review B*, vol. 57, no. 16, pp. 10069–10081, 1998.

[9] Apsel, S. E., Emmert, J. W., Deng, J., and Bloomfield, L. A., "Surface-enhanced magnetism in nickel clusters," *Physical Review Letters*, vol. 76, no. 9, pp. 1441–1444, 1996.

[10] Ballone, P., Milani, P., and Deheer, W. A., "Pseudospin relaxation in ferromagnetic clusters," *Physical Review B*, vol. 44, no. 18, pp. 10350–10353, 1991.

[11] Barden, C. J., Rienstra-Kiracofe, J. C., and Schaefer, H. F., "Homonuclear 3d transition-metal diatomics: A systematic density functional theory study," *Journal of Chemical Physics*, vol. 113, no. 2, pp. 690–700, 2000.

[12] Barth, U. V. and Hedin, L., "Local exchange-correlation potential for spin polarized case .1," *Journal of Physics Part C Solid State Physics*, vol. 5, no. 13, pp. 1629–, 1972.

[13] Bates, C. A. and Wood, P. H., "Magnetic-moments and their interaction in insulating crystals," *Contemporary Physics*, vol. 16, no. 6, pp. 547–560, 1975.

[14] Bauschlicher, C. W. and Ricca, A., "Can all of the fe-2 experimental results be explained?," *Molecular Physics*, vol. 101, no. 1-2, pp. 93–98, 2003.

[15] Bean, C. P. and Livingston, J. D., "Superparamagnetism," *Journal of Applied Physics*, vol. 30, no. 4, pp. S120–S129, 1959.

[16] Bergmann, T., Limberger, H., and Martin, T. P., "Evidence of electronic shell structure in cs-o clusters," *Physical Review Letters*, vol. 60, no. 17, pp. 1767–1770, 1988.

[17] Berkowitz, J., *Photoabsorption, photoionization, and photoelectron spectroscopy*. New York: Academic Press, 1979.

[18] Berry, M. V. and Tabor, M., "Level clustering in regular spectrum," *Proceedings of the Royal Society of London Series a-Mathematical Physical and Engineering Sciences*, vol. 356, no. 1686, pp. 375–394, 1977.

[19] Bertsch, G., Onishi, N., and Yabana, K., "Magnetization of ferromagnetic clusters," *Zeitschrift Fur Physik D-Atoms Molecules and Clusters*, vol. 34, no. 3, pp. 213–217, 1995.

[20] Bertsch, G. F. and Yabana, K., "Cold cluster ferromagnetism," *Physical Review A*, vol. 49, no. 3, pp. 1930–1932, 1994.

[21] Billas, I. M. L., Chatelain, A., and Deheer, W. A., "Magnetism from the atom to the bulk in iron, cobalt, and nickel clusters," *Science*, vol. 265, no. 5179, pp. 1682–1684, 1994.

[22] Billas, I. M. L., Chatelain, A., and deHeer, W. A., "Magnetism of fe, co and ni clusters in molecular beams," *Journal of Magnetism and Magnetic Materials*, vol. 168, no. 1-2, pp. 64–84, 1997.

[23] Billas, I., *Magnetism of iron, cobalt and nickel clusters studied in molecular beams*. PhD thesis, EPFL, 1995.

[24] Bloch, F. *Z. Physik*, vol. 57, p. 545, 1929.

[25] Bloomfield, L. A., "The magnetic-behavior of free transition-metal and rare-earth clusters," *Abstracts of Papers of the American Chemical Society*, vol. 204, pp. 26–PHYS, 1992. Part 2.

[26] Bonin, K. D., *Electric-dipole polarizabilities of atoms, molecules, and clusters*. Singapore: River Edge, NJ : World Scientific, 1997. English.

[27] Brack, M., "The physics of simple metal-clusters - self-consistent jellium model and semiclassical approaches," *Reviews of Modern Physics*, vol. 65, no. 3, pp. 677–732, 1993. Part 1.

[28] Brown, P. J., Capellmann, H., Deportes, J., Givord, D., and Ziebeck, K. R. A., "Spatial correlation of magnetization in the paramagnetic phases of iron and nickel," *Journal of Magnetism and Magnetic Materials*, vol. 31-4, no. FEB, pp. 295–296, 1983.

[29] Brown, W. F., "Thermal fluctuations of a single-domain particle," *Physical Review*, vol. 1, no. 5, pp. 1677–, 1963.

[30] Bucher, J. P., Douglass, D. C., and Bloomfield, L. A., "Magnetic-properties of free cobalt clusters," *Physical Review Letters*, vol. 66, no. 23, pp. 3052–3055, 1991.

[31] Capellmann, H., *Metallic magnetism*. Berlin ; New York: Springer-Verlag, 1987.

[32] Castro, M., Jamorski, C., and Salahub, D. R., "Structure, bonding, and magnetism of small fe-n, co-n, and ni-n, clusters, n<=5," *Chemical Physics Letters*, vol. 271, no. 1-3, pp. 133–142, 1997.

[33] Cohen-Tannoudji, C. D. B. L. F., "Quantum mechanics. vol. 2 uniform title: Mecanique quantique. english," 1977. NetLibrary, Inc.

[34] Collings, B. A., Amrein, A. H., Rayner, D. M., and Hackett, P. A., "On the vibrational temperature of metal cluster beams - a time-resolved thermionic emission study," *Journal of Chemical Physics*, vol. 99, no. 5, pp. 4174–4180, 1993.

[35] Cox, A. J., Douglass, D. C., Louderback, J. G., Spencer, A. M., and Bloomfield, L. A., "Magnetic-properties of rare-earth clusters," *Zeitschrift Fur Physik D-Atoms Molecules and Clusters*, vol. 26, no. 1-4, pp. 319–321, 1993.

[36] Cox, A. J., Louderback, J. G., Apsel, S. E., and Bloomfield, L. A., "Magnetism in 4d-transition metal-clusters," *Physical Review B*, vol. 49, no. 17, pp. 12295–12298, 1994.

[37] Cox, A. J., Louderback, J. G., and Bloomfield, L. A., "Experimental-observation of magnetism in rhodium clusters," *Physical Review Letters*, vol. 71, no. 6, pp. 923–926, 1993.

[38] Cox, D. M., Trevor, D. J., Whetten, R. L., Rohlfing, E. A., and Kaldor, A., "Magnetic-behavior of free-iron and iron-oxide clusters," *Physical Review B*, vol. 32, no. 11, pp. 7290–7298, 1985.

[39] Curie, P. *Ann. de Chim. et de Phys.*, vol. 5, p. 289, 1895.

[40] Cyrot, M., "Phase transition in hubbard model," *Physical Review Letters*, vol. 25, no. 13, pp. 871–, 1970.

[41] Deheer, W. A., "The physics of simple metal-clusters - experimental aspects and simple-models," *Reviews of Modern Physics*, vol. 65, no. 3, pp. 611–676, 1993. Part 1.

[42] Deheer, W. A. and Milani, P., "Photoionization of mass-selected kn+ ions - a test for the ionization scaling law - comment," *Physical Review Letters*, vol. 65, no. 26, pp. 3356–3356, 1990.

[43] Deheer, W. A. and Milani, P., "Large ion volume time-of-flight mass-spectrometer with position-sensitive and velocity-sensitive detection capabilities for cluster beams," *Review of Scientific Instruments*, vol. 62, no. 3, pp. 670–677, 1991.

[44] Deheer, W. A., Milani, P., and Chatelain, A., "Nonjellium-to-jellium transition in aluminum cluster polarizabilities," *Physical Review Letters*, vol. 63, no. 26, pp. 2834–2836, 1989.

[45] Deheer, W. A., Milani, P., and Chatelain, A., "Spin relaxation in small free iron clusters," *Physical Review Letters*, vol. 65, no. 4, pp. 488–491, 1990.

[46] Dirac, P. A. M., "On the theory of quantum mechanics," *Proceedings of the Royal Society of London Series a-Containing Papers of a Mathematical and Physical Character*, vol. 112, no. 762, pp. 661–677, 1926.

[47] Dirac, P. A. M., "Quantum mechanics of many-electron systems," *Proceedings of the Royal Society of London Series a-Containing Papers of a Mathematical and Physical Character*, vol. 123, no. 792, pp. 714–733, 1929.

[48] Douglass, D. C., Bucher, J. P., and Bloomfield, L. A., "Magic numbers in the magnetic-properties of gadolinium clusters," *Physical Review Letters*, vol. 68, no. 11, pp. 1774–1777, 1992.

[49] Douglass, D. C., Cox, A. J., Bucher, J. P., and Bloomfield, L. A., "Magnetic-properties of free cobalt and gadolinium clusters," *Physical Review B*, vol. 47, no. 19, pp. 12874–12889, 1993.

[50] Ederer, C., Komelj, M., and Fahnle, M., "Magnetism in systems with various dimensionalities: A comparison between fe and co," *Physical Review B*, vol. 68, no. 5, 2003. 052402.

[51] Elsasser, C., Krimmel, H., Fahnle, M., Louie, S. G., and Chan, C. T., "Ab initio study of iron and iron hydride: Iii. vibrational states of h isotopes in fe, cr and ni," *Journal of Physics-Condensed Matter*, vol. 10, no. 23, pp. 5131–5146, 1998.

[52] Elsasser, C., Zhu, J., Louie, S. G., Fahnle, M., and Chan, C. T., "Ab initio study of iron and iron hydride: I. cohesion, magnetism and electronic structure of cubic fe and feh," *Journal of Physics-Condensed Matter*, vol. 10, no. 23, pp. 5081–5111, 1998.

[53] Elsasser, C., Zhu, J., Louie, S. G., Meyer, B., Fahnle, M., and Chan, C. T., "Ab initio study of iron and iron hydride: Ii. structural and magnetic properties of close-packed fe and feh," *Journal of Physics-Condensed Matter*, vol. 10, no. 23, pp. 5113–5129, 1998.

[54] Falicov, L. M. and Harris, R. A., "2-electron homopolar molecule - a test for spin-density waves and charge-density waves," *Journal of Chemical Physics*, vol. 51, no. 8, pp. 3153–, 1969.

[55] Falicov, L. M. and Kimball, J. C., "Simple model for semiconductor-metal transitions - smb6 and transition-metal oxides," *Physical Review Letters*, vol. 22, no. 19, pp. 997–, 1969.

[56] Fan, H. J., Liu, C. W., and Liao, M. S., "Geometry, electronic structure and magnetism of small co-n (n=2-8) clusters," *Chemical Physics Letters*, vol. 273, no. 5-6, pp. 353–359, 1997.

[57] FERMI, E. *REND ACCAD NAZ LINCE*, vol. 6, p. 602, 1927.

[58] Freund, H. J. and Bauer, S. H., "Homogeneous nucleation in metal vapors .2. dependence of heat of condensation on cluster size," *Journal of Physical Chemistry*, vol. 81, no. 10, pp. 994–1000, 1977.

[59] Fuggle, J. C. S. G. A. A. J. W., *Narrow-band phenomena–influence of electrons with both band and localized character*. NATO ASI series. Series B, Physics ;; vol. 184; Variation: NATO ASI series.; Series B,; Physics ;; v. 184., New York: Plenum Press, 1988.

[60] Gantefor, G. and Eberhardt, W., "Localization of 3d and 4d electrons in small clusters: The "roots" of magnetism," *Physical Review Letters*, vol. 76, no. 26, pp. 4975–4978, 1996.

[61] Gerion, D., Hirt, A., Billas, I. M. L., Chatelain, A., and de Heer, W. A., "Experimental specific heat of iron, cobalt, and nickel clusters studied in a molecular beam," *Physical Review B*, vol. 62, no. 11, pp. 7491–7501, 2000.

[62] Gittlema.Ji, Abeles, B., and Bozowski, S., "Superparamagnetism and relaxation effects in granular ni-sio2 and ni-al2o3 films," *Physical Review B*, vol. 9, no. 9, pp. 3891–3897, 1974.

[63] Goncalvesdasilva, C. E. T. and Falicov, L. M., "Theory of valence mixing for rare-earth compounds," *Solid State Communications*, vol. 17, no. 12, pp. 1521–1524, 1975.

[64] Guirado-Lopez, R. A., Dorantes-Davila, J., and Pastor, G. M., "Orbital magnetism in transition-metal clusters: From hund's rules to bulk quenching," *Physical Review Letters*, vol. 90, no. 22, 2003. 226402.

[65] Guyon, P. M. and Berkowit.J, "Interpretation of photoionization threshold behavior," *Journal of Chemical Physics*, vol. 54, no. 4, pp. 1814–, 1971.

[66] Hales, D. A., Su, C. X., Lian, L., and Armentrout, P. B., "Collision-induced dissociation of co-n(+) (n=2-18) with xe - bond-energies of cationic and neutral cobalt clusters, dissociation pathways, and structures," *Journal of Chemical Physics*, vol. 100, no. 2, pp. 1049–1057, 1994.

[67] Halperin, W. P., "Quantum size effects in metal particles," *Reviews of Modern Physics*, vol. 58, no. 3, pp. 533–606, 1986.

[68] Hamamoto, N., Onishi, N., and Bertsch, G., "Magnetic properties of an ensemble of rotating ferromagnetic clusters," *Physical Review B*, vol. 61, no. 2, pp. 1336–1350, 2000.

[69] Heisenberg, W. *Z. Physik*, vol. 49, p. 619, 1928.

[70] Hihara, T., Pokrant, S., and Becker, J. A., "Magnetic moments and chemical bonding in isolated bincom clusters," *Chemical Physics Letters*, vol. 294, no. 4-5, pp. 357–362, 1998.

[71] Hill, T. L., "Thermodynamics of small systems," *Journal of Chemical Physics*, vol. 36, no. 12, pp. 3182–, 1962.

[72] Hohenberg, P. and Kohn, W., "Inhomogeneous electron gas," *Physical Review*, vol. 136, no. 3B, p. B864, 1964. Copyright (C) 2007 The American Physical Society.

[73] Homer, M. L., Persson, J. L., Honea, E. C., and Whetten, R. L., "Ionization energies and stabilities of nan, n less-than 25 - shell structure from measurements on cold clusters," *Zeitschrift Fur Physik D-Atoms Molecules and Clusters*, vol. 22, no. 1, pp. 441–447, 1991.

[74] Hubbard, J., "Electron correlations in narrow energy bands," *Proceedings of the Royal Society of London Series a-Mathematical and Physical Sciences*, vol. 276, no. DEC, pp. 238–, 1963.

[75] Hubbard, J., "Magnetism of iron," *Physical Review B*, vol. 19, no. 5, pp. 2626–2636, 1979.

[76] Hubbard, J., "Magnetism of iron .2," *Physical Review B*, vol. 20, no. 11, pp. 4584–4595, 1979.

[77] Hurwitz, H. PhD thesis, Harvard University, 1941.

[78] Jackson, J. D., *Classical electrodynamics*. New York: Wiley, 1999.

[79] Jahn, H. A., "Stability of polyatomic molecules in degenerate electronic states ii - spin degeneracy," *Proceedings of the Royal Society of London Series a-Mathematical and Physical Sciences*, vol. 164, no. A916, pp. 0117–0131, 1938.

[80] Jahn, H. A. and Teller, E., "Stability of polyatomic molecules in degenerate electronic states. i. orbital degeneracy," *Proceedings of the Royal Society of London Series a-Mathematical and Physical Sciences*, vol. 161, no. A905, pp. 220–235, 1937.

[81] Jansson, P. A., *Deconvolution : with applications in spectroscopy*. New York: Academic Press, 1984. ill. ; 23 cm.

[82] Jensen, P. J. and Bennemann, K. H., "Theory for the magnetic-properties of a free metal cluster ensemble," *Berichte Der Bunsen-Gesellschaft-Physical Chemistry Chemical Physics*, vol. 96, no. 9, pp. 1233–1236, 1992.

[83] Jensen, P. J. and Bennemann, K. H., "Theory for the atomic shell structure of the cluster magnetic-moment and magnetoresistance of a cluster ensemble," *Zeitschrift Fur Physik D-Atoms Molecules and Clusters*, vol. 35, no. 4, pp. 273–278, 1995.

[84] Kappes, M. M., Schar, M., Rothlisberger, U., Yeretzian, C., and Schumacher, E., "Sodium cluster ionization-potentials revisited - higher-resolution measurements for nax (x-less-than-23) and their relation to bonding models," *Chemical Physics Letters*, vol. 143, no. 3, pp. 251–258, 1988.

[85] Kasuya, T., "A theory of metallic ferromagnetism and antiferromagnetism on zeners model," *Progress of Theoretical Physics*, vol. 16, no. 1, pp. 45–57, 1956.

[86] Khanna, S. N. and Linderoth, S., "Magnetic-behavior of clusters of ferromagnetic transition-metals," *Physical Review Letters*, vol. 67, no. 6, pp. 742–745, 1991.

[87] Kittel, C., *Introduction to solid state physics*. Hoboken, NJ: Wiley, 8 ed., 2005.

[88] Knickelbein, M. B., "Electric dipole polarizabilities of ni12-58," *Journal of Chemical Physics*, vol. 115, no. 13, pp. 5957–5964, 2001.

[89] Knickelbein, M. B., "Experimental observation of superparamagnetism in manganese clusters," *Physical Review Letters*, vol. 86, no. 23, pp. 5255–5257, 2001.

[90] Knickelbein, M. B., "Magnetic ordering in manganese clusters," *Physical Review B*, vol. 70, no. 1, 2004. 014424.

[91] Knickelbein, M. B., "Magnetic ordering in clusters of the group 3 transition elements: Sc-n, y-n, and la-n," *Physical Review B*, vol. 71, no. 18, 2005. 184442.

[92] Kohn, W. and Sham, L. J., "Self-consistent equations including exchange and correlation effects," *Physical Review*, vol. 140, no. 4A, p. A1133, 1965. Copyright (C) 2007 The American Physical Society.

[93] Kolodney, E. and Amirav, A., "Aerodynamical acceleration and rotational-vibrational temperatures in seeded supersonic molecular-beams," *Chemical Physics*, vol. 82, no. 3, pp. 269–283, 1983.

[94] Korecki, J. and Krop, K., "Superparamagnetism of very small cobalt particles studied by mossbauer-spectroscopy," *Surface Science*, vol. 106, no. 1-3, pp. 444–452, 1981.

[95] Korenman, V., Murray, J. L., and Prange, R. E., "Local-band theory of itinerant ferromagnetism .1. fermi-liquid theory," *Physical Review B*, vol. 16, no. 9, pp. 4032–4047, 1977.

[96] Korenman, V., Murray, J. L., and Prange, R. E., "Local-band theory of itinerant ferromagnetism .2. spin-waves," *Physical Review B*, vol. 16, no. 9, pp. 4048–4057, 1977.

[97] Korenman, V., Murray, J. L., and Prange, R. E., "Local-band theory of itinerant ferromagnetism .3. nonlinear landau-lifshitz equations," *Physical Review B*, vol. 16, no. 9, pp. 4058–4062, 1977.

[98] Kresin, V. Z. and Ovchinnikov, Y. N., "Shell structure and strengthening of superconducting pair correlation in nanoclusters," *Physical Review B*, vol. 74, no. 2, 2006. 024514.

[99] Langevin, P., "Magnetism and theory of electrons," *Annales De Chimie Et De Physique*, vol. 5, pp. 70–127, 1905.

[100] Langreth, D. C. and Mehl, M. J., "Beyond the local-density approximation in calculations of ground-state electronic-properties," *Physical Review B*, vol. 28, no. 4, pp. 1809–1834, 1983.

[101] Langreth, D. C. and Perdew, J. P., "Theory of nonuniform electronic systems .1. analysis of the gradient approximation and a generalization that works," *Physical Review B*, vol. 21, no. 12, pp. 5469–5493, 1980.

[102] Li, Z. Q. and Gu, B. L., "Electronic-structure calculations of cobalt clusters," *Physical Review B*, vol. 47, no. 20, pp. 13611–13614, 1993.

[103] Lichtenstein, A. I., Katsnelson, M. I., and Kotliar, G., "Finite-temperature magnetism of transition metals: An ab initio dynamical mean-field theory," *Physical Review Letters*, vol. 8706, no. 6, 2001. 067205.

[104] Limberger, H. G. and Martin, T. P., "Photoionization spectra of cesium and cesium oxide clusters," *Journal of Chemical Physics*, vol. 90, no. 6, pp. 2979–2991, 1989.

[105] Liu, F. Y. and Armentrout, P. B., "Guided ion-beam studies of the kinetic-energy-dependent reactions of co-n(+) (n=2-16) with d-2: Cobalt cluster-deuteride bond energies," *Journal of Chemical Physics*, vol. 122, no. 19, 2005. 194320.

[106] Liu, F. Y., Li, F. X., and Armentrout, P. B., "Guided ion-beam studies of the reactions of co-n(+) (n=2-20) with o-2: Cobalt cluster-oxide and -dioxide bond energies," *Journal of Chemical Physics*, vol. 123, no. 6, 2005. 064304.

[107] Liu, S. R., Zhai, H. J., and Wang, L. S., "Electronic and structural evolution of co-n clusters (n=1-108) by photoelectron spectroscopy," *Physical Review B*, vol. 6415, no. 15, 2001. 153402.

[108] Maiti, A. and Falicov, L. M., "Stern-gerlach dynamics of magnetic clusters," *Physical Review B*, vol. 48, no. 18, pp. 13596–13601, 1993.

[109] Makov, G., Nitzan, A., and Brus, L. E., "On the ionization-potential of small metal and dielectric particles," *Journal of Chemical Physics*, vol. 88, no. 8, pp. 5076–5085, 1988.

[110] Marsman, M. and Hafner, J., "Broken symmetries in the crystalline and magnetic structures of gamma-iron," *Physical Review B*, vol. 66, no. 22, 2002. 224409.

[111] Martin, D. H., *Magnetism in solids*. Cambridge: M.I.T. Press, 1967. Bibliography: p. 437-443.

[112] Martin, T. P., "Cluster beam chemistry - from atoms to solids," *Angewandte Chemie-International Edition in English*, vol. 25, no. 3, pp. 197–211, 1986.

[113] Martin, T. P., "Shells of atoms," *Physics Reports-Review Section of Physics Letters*, vol. 273, no. 4, pp. 199–241, 1996.

[114] Martin, T. P., "From atoms to solids," *Solid State Ionics*, vol. 131, no. 1-2, pp. 3–12, 2000.

[115] Mattis, D. C., *The theory of magnetism*. Berlin ; New York: Springer-Verlag, 1988.

[116] Merikoski, J., Timonen, J., Manninen, M., and Jena, P., "Ferromagnetism in small clusters," *Physical Review Letters*, vol. 66, no. 7, pp. 938–941, 1991.

[117] Mermin, N. W. A. N. D., *Solid state physics*. 1976.

[118] Milani, P., "Rotational coupling effects on the spin relaxation of free ferromagnetic clusters," *Zeitschrift Fur Physik D-Atoms Molecules and Clusters*, vol. 28, no. 2, pp. 163–167, 1993.

[119] Milani, P. and Deheer, W. A., "Relative thermometer for neutral clusters produced in laser-vaporization sources," *Physical Review B*, vol. 44, no. 15, pp. 8346–8348, 1991.

[120] Milani, P., Moullet, I., and Deheer, W. A., "Experimental and theoretical electric-dipole polarizabilities of al and al2," *Physical Review A*, vol. 42, no. 9, pp. 5150–5154, 1990.

[121] Mook, H. A., "Neutron-scattering studies of the high-temperature spin dynamics of ferromagnetic materials," *Journal of Magnetism and Magnetic Materials*, vol. 31-4, no. FEB, pp. 305–308, 1983.

[122] Mook, H. A., Lynn, J. W., and Nicklow, R. M., "Temperature-dependence of magnetic excitations in nickel," *Physical Review Letters*, vol. 30, no. 12, pp. 556–559, 1973.

[123] Mook, H. A. and Nicklow, R. M., "Neutron-scattering investigation of magnetic excitations in iron," *Physical Review B*, vol. 7, no. 1, pp. 336–342, 1973.

[124] Mook, H. A. and Paul, D. M., "Neutron-scattering measurement of the spin-wave spectra for nickel," *Physical Review Letters*, vol. 54, no. 3, pp. 227–229, 1985.

[125] Moran, S., Ederer, C., and Fahnle, M., "Ab initio electron theory for magnetism in fe: Pressure dependence of spin-wave energies, exchange parameters, and curie temperature," *Physical Review B*, vol. 67, no. 1, 2003. 012407.

[126] Morenzin, J., Kietzmann, H., Bechthold, P. S., Gantefor, G., and Eberhardt, W., "Localization and bandwidth of the 3d-orbitals in magnetic ni and co clusters," *Pure and Applied Chemistry*, vol. 72, no. 11, pp. 2149–2157, 2000.

[127] Moriya, T., "Recent progress in the theory of itinerant electron magnetism," *Journal of Magnetism and Magnetic Materials*, vol. 14, no. 1, pp. 1–46, 1979.

[128] Moriya, T., *Spin fluctuations in itinerant electron magnetism*. Berlin ; New York: Springer-Verlag, 1985.

[129] Moro, R., Xu, X. S., Yin, S. Y., and de Heer, W. A., "Ferroelectricity in free niobium clusters," *Science*, vol. 300, no. 5623, pp. 1265–1269, 2003.

[130] Moro, R., Yin, S. Y., Xu, X. S., and de Heer, W. A., "Spin uncoupling in free nb clusters: Support for nascent superconductivity," *Physical Review Letters*, vol. 93, no. 8, 2004. 086803.

[131] Morup, S., Topsoe, H., and Clausen, B. S., "Magnetic-properties of microcrystals studied by mossbauer-spectroscopy," *Physica Scripta*, vol. 25, no. 6, pp. 713–719, 1982.

[132] Neel, L. *Ann. Geophys.*, vol. 5, p. 99, 1949.

[133] Oliver, G. L. and Perdew, J. P., "Spin-density gradient expansion for the kinetic-energy," *Physical Review A*, vol. 20, no. 2, pp. 397–403, 1979.

[134] Ovchinnikov, Y. N. and Kresin, V. Z., "Giant strengthening of superconducting pairing in metallic nanoclusters," *European Physical Journal B*, vol. 45, no. 1, pp. 5–7, 2005.

[135] Ovchinnikov, Y. N. and Kresin, V. Z., "Strong pair correlation in small metallic nanoclusters: the energy spectrum," *European Physical Journal B*, vol. 47, no. 3, pp. 333–336, 2005.

[136] OâĂŹHandley, R. C., *Modern magnetic materials : principles and applications*. New York: Wiley, 2000.

[137] Pant, M. M. and Rajagopa.Ak, "Theory of inhomogeneous magnetic electron-gas," *Solid State Communications*, vol. 10, no. 12, pp. 1157–, 1972.

[138] Parks, E. K., Klots, T. D., Winter, B. J., and Riley, S. J., "Reactions of cobalt clusters with water and ammonia - implications for cluster structure," *Journal of Chemical Physics*, vol. 99, no. 8, pp. 5831–5839, 1993.

[139] Parks, R. D., *Valence instabilities and related narrow-band phenomena : [proceedings of an international conference on valence instabilities and related narrow-band phenomena held at the University of Rochester, Rochester, New York]*. New York: Plenum Press, 1977. ill. ; 26 cm.

[140] Pastor, G. M., Dorantesdavila, J., and Bennemann, K. H., "Size and structural dependence of the magnetic-properties of small 3d-transition-metal clusters," *Physical Review B*, vol. 40, no. 11, pp. 7642–7654, 1989.

[141] Pauly, H., *Atom, molecule, and cluster beams*. Springer series on atomic, optical, and plasma physics, Berlin ; New York: Springer, 2000.

[142] Pechukas, P., "Distribution of energy eigenvalues in the irregular spectrum," *Physical Review Letters*, vol. 51, no. 11, pp. 943–946, 1983.

[143] Perdew, J. P., "Density-functional approximation for the correlation-energy of the inhomogeneous electron-gas," *Physical Review B*, vol. 33, no. 12, pp. 8822–8824, 1986. Part 2.

[144] Perdew, J. P., "Energetics of charged metallic particles - from atom to bulk solid," *Physical Review B*, vol. 37, no. 11, pp. 6175–6180, 1988.

[145] Perdew, J. P. and Yue, W., "Accurate and simple density functional for the electronic exchange energy - generalized gradient approximation," *Physical Review B*, vol. 33, no. 12, pp. 8800–8802, 1986. Part 2.

[146] Pereiro, M., Man'kovsky, S., Baldomir, D., Iglesias, M., Mlynarski, P., Valladares, M., Suarez, D., Castro, M., and Arias, J. E., "Model potential nonlocal density functional calculations of small cobalt clusters, co-n,n <= 5," *Computational Materials Science*, vol. 22, no. 1-2, pp. 118–122, 2001.

[147] Persson, J. L., Whetten, R. L., Cheng, H. P., and Berry, R. S., "Evidence for quantized electronic level structure for 100-1300 electrons in metal-atomic clusters," *Chemical Physics Letters*, vol. 186, no. 2-3, pp. 215–222, 1991.

[148] Pokrant, S., "Evidence for adiabatic magnetization of cold dy-n clusters," *Physical Review A*, vol. 62, no. 5, 2000. 051201.

[149] Pokrant, S. and Becker, J. A., "Magnetization curves of dy-n clusters," *European Physical Journal D*, vol. 16, no. 1-3, pp. 165–168, 2001.

[150] Pokrant, S., Herwig, C., Hihara, T., and Becker, J. A., "Electronic spin-spin coupling in rare earth doped semiconductor and semimetal clusters," *European Physical Journal D*, vol. 9, no. 1-4, pp. 509–512, 1999. Sp. Iss. SI.

[151] Postnikov, A. V., Entel, P., and Soler, J. M., "Density functional simulation of small fe nanoparticles," *European Physical Journal D*, vol. 25, no. 3, pp. 261–270, 2003.

[152] Prange, R. E. and Korenman, V., "Local-band theory of itinerant ferromagnetism .4. equivalent heisenberg-model," *Physical Review B*, vol. 19, no. 9, pp. 4691–4697, 1979.

[153] Prange, R. E. and Korenman, V., "Local-band theory of itinerant ferromagnetism .5. statistical-mechanics of spin-waves," *Physical Review B*, vol. 19, no. 9, pp. 4698–4702, 1979.

[154] Ramsey, N., *Molecular beams.* Oxford: Clarendon Press, 1956.

[155] Reuse, F. A. and Khanna, S. N., "Geometry, electronic-structure, and magnetism of small ni-n (n=2-6, 8, 13) clusters," *Chemical Physics Letters*, vol. 234, no. 1-3, pp. 77–81, 1995.

[156] Rodriguez-Lopez, J. L., Aguilera-Granja, F., Michaelian, K., and Vega, A., "Structure and magnetism of cobalt clusters," *Physical Review B*, vol. 67, no. 17, 2003. 174413.

[157] Rohlfing, E. A., Cox, D. M., Kaldor, A., and Johnson, K. H., "Photoionization spectra and electronic-structure of small iron clusters," *Journal of Chemical Physics*, vol. 81, no. 9, pp. 3846–3851, 1984.

[158] Ruderman, M. A. and Kittel, C., "Indirect exchange coupling of nuclear magnetic moments by conduction electrons," *Physical Review*, vol. 96, no. 1, pp. 99–102, 1954.

[159] Sakurai, J. J. T. S. F., *Modern quantum mechanics.* Menlo Park, Calif.: Benjamin/Cummings, 1985. ill. ; 25 cm.

[160] Saunders, W. A., Clemenger, K., Deheer, W. A., and Knight, W. D., "Photoionization and shell structure of potassium clusters," *Physical Review B*, vol. 32, no. 2, pp. 1366–1368, 1985.

[161] Scoles, G., *Atomic and Molecular Beam Methods.* New York: Oxford University Press, 1988.

[162] Selby, K., Vollmer, M., Masui, J., Kresin, V., Deheer, W. A., and Knight, W. D., "Surface plasma resonances in free metal-clusters," *Physical Review B*, vol. 40, no. 8, pp. 5417–5427, 1989.

[163] Shastry, B. S., Edwards, D. M., and Young, A. P., "The paramagnetic state of bcc iron," *Journal of Physics C-Solid State Physics*, vol. 14, no. 22, pp. L665–L670, 1981.

[164] Sipr, O., Kosuth, M., and Ebert, H., "Magnetic structure of free iron clusters compared to iron crystal surfaces," *Physical Review B*, vol. 70, no. 17, 2004. 174423.

[165] Slater, J. C., "Ferromagnetism and the band theory," *Reviews of Modern Physics*, vol. 25, no. 1, pp. 199–210, 1953.

[166] Smith, J. L. and Kmetko, E. A., "Magnetism or bonding - a nearly periodic table of transition-elements," *Journal of the Less-Common Metals*, vol. 90, no. 1, pp. 83–88, 1983.

[167] Staunton, J., Gyorffy, B. L., Pindor, A. J., Stocks, G. M., and Winter, H., "The disordered local moment picture of itinerant magnetism at finite temperatures," *Journal of Magnetism and Magnetic Materials*, vol. 45, no. 1, pp. 15–22, 1984.

[168] Stearns, M. B., "Why is iron magnetic," *Physics Today*, vol. 31, no. 4, pp. 34–39, 1978.

[169] Stoner, E. C., "The internal energy of ferromagnetics," *Philosophical Transactions of the Royal Society of London Series a-Mathematical and Physical Sciences*, vol. 235, pp. 165–193, 1936.

[170] Sugar, J. and Corliss, C., "Atomic-energy levels of the iron-period elements - potassium through nickel," *Journal of Physical and Chemical Reference Data*, vol. 14, pp. 1–, 1985. Suppl. 2.

[171] Tatewaki, H., Tomonari, M., and Nakamura, T., "The band-structure of small iron clusters from fe1 to fe6," *Journal of Chemical Physics*, vol. 88, no. 10, pp. 6419–6430, 1988.

[172] Thomas, L. H., "The calculation of atomic fields," *Proceedings of the Cambridge Philosophical Society*, vol. 23, pp. 542–548, 1927.

[173] Tiago, M. L., Zhou, Y. K., Alemany, M. M. G., Saad, Y., and Chelikowsky, J. R., "Evolution of magnetism in iron from the atom to the bulk," *Physical Review Letters*, vol. 97, no. 14, 2006. 147201.

[174] Tomonari, M. and Tatewaki, H., "The ground, excited, and negatively ionized states of fe-2," *Journal of Chemical Physics*, vol. 88, no. 3, pp. 1828–1836, 1988.

[175] Townes, C. H. and Schawlow, A. L., *Microwave spectroscopy*. New York: Dover Publications, 1975.

[176] Van Vleck, J. H., "Nonorthogonality and ferromagnetism," *Physical Review*, vol. 49, no. 3, pp. 0232–0240, 1936.

[177] Van Vleck, J. H. and Sherman, A., "The quantum theory of valence," *Reviews of Modern Physics*, vol. 7, no. 3, pp. 0167–0228, 1935.

[178] Vanvleck, J. H., "A survey of the theory of ferromagnetism," *Reviews of Modern Physics*, vol. 17, no. 1, pp. 27–47, 1945.

[179] Vanvleck, J. H., "The coupling of angular momentum vectors in molecules," *Reviews of Modern Physics*, vol. 23, no. 3, pp. 213–227, 1951.

[180] Vanvleck, J. H., "Models of exchange coupling in ferromagnetic media," *Reviews of Modern Physics*, vol. 25, no. 1, pp. 220–228, 1953.

[181] Vanvleck, J. H., "Quantum-mechanics - key to understanding magnetism," *Reviews of Modern Physics*, vol. 50, no. 2, pp. 181–189, 1978.

[182] Visuthikraisee, V. and Bertsch, G. F., "Spin-rotation coupling in ferromagnetic clusters," *Physical Review A*, vol. 54, no. 6, pp. 5104–5109, 1996.

[183] von Issendorff, B. and Cheshnovsky, O., "Metal to insulator transitions in clusters," *Annual Review of Physical Chemistry*, vol. 56, pp. 549–580, 2005.

[184] Wang, L. S., Cheng, H. S., and Fan, J. W., "Photoelectron-spectroscopy of size-selected transition-metal clusters - fe-n(-)," *Journal of Chemical Physics*, vol. 102, no. 24, pp. 9480–9493, 1995.

[185] Watanabe, K., "Photoionization and total absorption cross section of gases .1. ionization potentials of several molecules - cross sections of nh3 and no," *Journal of Chemical Physics*, vol. 22, no. 9, pp. 1564–1570, 1954.

[186] Weiss, P., "The specific heat and molecular field of ferromagnetic substances," *Comptes Rendus Hebdomadaires Des Seances De L Academie Des Sciences*, vol. 145, pp. 1417–1419, 1907.

[187] Wigner, E., "On the interaction of electrons in metals," *Physical Review*, vol. 46, no. 11, pp. 1002–1011, 1934.

[188] Wohlfarth, E. P., "The theoretical and experimental status of the collective electron theory of ferromagnetism," *Reviews of Modern Physics*, vol. 25, no. 1, pp. 211–219, 1953.

[189] Wohlfarth, E. P., *Ferromagnetic materials*. Amsterdam: Elsevier North-Holland, 1980.

[190] Wolff, P. A., "Localized moments in metals," *Physical Review*, vol. 124, no. 4, pp. 1030–, 1961.

[191] Xiao, G., Liou, S. H., Levy, A., Taylor, J. N., and Chien, C. L., "Magnetic relaxation in fe-(sio_{2}) granular films," *Physical Review B*, vol. 34, no. 11, p. 7573, 1986.

[192] Xu, X. S., Yin, S. Y., Moro, R., and de Heer, W. A., "Magnetic moments and adiabatic magnetization of free cobalt clusters," *Physical Review Letters*, vol. 95, no. 23, 2005. 237209.

[193] Yang, S. and Knickelbein, M. B., "Photoionization studies of transition-metal clusters - ionization-potentials for fen and con," *Journal of Chemical Physics*, vol. 93, no. 3, pp. 1533–1539, 1990.

[194] Yin, S. G., Xu, X. S., Moro, R., and de Heer, W. A., "Measurement of magnetic moments of free binmnm clusters," *Physical Review B*, vol. 72, no. 17, 2005. 174410.

[195] Yin, S. Y., Xu, X. S., Moro, R., and De Heer, W. A. vol. to be published, 2006.

[196] Yin, S., Moro, R., Xu, X., and de Heer, W. A., "Anomalous magnetic enhancement in mn doped co clusters," *to be published*, p. 1, 2006.

[197] Yoshida, H., Terasaki, A., Kobayashi, K., Tsukada, M., and Kondow, T., "Spin-polarized electronic-structure of cobalt cluster anions studied by photoelectron-spectroscopy," *Journal of Chemical Physics*, vol. 102, no. 15, pp. 5960–5965, 1995.

[198] Yosida, K., "Magnetic properties of cu-mn alloys," *Physical Review*, vol. 1, no. 5, pp. 893–898, 1957.

[199] Zener, C., "Non-adiabatic crossing of energy levels," *Proceedings of the Royal Society of London Series a-Containing Papers of a Mathematical and Physical Character*, vol. 137, no. 833, pp. 696–702, 1932.

[200] Zener, C., "Interaction between the d-shells in the transition metals," *Physical Review*, vol. 81, no. 3, pp. 440–444, 1951.

[201] Zener, C. and Heikes, R. R., "Exchange interactions," *Reviews of Modern Physics*, vol. 25, no. 1, pp. 191–198, 1953.

[202] Ziman, J. M., *Principles of the theory of solids*. Cambridge: University Press, 1972.

[203] Zitoun, D., Respaud, M., Fromen, M. C., Casanove, M. J., Lecante, P., Amiens, C., and Chaudret, B., "Magnetic enhancement in nanoscale corh particles," *Physical Review Letters*, vol. 89, no. 3, 2002. 037203.

VITA

Xiaoshan Xu was born on August 9th, 1975 in Nanjing China. He received a Bachelor degree and a Master degree of Science from physics department of Nanjing University in 1997 and 2000 respectively. He started his studies of physics at Georgia Tech in the fall of 2000. In August 2000, he joined the small system lab advised by Walter de Heer, where he has been working on cluster beam experiments for his Ph.D. thesis.